Label-Free Biosensors for Cytokine Detection

by

Bo-Ram Oh

A dissertation submitted in partial fulfillment
of the requirements for the degree of
Doctor of Philosophy
(Mechanical Engineering)
in the University of Michigan
2016

Doctoral Committee:

Professor Katsuo Kurabayashi, Chair
Associate Professor Jianping Fu
Assistant Professor Somin Eunice Lee
Assistant Professor Allen Po-Chih Liu

Acknowledgements

First of all, I would like to express my deepest gratitude to my advisor, Professor Katsuo Kurabayashi, for his supervision and mentorship throughout my Ph.D. program. I learned a lot from him while conducting research and benefited from his supervision and support during the Ph.D. program. His passion and keen eye for new research impressed me significantely and I have been greatly influenced by him to be a mature researcher. I was lucky to be in his lab and would not be able to achieve what I have done without his guidance. Furthermore, I would like to extend my thanks to my committee members who offered collegial guidance and support over the years: Professor Jianping Fu, Professor Allen Liu, and Professor Somin Lee.

I would like to thank the friends I met in Michigan and the lab members that I met in the Microsystems Technology and Science (MSTS) laboratory. I was fortunate to meet some good colleagues who inspired me, and had good discussions, and helped to explore my research. I would like to send my thanks to Dr. Nien-Tsu (Joe) Huang, Dr. Pengyu Chen, Dr. Robert Nidetz, Dr. Junghwan Seo, Dr. Sungjin Kim, Dr. Dibyadeep Paul, Mr. Meng-Ting Chung, Mr. Yujing Song, and Mr. Brian Berger.

Specially, I would like to express my deepest gratitude and love to my family. In particular, I would like to express my appreciation for my mother for her affection, love, prays of day and night, and endless support during my study. Although she was in Korea, whenever I needed her she was willing to spend her time, listen to my voice, and send

encouragement to support me. Always, she is one of my best friends and the best counselor to me.

I sincerely appreciate my father for his love, faith, encouragement, and support, which lead me to finish my Ph.D. program. He is still the wisest man I've ever met in my life and has inspired me in many ways. His concise but powerful advice and critical opinions were valuable assets of mine and lead me to achieve various things in my life, including my Ph.D. He is a great mentor and supporter and I always respect his intelligence and wisdom which influenced me a lot.

I would like to thank my grandmother for sending her love and support during my study. Her wisdom and encouragement enabled me to finish my study. Also, I would like to thank my parents-in-law for their warm encouragement and support of my study as well as their endless faith in me. I am really blessed to meet such wonderful parents-in-law. I thank my dearest brother Minsuk, for his encouragement, for chatting with me to share his thoughts whenever I had a hard time during my study, and for being a good friend of mine during my life.

Finally, I would like to express my gratitude and love to my beloved husband, Hongsuk Nam. I was so blessed to meet such a wonderful man at U of M and to get married during my Ph.D. He was thoughtful and supportive of my entire work and also was a good research collaborator. I am so proud that we could publish co-authored papers during our study at Michigan. Always, I deeply thank him for sharing my concerns and stresses, as well as his warm encouragement to finish my Ph.D. program.

Table of Contents

List of Figures

List of Tables

List of Appendices

Appendix

Abstract

Cytokines are protein biomarkers secreted by immune cells that serve as mediators in the immune system. The functional phenotypes of immune cells are important in recognizing immune functions and often determined by the dynamic cytokine secretion behaviors of immune cells. As a result, many researchers have attempted to quantify cytokines to develop a new approach to immune diagnosis and therapy. The lack of rapid, sensitive, multiplexed time-course cytokine monitoring techniques poses significant challenges to these research efforts. To fill this technological gap, this thesis has developed label-free biosensing platforms for rapid and sensitive cytokine detection.

In the first part of this thesis, an MoS_2-based field-effect transistor (FET) biosensor was developed to detect cytokines. This work advanced critical device physics by leveraging the excellent electronic/structural properties of TMDCs in biosensing applications as well as the research capability in analyzing biomolecular interactions with a fM-level sensitivity.

In the second part, we demonstrated a nanoparticle based localized surface plasmon resonance (LSPR) biosensing device integrated with microfluidic technology. The quantitative characterization of cytokine secretion behaviors from T-cells that are

altered by an immunosuppressive drug was studied at high temporal resolution. The biosensors achieved precise measurements with low operating sample volume (~1 μL), short assay time (~ 30 min), heightened sensitivity (~20-30 pg/mL), and negligible sensor crosstalk. Data obtained from the multi-cytokine secretion profiles provided a comprehensive picture of the time-varying cellular functional state during pharmacologic immunosuppression.

In the last part, integrated LSPR biosensor within a microfluidic system was developed for cell-based immune functional analysis. By placing cells near the sensing elements, we achieved in-situ measurement of the cytokine secretion behavior of immune cells. This platform has potential to facilitate real-time continuous measurement of the concentration of cell-secreted cytokines. The extended function of this platform may further allow us to measure cytokine secretion rate of cells to extract both the magnitude and time constant of the cellular response to an immunological environmental change.

Compared to previous labeling techniques for cytokine detection, the label-free FET and LSPR cytokine detection techniques are able to provide rapid, highly sensitive biosensing platforms, suitable for capturing the dynamic nature of immune response. Furthermore, the multiplexed detection capability integrated in a microfluidic system enables us to understand the cytokine-regulated functional characteristics of immune system. These platforms hold significant promise for point-of-care applications in clinical settings.

Chapter 1

Introduction

1.1 Introduction and Research Background

The immune system is a complex mechanism for the human host from pathogens, such as viruses and bacteria. The organs, tissues, cells and cell secreted protein biomarkers in the immune system work together to protect the body from external environments. Immune cells dynamically change their immuno-functional phenotypes, and such a change reflects the immune condition of the host. Some of the immunological functionality changes of immune cells are manifested by alterations of the cells' cytokine secretion behaviors.

Cytokines are small cell-secreted biomarkers, working as mediators and modulators in the immune system and work in the complex network to regulate the differentiation, growth, and inflammatory response of cells. Many researchers have been fascinated by the multifaceted roles of cytokines to tightly regulate and balance the immune system, and attempted to quantify cytokine molecules for screening infectious diseases or drug treatment and development (Figure 1.1). So far, many researchers

exploited the quantification of cytokine biomarkers to understand the immune condition of the patients for various immune related diseases. In some immune related diseases, the shifting between pro-inflammation and anti-inflammation statuses is often extremely dynamic and rapid while involving a complex cytokine communication network. In such cases, a rapid immunoassay that affords comprehensive characterization and quantitative analysis of multiple cytokine species secreted from immune cells is the key to precisely determine the variations and the dynamic characteristics of immune system.

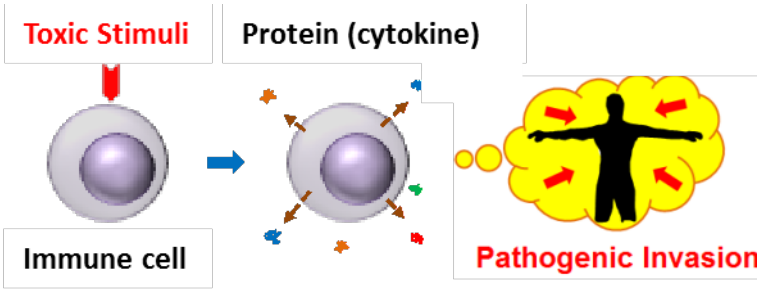

Figure 1.1: Concept of protein secretion response of immune cell to extracellular toxic stimulation.

Current gold standard methods for quantifying cytokines are enzyme-linked immunosorbent assay (ELISA) and bead-based immunoassay. In these techniques, target biomolecules are tagged with labels and the signal from the labels represent the quantity of target biomolecules in the sample. These labeling methods involve several sample preparation processes including multiple washing steps, and therefore they require long assay time between sampling to detection. Researchers were motivated to develop various cytokine biosensors, overcoming the bottlenecks of the conventional immunoassay techniques, to address clinical needs for disease diagnosis and immune system analysis by quantification of cytokines motivate. To capture the dynamic variation, the cytokine quantifying biosensors should be rapid, sensitive enough to detect subtle

variations in the cytokine secretion behavior, and able to provide information of a wide variety of cytokines for a comprehensive understanding of immune functional changes.

Label-free biosensing is a promising approach to measure immune cell-secreted cytokines while meeting the aforementioned requirements; they are less laborious assay by eliminating labels for the sensing, they quantify biomarker analytes in a physiological sample solution in a non-destructive manner, and thye offer a rapid and highly sensitive detection platform. Moreover, label-free biosensors have high potential for real-time monitoring of immune condition change which may provide a clear picture to understand time-varying cytokine-mediated immune responses. A previous study reviewed [1] various types of label-free cytokine biosensing platforms developed based on the signal producing mechanisms, including mechanical, electrical, optical, and plasmonic sensors. In the review, they pointed out the significance of the sensitivity (around 10 pg/mL) and speed (sample-to-answer time < 30 min) in cytokine detection biosensors for effective immune functional analysis (Figure 1. 2). Of note, not all label-free biosensors meet the requirements to reach such sensitivity and speed. Among those mentioned biosensors, electrochemical and localized surface plasmon resonance (LSPR) plasmonic detection schemes have the greatest promise for meeting the criteria to achieve high sensitivity and speed for cytokine assay. Thus in this thesis work, we focused on developing FET biosensors which is one of the electrochemical sensor and LSPR biosensor for analyzing cytokine assays, providing a rapid, highly sensitive platforms which has high potential to help researchers clearly understand immune function response.

An additional application of label-free biosensor for quantifying cytokine is a process called cytokine secretion assay. This process provides the means to quantify

cytokine molecules secreted by immune cells under endotoxin exposure and allows for characterizing immune cells' functional responses to infection, external stimulation, and drug modulation. Cytokine-mediated cellular functional responses are often extremely dynamic and rapid while involving various types of cytokines. Thus, the cytokine secretion assay is a good candidate to study with rapid, highly sensitive label-free biosensing techniques which we are dealing in this thesis work. However, general FET biosensors do not provide suitable platform for cytokine secretion assay, since they are susceptible to background noise when using complex physiological fluid sample. In cytokine secretion assay, various types of cell secreted cytokines are included in the fluidic sample and this hinders FET sensors to precisely detect target cytokines. Accordingly, only LSPR biosensing technique will be developed for cytokine secretion assay in this dissertation.

LSPR biosensors face challenges to comprehensively analyze complex, dynamic immune system by quantifying cytokines. In some cases, low sensitivity hinders capability to detect cytokines in the sample, or single cytokine measurement does not provide a full picture to understand the complex immune system involving multiplex cytokines. We suggest a potential solution to overcome such challenges by integrating a microfluidic system with LSPR biosensing techniques. By implementing a microfluidic system, we plan to offer platforms of sensor surface nanofabrication and provide sensitive nanoparticle based LSPR biosensors as well as provide reliable high-affinity multiple receptors for sensing. Besides, integrating biosensors in a microfluidic platform enables facilitating cell-based immune functional analysis by simultaneously measuring cytokine secretion behavior of immune cells in real-time, by placing cells near the

sensing elements. This real-time continuous measurement of concentration of cell secreted cytokines will allow quantification of the secretion rate, magnitude, and the time constant of cellular response to the immune condition change. By extracting cytokine secretion rate in the early stage of cytokine secretion and associate this secretion rate to analyze immune cellular response, we can eliminate the long incubation time to analyze the cellular response since we can estimate the end time of the incubation process.

To expand on this key idea, the following sections illustrate some additional background on cytokine, label-free biosensors, and especially the main topic of this research, FET, and LSPR-based label-free biosensing technique. More background of integrating microfluidic system for biosensing applications will be followed.

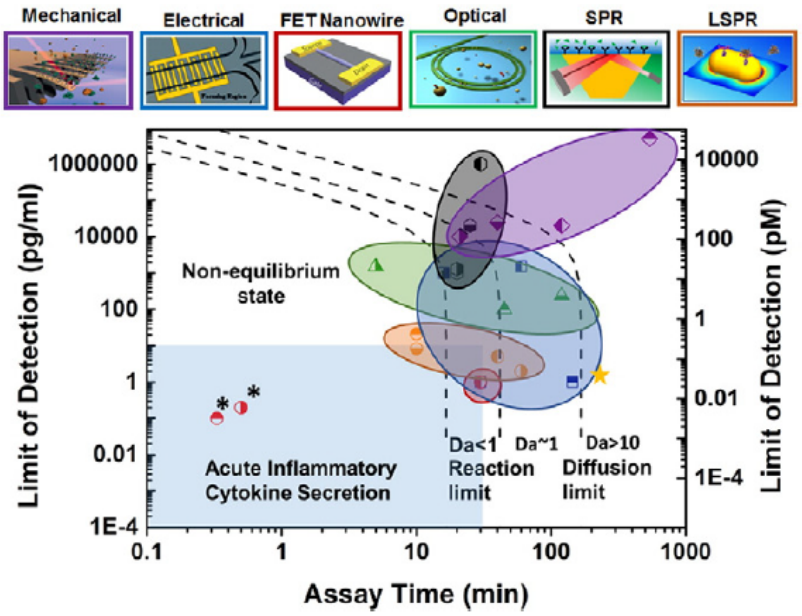

Figure 1.2: Regime map of label-free biosensors showing sensitivity vs. assay time. FET and LSPR biosensors have potential to provide us of sensitivity and assay time approaching to the desirable levels [1].

1.1.1 Cytokines

Cytokines are cell-secreted or membrane bound small bioactive proteins in the immune system. They are mediators and modulators playing key roles in various physiological processes, such as cell growth, cell differentiation, cell-to-cell communication, and regulating the host's inflammatory behavior [2] and response to immunomodulatory agents [3, 4]. The cytokine signaling processes in immune cells are initiated by the binding of specific cytokine molecules to the cell receptors, which subsequently cause the activation of intracellular kinases, DNA transcription factors, and gene expression [5]. These processes occur dynamically and reflect changes to the immune system condition change, which induces the dynamic nature of cytokine secretion in the immune system (Figure 1.3.a).

The multifaceted roles of cytokine working in the immune system to retain the balance of immunity prompted clinical interest to quantify these biomarkers for the application of screening infectious diseases or drug treatment and development [6]. Moreover, previous studies proposed that quantification of cytokine provides a more accurate way to diagnose bacterial infections than current diagnostic methods such as relying on symptoms, initial clinical markers, and laboratory markers [7, 8]. The quantification of cytokine biomarkers for understanding immune related diseases has been exploited for cancer [9-11], heart diseases [12], Alzheimer's [13], rheumatoid arthritis [14], and Crohn's disease [15].

Cytokines are pleiotropic, which means that they bind multiple targets and induce physiological phenomena, and this characteristic is referred as cytokine redundancy [16]. Also, cytokines are reciprocal, interacting with each other in a complex way (Figure 1.3.b)

[17]. As a result, understanding the network of cytokines in regulating the immune system provides clinically and immunologically useful information [18] related to inflammatory diseases, immune modulation, and also drug discovery. Owing to the complexity and tightly regulated nature of the cytokine network, previous studies pointed out the importance of scrutinizing multiple cytokines to understand physiological variation of immune system [19, 20]. Thus, in this thesis, cytokines are studied for understanding various immune-related cellular functional responses as well as screening immune system related diseases.

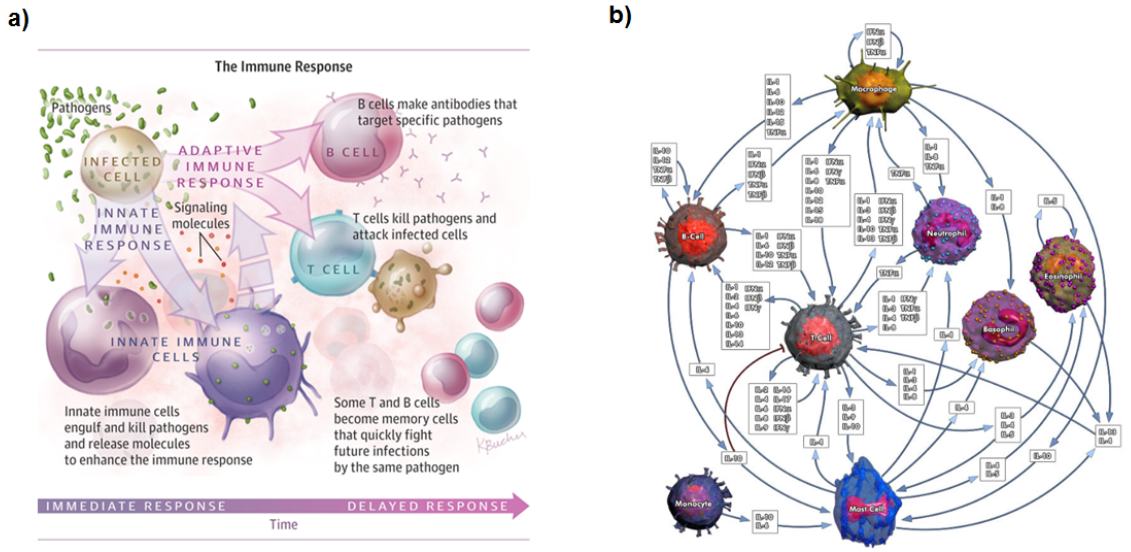

Figure 1. 3: a) Dynamic immune cellular response under pathogen attacks into immune system. *http://jama.jamanetwork.com/article.aspx?articleid=2279715*. b) A complex cytokine communicating network. *www.qiagen.com, www.SABiosciences.com*

1.1.2 Label-free Biosensors

In recent years, many researchers have been interested in label-free biosensing for its technical and practical advantages to overcome the shortcomings of other analysis techniques. The advantages of utilizing label-free biosensor are addressed in this section.

The elimination of labeling agents, such as fluorophores, isotopes, enzymes, and nanoparticles provides researchers more consistent results of quantifying cytokines by avoiding inconsistent labeling on target biomolecules, plus saving cost and time for assay. Label-free biosensor approaches are also suitable for binding kinetics of biomolecules since they do not require labeling process, while labeling approaches are not. Labels such as fluorophores or dyes are easily photobleached, and their signal decays over time. Thus, labeling approaches are not desirable for real-time signal acquisition or studying the binding kinetics. The label-free processes can determine the near end point of the incubation process (the time point when majority of target biomolecules settle down on the sensor surface) when we track real-time sensor response curve and find the time that the response curve reached plateau. With a sensor response curve over time obtained by a label-free technique, we do not need to wait for the long incubation to quantify target molecules. The initial slope of the response curve, i.e., the initial rate of binding, be correlated to the quantity of the analyte [21]. In this case, we are able to rapidly acquire analyte information by eliminate a long incubation process from the entire assay and rapidly acquire analyte information.

When it comes to cytokine-based immune monitoring, label-free detection techniques provide more significant advantage. Immune cells face alteration in their functional feature such as cytokine secretion in response to infection or external stimulation, and often cause the immune system to experience dynamic transition from pro-inflammatory phase to an anti-inflammatory phase or vice versa. A simple quantification of cytokines in the blood stream, lymphy nodes, or tissue alone may not be enough to monitor such rapid change of the immune status during the course of immune

response development. In this case, building a predictive model to understand immunity requires more comprehensive monitoring of complex and dynamic cytokine-mediated functional behavior of immune cells. Real-time measurement of cellular functional variation reflected by cytokine secretion provides a means to probe such behaviors. In some conventional techniques using labeling, provided qualitative information of cells by scanning variation of functional features of cells under immune condition change. However, precise determination of the cellular behavior requires the measurement of a quantitative parameter, such as the cytokine secretion rate. The rate provides critical information including magnitude and time constant of cellular time-varying response [22]. Only label-free quantification of cell-secreted cytokines will provide such information for researchers in a practical manner.

There exist various types of label-free biosensing platforms developed based on the signal producing mechanisms, including mechanical, electrical, optical, and plasmonic sensors. In this thesis, field-effect transistor based biosensor and localized surface plasmonic resonance based biosensor are mainly discussed because of their various superior features including high sensitivity and rapid assay time (Figure 1.3), which offer significant technological merits for characterizing time-varying cellular functional responses.

1.1.3 Field-effect Transistor Biosensors

Recent progress in nanomaterial synthesis and nanofabrication methods has enabled researchers to develop nanoscale biosensors. The recent field-effect transistor biosensors are highly dependent on nanofabrication methodologies, which recently grew drastically.

The principle of field-effect transistor (FET) biosensing methods is based on electrical signal change associated with target analyte binding on the sensor surface. The sensor surface is first prepared by immobilizing target analyte paired receptors. When target molecules are bound to the receptor, the channel (electrical channel connecting source and drain) surface potential changes and as a result the channel conductance varies. By measuring the conductance change from the transistor channel, the concentration of analyte in the solution can be quantified.

In general FET-based biosensing applications, a semiconductor material is connected to both source and drain electrodes. The third electrode, called gate electrode, which is capacitively coupled with a dielectric layer on the semiconductor channel, electrostatically modulates the current flow through the channel between sources and drain electrodes. For biomolecule sensing, the dielectric layer is functionalized with captured molecules, which is specific to the target molecule. When charged target molecules are conjugated on the captured molecules, the gate (electrostatic) effect occurs and gets transduced into readable signal such as change of FET drain-to-source current or channel conductance [23]. Semiconducting or conducting materials such as silicon nanowires (SNWs), carbon nanotubes (CNT), graphene, and layered two-dimensional materials have been fabricated into FET devices for biosensing applications. Early studies focused on using 1-D nanostructures such as SNWs and CNTs. However, the poor scalability and larger area manufacturability limit the use of these materials for FET biosensors. 2-D materials, such as graphene and Molybdenum disulfide (MoS_2), provide more advantages for biosensing [24-35]. With their large surface-to-volume ratio and electronic properties, 2-D FET biosensors are highly sensitive to biomolecular surface

binding [36-40]. Also, they exhibit low detection limits due to low electronic noise, which is attributed to the low density of scattering center. With high sensitivity, a FET biosensor is suitable for accurate cytokine secretion assay for cellular functional analysis. And without labeling processes, FET biosensors could offer platforms for rapid biomolecule quantification, real-time response recording, and molecule binding kinetic studies. In summary, 2-D material based FET biosensors are especially promising candidates for cellular functional analysis since they provide high sensitivity and short sample-to-answer time, and are suitable for miniaturization and integration in a system which has potential for multiplexed signal detection for cytokine secretion assay.

1.1.4 Localized surface plasmon resonance (LSPR) Biosensors

Over the last decade, plasmonic sensing techniques have been widely studied for biosensing applications. The principle of plasmonic sensing depends on the excitation of electromagnetic (EM) radiation on the noble metal (e.g. gold) surrounded by dielectric medium. When a several-hundred THz electromagnetic field (i.e. visible light) hits a noble metal surface, collective oscillations of free electrons near the metal surface called surface plasmons (SPs) are induced. When the oscillation resonates with a particular wavelength of incident electromagnetic field, the characteristic resonance mode of SPs arises. SPs generate an evanescent field between the metal and dielectric region and they exponentially decay into a dielectric region, which makes this resonance effect extremely sensitive to the local refractive index (RI) change near the metal surface. The RI change, induced from both surrounded medium change and biomolecule adsorption on the metal surface, induces the resonant condition of SPs. Tracing this change in real-time, SP based

biosensing techniques are suitable for label-free quantitative analysis of target biomolecules in the sample, antibody-antigen interactions, and protein binding kinetics[41].

The SP-based sensing techniques are developed in two setups: (1) surface plasmon resonance (SPR) and (2) localized surface plasmon resonance (LSPR). In SPR, propagating SPs are excited on a thin metallic film coupled with bulk optical elements, such as a prism (Figure 1.4.a). This optical setting is called the Kretschmann configuration. So far, the SPR setup has been the most conventional plasmonic biosensing technique. However, the Kretschmann configuration used in the SPR technique makes it hard to miniaturize and integrate the system with other functional systems, since it requires bulky optical elements. Furthermore, the SPR biosensors suffer from background noise coming from fluctuation of bulk refractive index. This is due to the long penetration length (a few hundreds of nm) of SPR evanescent field, which is much larger than the typical size of target molecule. As a result, the target molecule bound on the SPR sensor surface could be buried into detection noise level, which further leads to another limitation, such as lack of sensitivity. The detection limit of SPR detection is known to be around pM-nM range. Thus the poor detection limit of SPR technique hinders use for clinical sample detection, which generally requires fM-pM level detection limit for small target analytes (e.g. cytokines).

Recent advances in nanomaterials and nanofabrication guide the development of LSPR-based biosensing technologies. LSPR biosensors are promising candidates for rapid, real-time, label-free detection for biomolecule detection. In LSPR, metal nanoparticles/nanostructures in sub-wavelength size are excited by an external light

source to generate surface plasmons (Figure 1.4.b). The highly localized EM field in LSPR generates confined evanescence fields near the metal sensing surface. This feature enables LSPR sensors to be more sensitive to the surface binding of target molecules. For conventional LSPR biosensing, the nanoparticles are functionalized and coated with capture molecules and the target analytes are captured on the sensing nanoparticles via the capture molecules. Thus, target analytes bound to the nanoparticle surface occupy a large volume fraction of the evanescent field of LSPR and yield high sensitivity, which permits the detection a low concentration of small molecules. Furthermore, unlike SPR sensors, the evanescent field of LSPR can be directly excited by light illumination with free space optics, which eliminates bulky optical components. Owing to the confinement of the sensing region near the nanoparticle and ease of signal acquisition, LSPR biosensing has potential for miniaturization, integration, and multiplexing while maintaining high sensitivity.

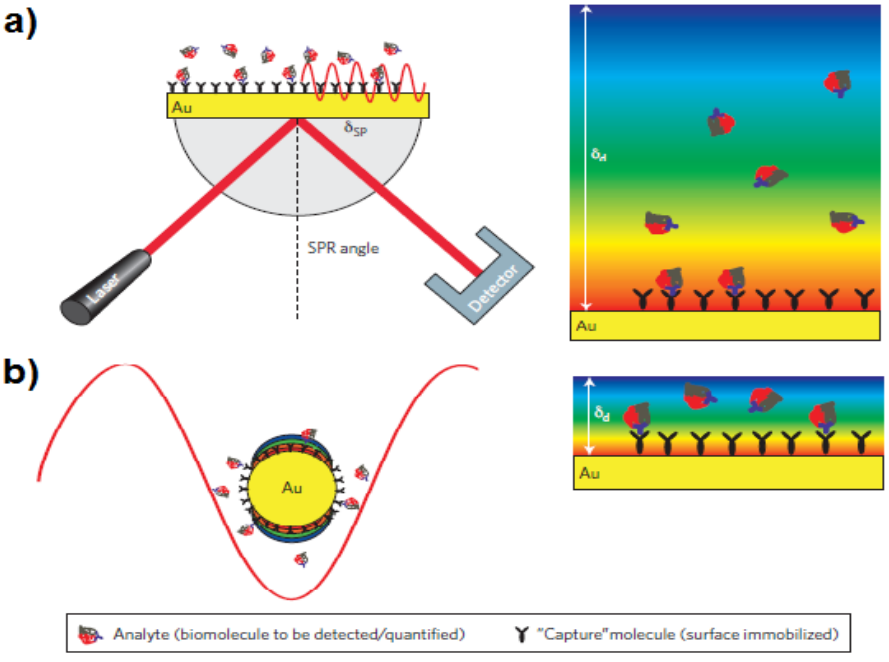

Figure 1.4: Schematic representation of a) Kretschmann configuration of SPR generated on the metal film and b) LSPR occurred around single nanoparticle. This figure also illustrates the decay length (δ_d) of SPR and LSPR. The color gradient in the figure presents the field intensity distribution (enhanced field at the surface (red) and decreases field (blue) towards dielectric medium) [42].

1.1.5 Microfluidic System

Many researchers have demonstrated integrated microfluidic systems offering several advantages for biosensing applications. Microfluidic systems can enhance the reaction speed of reagents with a confined volume and provide conditions suitable for detecting low concentrations of small molecules [43]. The confined environment can easily generate strong convection flow with a small flow rate. This convection will enhance analyte transport to the sensing area and increase the chance for the analyte molecules to meet with target receptors on the sensor. Furthermore, the short sample-to-sensor distance in the microfluidic environment reduces the binding assay time. Since the target detection molecules are placed near the sensing surface, the diffusion time of target molecule to the sensing surface is reduced. Microfluidic platforms are able to couple with several other practical functions such as sample and reagent loading, analyte signal detection, multiplex analyte detection. Moreover, by integrating multi-functional microfluidic system for biosensing, we can design high throughput platform for analyte signal sensing.

1.2 Motivation for Research

The first motivation of this research is to provide label-free biosensing platforms for rapid, sensitive cytokine quantification biosensors and more effectively evaluate dynamic response of immune system. The central challenge of traditional techniques for

rapid sensing is mainly coming from using labels for quantifying cytokine biomarkers. As briefly mentioned before, labeling techniques require several sample preparation processes, multiple washing steps, and a long assay time which is laborious, expensive, and time consuming. These features hinder rapid sensing for cytokine quantification. To probe dynamics and subtle variation of the immune system, the platform should provide rapidness and enough sensitivity to capture the change of cytokine concentration in the sample. Furthermore, to characterize the time-varying immune response upon immunity change, real-time sensing technique has potential to provide a clear picture about the dynamics of immune condition variation.

The second motivation for this research is to demonstrate microfluidic system integration to eliminate the challenges of current label-free LSPR biosensing techniques for cytokine secretion assay. Some of label-free LSPR biosensors face limitations such as lack of multiplexed detection capability, limited measurement throughput. To comprehensively study cytokine secretion assay, the challenges should be solved. A microfluidic system is a potential solution which enables multiplex target measurement and high throughput measurement. Furthermore, the microfluidic system has potential to provide such a platform to study cell secretion monitoring in real-time by implementing cells in the device which enables us to study cellular functional change and enable us to extract additional factors such as secretion rate and time constant for analyzing immune system.

These motivations lead us to develop label-free biosensors integrated in a microfluidic system. To accomplish this goal, we developed two-dimensional

nanomaterial-based FET biosensors and nanoparticle-based LSPR biosensors and further incorporated the biosensors with our own designed microfluidic device.

1.3 Thesis Objectives

This thesis research has three main goals that are driven by the motivations above and that address the shortcomings of current technology. The first goal is to develop a label-free field-effect transistor biosensor to detect cytokines in a physiological medium. In general, FET biosensors have great potential to offer a rapid, high sensitive platform, which can meet the primary need to characterize the dynamic response of immune system from cytokine levels in blood or serum. Atomically layered transition metal dichalcogenides (TMDCs) are prepared for constructing transistor biosensors integrated in a microfluidic sample loading channel for cytokine detection. Due to the high sensitivity of the atomically layered TMDCs materials to the surface binding of target molecules, we expected this platform to be suitable for biomolecule sensing application. Furthermore, by recording the real-time analyte binding kinetics using the sensor, we are able to determine a signal readout duration time which can differentiate samples according to the concentrations of cytokines in the sample. However, general FET biosensors do not provide a suitable platform for cell-secrete cytokine detection, since they are susceptible to background noise when using complex physiological fluid sample. In detection of cytokines secreted from cells, various types of cell-secreted cytokines are included in the fluidic sample and this hinders FET sensors to precisely detect target cytokines. Accordingly, only LSPR biosensing technique will be developed for cell-secreted cytokine detection in this dissertation. The second goal of this thesis is to

develop a multiplexed time-course measurement of cell-secreted cytokines using LSPR plasmonic biosensors. Using a microfluidic nanoparticle patterning method, we fabricate a high-sensitivity LSPR cytokine biosensor device. With the device, real-time monitoring of cytokine binding curve is performed to calculate how fast we can get cytokine quantification data out of the developed platform. The time-course profiles of four different cytokines obtained by the platform will give us abundant information to analyze cellular functional response in a rapid, sensitive, and multiplexed manner. The last goal is to show the multi-functionalities of the integrated microfluidic platform for human blood analysis together with label-free LSPR-biosensors. Our microfluidic device allows cell separation, incubation and cytokine detection in a single platform. This platform is aimed to synergistically take both advantages from label-free LSPR biosensing and microfluidic environment.

1.4 Thesis Outline

Based on the research objectives in the above section, the thesis comprises five subsequent chapters. The outline is as follows:

Chapter II - Review of Related Studies: This chapter reviews other previous research related to this thesis work. First, generally existing label-free biosensing techniques will be briefly discussed and then more specific label-free detection techniques of our focus will be reviewed. The review is divided into two topics: (1) label-free biosensors – especially (i) field-effect transistor based biosensors and (ii) plasmonic biosensors – and (2) integrated microfluidic systems with biosensors. Here, the

advantages and limitations of current label-free biosensors will be critically reviewed, and the potential of integrated microfluidic biosensor systems will be described.

Chapter III - Label-free FET-based Cytokine Detection Device: In this chapter, an MoS_2-based transistor biosensor capable of detecting cytokine is demonstrated. First, the nanofabrication processes of atomically layered TMDCs for biosensing platform will be discussed. The sensor performance for cytokine quantification is validated using different concentrations of purified cytokine samples, and the binding kinetic measurement will be extracted by the association/dissociation rate of antibody-antigen. The impact of this work, leveraging the electronic/structural properties of TMDCs for biosensors, and ability in analyzing biomolecule interaction with ultra-sensitivity, will be discussed.

Chapter IV - Label-free LSPR-based Multiplex Time-course Cytokine Detection: In this chapter, T-cell behavior under immunomodulation and their cytokine secretion will be discussed. Then T-cell stimulation, drug administration, and sample collecting process will be explained. A new fabrication method using charged gold nanorods for manufacturing LSPR microarray device will be discussed. Then four different cytokine time-course profiles secreted from T-cells will be analyzed to study the subtle variation of cellular function under immunomodulation. After new cytokine secretion patterns are revealed from the developed fine time-course cytokine profile detection platform, we will discuss future potential applications of the platform.

Chapter V - Integrated Microfluidics LSPR-based Cell secreted Cytokine Detection: In this chapter, designing and fabricating the multi-functional PDMS device will be demonstrated. To utilize human blood sample for the measurement, the preparation and bead-conjugation processes before loading into PDMS device will be

explained. The integrated device structure will be explained and LSPR biosensing physics will be introduced. Then the device performance will be validated by using purified cytokine samples. Furthermore, real-time anlyte binding curve will be studied and cytokine quantification using real human blood cells will be demonstrated. In here, the synergistic collaboration of a microfluidic system and a LSPR detection platform will be illustrated by the result.

Chapter VI - Conclusions and Future Works: The final chapter summarizes the impact of the present research and discusses potential research directions. The future work of FET-based biosensor includes multiplexed measurement of cytokines from the samples which requires patterning the array of sensing materials, or developing an integrated microfluidic system for real-time cell secreted cytokine measurement. For LSPR-based biosensor, the future work includes designing a microfluidic platform directly capturing cells in close proximity to integrated nanoparticle-based LSPR biosensors and measuring the dynamic cellular cytokine secretion profiles in real time.

Chapter 2

Literature Review

This chapter provides a review of previous studies related to this thesis work. The review gives insight into the motivations and applications of our research as well as analysis of competing technologies. This thesis work aims to develop cytokine biosensor technologies taking advantage of label-free technologies and integrated microfluidic systems. The review is composed of two main sections related to this goal: (1) label-free biosensors including (i) field-effect transistor biosensors, (ii) plasmonic biosensors, and (2) integrated microfluidic systems for biosensors. Each section details why this review is relevant and discusses multiple previous work that studied the topic. The review will summarize the achievements and limitations of existing work and describe how to address these problems in this thesis work.

2.1 Label-free Biosensors

The conventional label-free biosensing techniques follow three processes for biomolecule sensing: (1) preparing a sensing element on a surface, (2) binding target

biomolecules on the sensing element, and (3) collecting the signal information via a sensing signal transducing mechanism. Based on the signal transducing methods, we can categorize label-free biosensors as mechanical, electrochemical, optical, or plasmonic biosensors. As mentioned in the previous chapter, in this thesis work, FET-based biosensor and plasmonic biosensors are chosen, and thus we are focusing on reviewing these sensors.

2.1.1 Field-effect Transistor Biosensors

Recently, many studies have focused on developing a field-effect transistor for biosensing applications. After developing nanomaterials and nanofabrication techniques, semiconducting/conducting materials have been widely used for various biosensors such as for pH sensors, glucose sensors, cancer biomarker detecting sensors, and sensors for cytokine biomarker detection. The general working mechanism of field-effect transistor (FET) biosensing methods is based on electrical signal change associated with slightly charged target analyte binding on the sensor surface. First the sensor surface is prepared by immobilizing target analyte paired receptors. When target molecules are bound to the receptor, the channel (electrical channel connecting source and drain) surface potential changes and as a result the channel conductance varies. By measuring the conductance change from the transistor channel, the concentration of analyte in the solution can be quantified.

Created from nanowires (NWs) and carbon nanotubes (CNTs), FET biosensors provided sensitive platforms for biomarker detection; they are widely utilized for diagnosing biomarkers from nM to fM range in serum [44-49] nM proteins in cell growth system [50, 51], and affinities/kinetics of protein interactions with fM-level sensitivity

[52]. The fM level limit-of-detection (LOD) attained by nanoscale FET biosensors is due primary to the dimension (nanoscale) and good electrical properties which enable highly sensitive label-free biosensors for biomolecule quantification. Furthermore, their suitability for biofunctionalization provides good selectivity and biomolecule detection [53]. Such biosensors with consistent transistor responses would provide reliable lab-on-a-chip platforms for various biomolecule monitoring studies including quantification of target analyte and characterization of analyte-receptor binding kinetics. Pui et al [54] established very fast (20s) and ultrasensitive (LOD around 0.1 pg/mL) cytokine detecting biosensors using silicon nanowires. In their study, the biosensor simultaneously monitored the time-course dynamic secretion of TNF-α and IL-8 in complex biological fluids (cell culture medium of macrophage cell, or blood sample of rats) under LPS stimulation. The dynamic secretion of two cytokine was characterized in a cell culture medium and in 1000 times diluted animal serum using the platform (Figure 2.1). The cytokine levels kept increasing in cell culture medium whereas the cytokine secretion in animal serum initially increased and decreased after reaching a peak (Figure 2.1.c). These different secretion profiles collected by the developed platform clearly show the complex nature of the immune response of living organisms. However, the drawback of this study is using a common top-down approach to fabricate the sensor element, which requires expensive manufacturing processes. FET-biosensors have great potential to be used as point-of-care devices. However, the high cost is a significant drawback for the disposable use of these devices in point-of-care biological assay.

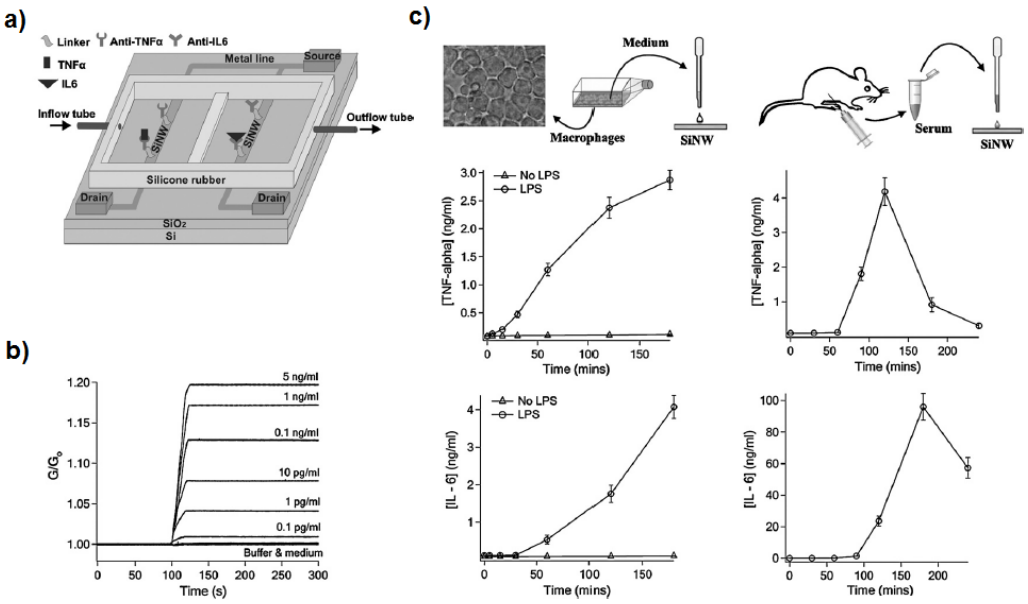

Figure 2.1: a) Schematic illustration of SiNW platform which can simultaneously detect TNF-α and IL-6 cytokine. b) Time vs. nanowire conductance variation curve by introducing various protein concentration ranging from 0.1 pg/mL to 5 ng/mL. c) Time-course cytokine secretion detection from macrophage culture medium and blood serum from rats [54].

Likewise in a previous study introduced above [54] , serious fabrication constraints exist for 1D nanostructure based FET biosensors [44, 48, 54]. Generally, to achieve highly sensitive FET biosensors to monitoring biomarkers, small-size NWs and CNTs are needed. To achieve an ultralow detection limit, the critical dimensions of the sensing channel should be comparable to those of charged molecules to maximize the gating effect [47, 55, 56]. Usually CNTs and NWs are produced by bottom-up synthesis methods such as chemical vapor deposition (CVD). Currently, the lack of a proper top-down fabrication method to produce an ordered array of nanostructures hinders the construction of high throughput biosensing platforms using NWs. Top-down techniques are able to fabricate high-quality SiNWs [52]. However, the fabrication of such a high quality Si NW array requires an expensive semiconductor-on-insulator (SOI) substrate and exquisite nanolithography tools resulting in high processing costs.

Two-dimensional (2D) atomically layered materials such as graphene, topological insulators (TIs), and TMDCs, are potential materials for FET biosensors due to their attractive electronic/optoelectronic properties, large abundance, and compatibility with planar nanofabrication processes [24-35]. Owing to their atomically thin layered structure, the electrical properties in 2D materials are highly sensitive to the external stimuli. Such feature enables the 2D FET biosensors to be more suitable for ultrasensitive biosensing applications [36-40]. Huang et al. have demonstrated graphene oxide-based FET sensors capable of detecting IL-6 cytokine biomarker [57]. In this study, atmospheric-pressure ethanol Chemical Vapor Deposition treated graphene oxide (ECVDGO) was utilized for biosensing substrate while overcoming the limitation of general graphene-based biosensors (Figure 2.2). With the treated GO, they decreased the electrical resistivity from 1.99×10^6 Ω/square to 4.68×10^3 Ω/square, and resistivity variation from 1.60×10^6 to 7.72×10^2 Ω/square. They also demonstrated the sensor performance using Interleukin-6 cytokine with a detection range from 4.7 to 300 pg/mL. This study pointed out the potential of GO with high manufacturability for FET biosensors of sensitive and label-free detection of biomolecules.

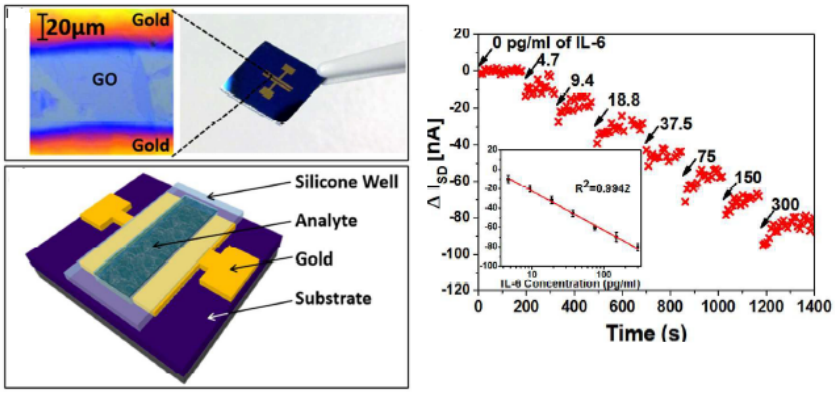

Figure 2.2: Graphene Oxide used as filed-effect transistor biosensor for sensitive and label-free detection of IL-6 cytokine biomarker [57].

Graphene-based FET biosensors have good potential as well. However, zero-bandgap graphene has some drawbacks such as a low ON/OFF current ratio and increased leakage current which leads to reduced sensitivity. In contrast to graphene, semiconducting TMDCs (e.g. MoS_2) have sizable bandgaps and exhibit high ON/OFF current ratios up to 10^8. When this feature is combined with their atomically layered structures, they can provide sensing platforms with much higher sensitivity than graphene [23, 58, 59]. Recently, Wang et al. and Sakar et al. demonstrated how few-layer-MoS_2 flakes can be utilized for FET biosensors [23, 60]. Wang et al. established 400fM level LOD MoS_2 FET biosensors for detecting a cancer-related biomarker called prostate specific antigen (PSA) and showed the real-time detection of the biomarker (Figure 2.3) [60]. Sakar et al. also provided FET biosensing platforms to detect biomolecules (biotin-streptavidin) as well as pH sensing platforms that utilize few-layered MoS_2 (Figure 2.4) [23]. The developed biosensors offer 100 fM level LOD for the streptavidin detection and pH detection capability that is 74 times as sensitive as graphene based FET biosensors (Figure 2.4.c). They emphasized the potential of MoS_2 based FET biosensors for future point-of-care devices since they are label-free, highly sensitive, and scalable sensors with low production costs and low power assumptions. Their study clearly summarized the advantages of utilizing MoS_2 for FET biosensors in comparison to other 1-D and 3-D materials as well as graphene. Using MoS_2 for the FET-based biosensor provides various advantageous features such as high sensitive, low-cost mass production, planar patterning capability, and device scalability (Table 2.1). Thus, in this thesis work, MoS_2 FET biosensors for the rapid, highly sensitive cytokine biomarker detection will be explored.

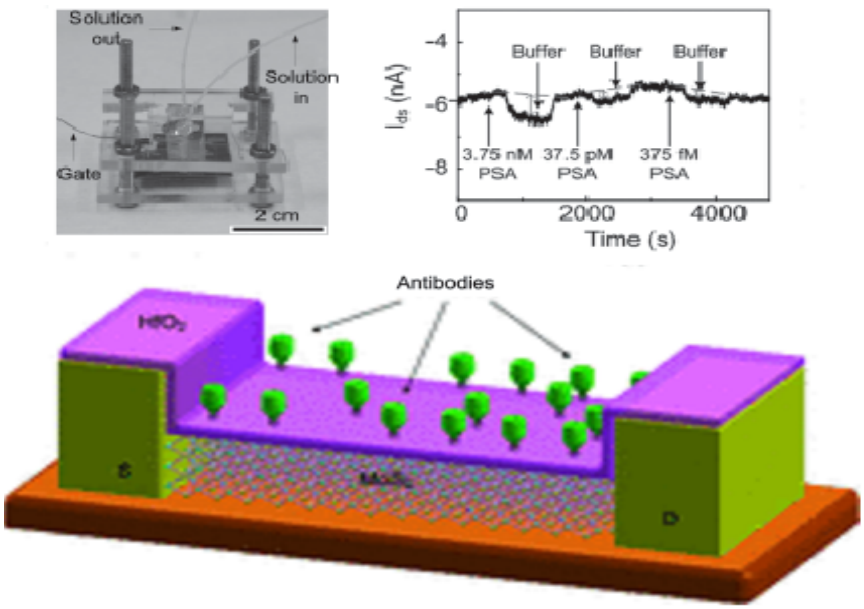

Figure 2.3: Label-free MoS_2 nanosheet-based field-effect biosensor for cancer marker protein detection in real time with high sensitivity and selectivity [60].

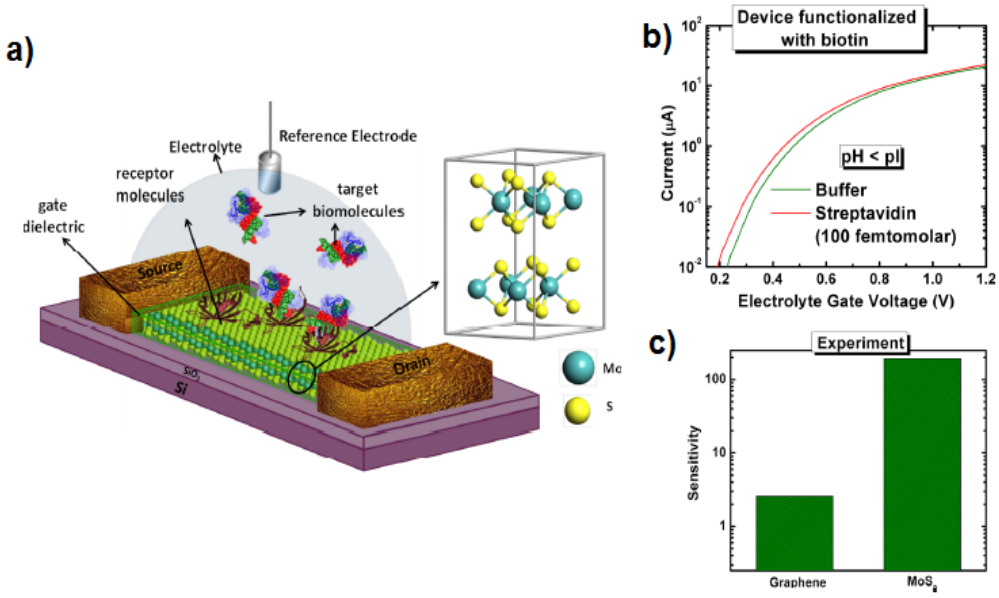

Figure 2.4: a) Schematic of MoS_2-based FET biosensor. The dielectric layer covering MoS_2 channel is functionalized with receptor molecules. When a charged target biomolecule is captured on the receptor molecule, it will induce gating effect and change the device current. b) The high sensitive MoS_2 biosensor device significantly increase in current when 100 fM streptavidin solution at pH 3 was added on to the sensor with biotin coated. c) Comparison of sensitivity of graphene and MoS_2–based FET biosensor of pH sensing. MoS_2 -based FET biosensor is 74 times higher compare to graphene biosensor [23].

TABLE 1. Comparison of MoS_2 with Other Competing Materials for FET-Based Biosensing[a]

		sensitivity	device fabrication and large-scale integrability	device scalability	flexibility and transparency
3D bulk materials		*low (inferior electrostatic gating effect through biomolecule conjugation)*	possible	*low*	*low*
1D nanomaterials	Si NW	high (excellent electrostatic gating effect through biomolecule conjugation)	*(i) top-down method: high cost and slow production rate; (ii) bottom-up method: severe integrability issues*	possible but process-wise challenging	*low*
	CNT	high (excellent electrostatic gating effect through biomolecule conjugation)	*(i) separation of metallic and semiconducting nanotubes required; (ii) severe integrability issues*	possible but process-wise challenging	high
2D nanomaterials	graphene	*low (excellent electrostatic gating effect but low carrier modulation)*	(i) low-cost mass production possible; (ii) planar platform provides easy patternability and integrability	high	high
	MoS_2	high (excellent electrostatic gating effect through biomolecule conjugation)	(i) low-cost mass production possible; (ii) planar platform provides easy patternability and integrability	high	high

Table 2.1: Comparison of MoS_2 material with other competing materials for FET-based biosensing. The characteristic such as sensitivity; device fabrication and large-scale integrability; device scalability; and flexibility and transparency were compared [23].

2.1.2 Plasmonic Biosensors

Over the last decade, plasmonic biosensors were extensively studied for various applications. As mentioned in the previous chapter, the principle of the plasmonic biosensors depends on the interaction of electromagnetic (EM) radiation on a noble metal in contact with surrounding dielectric medium. Coherent oscillations of free electrons near the metal surface called surface plasmons (SPs) resonate with incident excitation light frequency. SPs own the evanescence field at the boundary area between the metal and dielectric region and this field exponentially decays into a dielectric region. The resonance mode of SPs is sensitive to the local refractive index change and this change is induced by the adsorption of biomolecules in the metal-dielectric interface results in the alteration of the resonant condition of SPs. SP-based biosensing is found in two settings:

(1) the surface plasmon resonance (SPR) setting, where SPs occur at the interface between a thin metal substrate and a dielectric medium; and (2) the localized surface plasmon resonance (LSPR) setting, where SPs are excited at the surface of subwavelength sized nanoparticle/nanostructure by an external light source (Figure 1.4).

The most widely used plasmonic biosensing technique for biological and chemical analyte detection is label-free SPR biosensing. Especially for the biomolecule sensing (e.g. biomolecule quantification), SPR biosensors can overcome the shortcomings of labeling-based conventional techniques, such as long sample preparation time, complex processes, and large sample volume requirements, by eliminating tedious labeling processes. However, SPR detection suffers from several fundamental limitations while working as a biomolecule detection sensor due to its Kretschmann arrangement involving a bulky prism, and yielding a longer surface plasmon decay length (δ_d) than the LSPR technique. This SPR arrangement hinders sensor miniaturization and integration with other functional systems, such as point-of-care devices. Moreover, the longer surface plasmon decay length (δ_d) in SPR (Figure 1.4.a) is typically on the order of half of the resonance wavelength (few hundreds of nm). This feature enables SPR biosensors to provide higher sensitivity to a bulk refractive index (RI) change, and is susceptible to background noise coming from bulk refractive index fluctuation. The sensitivity of SPR biosensors usually lies between 10^{-7} and 10^{-6} in refractive index unit (RIU)[61, 62] which represents the range of pM-nM detection limit for the target analyte detection. However, in clinical studies the small molecule such as cytokine molecule concentration falls around range of pM-fM [63]. Thus, to overcome the sensitivity limitation, some of SPR

sensing platforms involved using secondary antibodies or compounds to amplify the sensing signal.

Chou et al. demonstrated an SPR biosensor combined with a secondary antibody as a signal enhancer for detecting IL-6 in cell culture medium and achieved a detection limit around 1.3 ng/mL [64]. Several studies further use nanoparticles to enhance the SPR signal. Martinez-Perdigueroa et al. and Law et al. developed a nanoparticle-based SPR biosensor by integrating gold nanoparticles and immunoassay technologies into SPR system to detect cytokines (Figure 2.5) [65, 66]. In both studies, an evanescent field that was extended from the gold film to the gold nanoparticles induced plasmonic coupling, drastically enhancing the detection sensitivity. Approaches mentioned above introduce a secondary element to enhance the SPR signal and provide better detection limit for the sensing. However, all these methods implemented additional assay steps, complicate overall procedures, and diminish the merits of label-free sensing by tagging labels to the target molecule.

Battaglia et al. explored alternative SPR excitation methods using fiber-optics to improve the sensing performance for SPR detection [67]. In the study, IL-1, IL-6 and TNF-α in PBS solution was detected with fiber-optics and achieved sensitivity around 1 ng/mL, but failed to meet the sensitivity level of clinical requirements such as few pg/mL. Furthermore, improvements of the sensing capability of SPR biosensors were explored by improving the characteristics of the metal thin film layer (Figure 2.5.c) or by altering the dielectric surrounding [68].

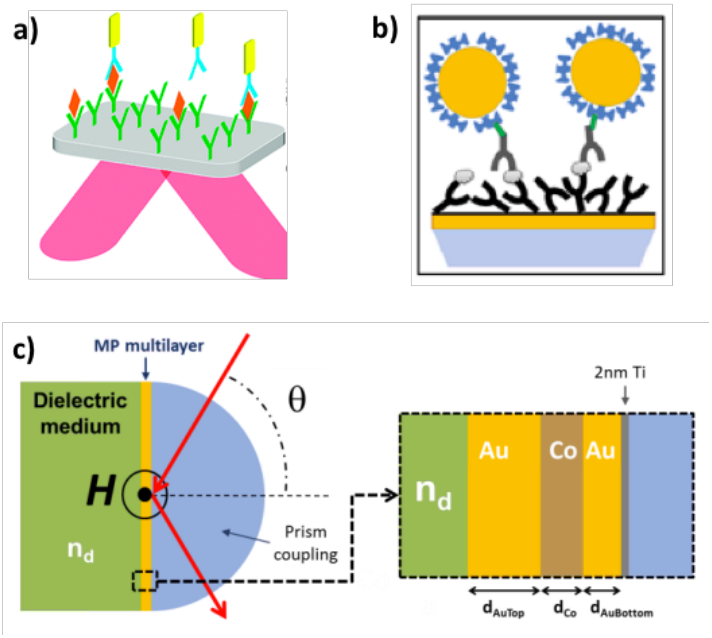

Figure 2.5: a,b) SPR sensing introducing gold nanoparticles to enhance the SPR signal to increase sensitivity [65, 66]. c) Modified characteristics of metal thin film layer to improve SPR sensing capability [68].

Recent advances in nanomaterials and nanofabrication processes open up the potential of LSPR plasmonic biosensing techniques for fast, real-time, label-free detection of biological species. The evanescence field surrounding LSPR sensors is directly excited by EM illumination by free space optics. As a result, in LSPR, the bulky optics is not required and the system can be miniaturized and integrated with other systems. Furthermore, the EM field is highly confined to a local area near a metal nanostructure surface; biomolecules attached onto the nanostructure surface occupy a large fraction of the evanescence field volume. This leads to a significant change of the LSPR signal from the sensing substrate and result into high sensitivity that allows capability to detect small molecules.

Huang et al. demonstrated LSPR biosensors detecting TNF-α molecules using a silver nanoparticle [69]. This biosensing technique offered an ultrasensitive platform

which enables measuring single molecule level detection. But this sensing mechanism requires long analysis time for analyte binding to reach equilibrium, which hinders use of rapid immune diagnosis application. For more rapid sensing of cytokine molecules, Chiang et al. and Huang et al. measured IL-1β and TNF-α by providing few tens of pg/mL detection sensitivity within less than 10 min [70, 71]. However, in these platforms the fiber probe should be dipped into a large volume of sample for signal measurement, which leads to practical limitations in its clinical applications.

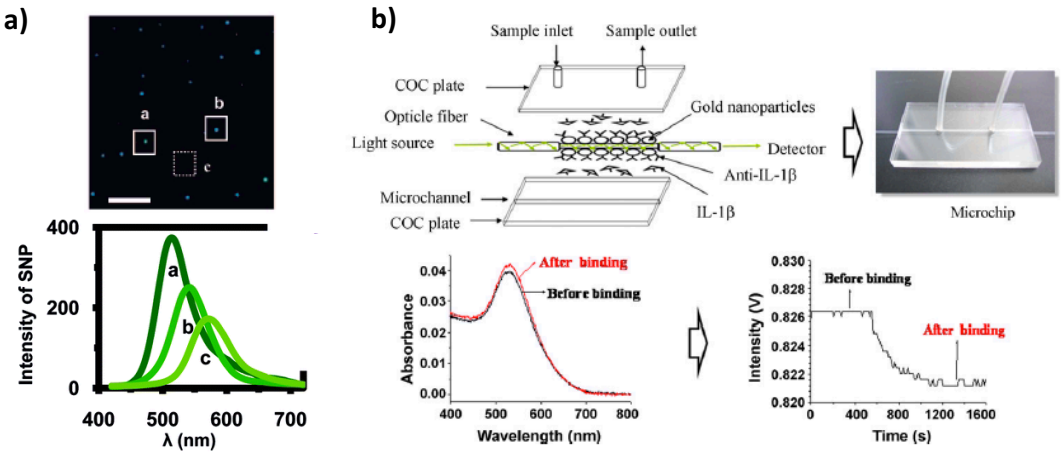

Figure 2.6: a) A single silver nanoparticle-based nanoplasmonic biosensor for immunoassay detection [69]. b) Fiber-optics based rapid, sensitive LSPR biosensing platform [70].

Recently, Chen et al. developed a nanoparticle patterned microarray type of LSPR biosensing device detecting multiple cytokine species using few serum cytokine samples in a single device at the same time [63]. In this study, instead of using a single nanoparticle, the patterned array of nanoparticles was used as sensing element and functionalized with six different probe antibodies for sensing. This platform allows high throughput analysis of cytokine biomarker in 1 μL serum sample to a detection limit around 10 pg/mL within 40 min. To summarize, the LSPR biosensing technique has high potential for small molecule detection owing to the small size scale and simple setup for

signal acquisition, which will be desirable for sensor miniaturization, integration, and multiplexed detection.

2.2 Integrated Microfluidic System for Biosensors

Modern advances in microfabrication technologies have enabled a number of studies to integrate biosensors in a microfluidic platform with on-chip fluidic channels, chambers, and valves. The microfluidic integration of biosensors fully incorporates the advantages coming from both biosensing techniques and microfluidic systems, then offers advanced platforms performing various functions. Here, some of label-free biosensors integrated in a microfluidic system will be reviewed.

Stern et al. developed label-free FET biosensors integrated in a microfluidic system to mitigate the limitation of FET biosensors using complex physiological fluidic samples for sensing [72]. By eliminating the use of labels in assays, some of label-free biosensing methods, including FET biosensing platforms, faced obstacles such as being susceptible to false positive signals induced from non-specific bindings of untargeted molecules. In this study, authors designed silicon nanoribbon structured FET biosensors integrated in a microfluidic chip to eliminate interferences of other background molecules with cancer biomarkers in whole blood. In the platform (Figure 2.7.a), the researchers incorporated a mechanism that first captured biomarkers from blood samples and subsequently released captured molecules by photocleaving crosslinkers after washing the sample. The released biomarkers were transferred into an area with sensors in the microfluidic system, and purified biomarkers were detected using the FET biosensors. A similar microfluidic analyte purification approach could be employed for label-free cytokine FET-based biosensors to attain desirable selectivity and sensitivity.

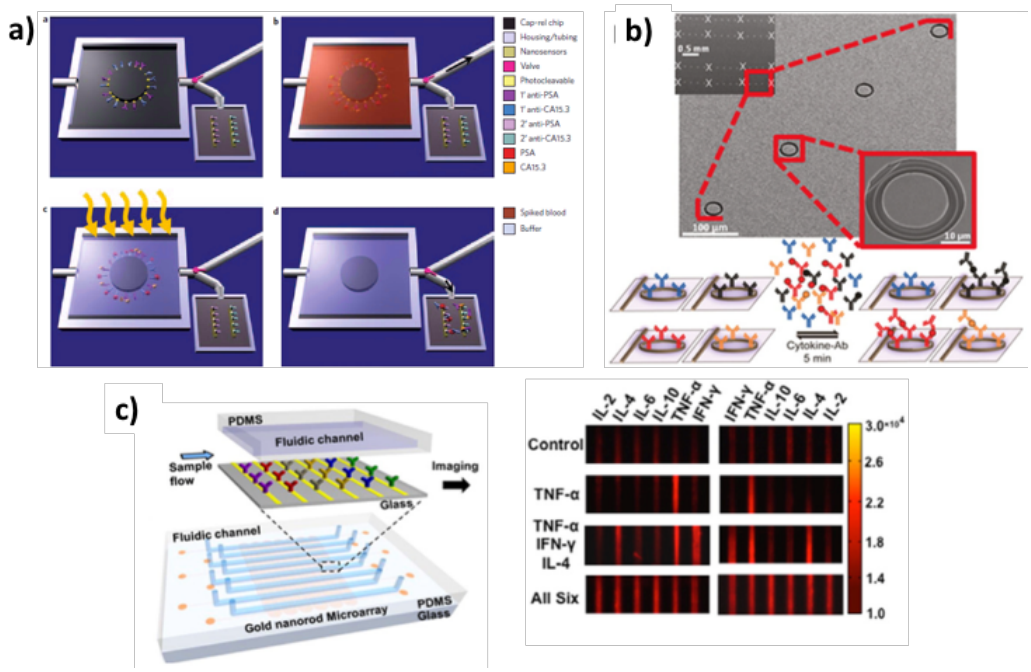

Figure 2.7: Integration of label-free biosensors with microfluidic system which enables on-chip sample preparation and multiplexed cytokine detection. a) Processes of selectively purified target proteins from whole blood sample using microfluidic device. The captured target biomolecule is separated from sample and photocleaved from crosslinker and transferred into sensing area [72]. b) Multiplexed cytokine detection using silicon micro-ring resonator arrays integrated in the microfluidic system [21]. c) Multiplexed cytokine detection using LSPR biosensor-array integrated in the microfluidic system [63].

Labe-free biosensors integrated with microfluidic platforms could provide another important advantage: multiplexing power in cytokine measurement. Recent studies [21, 63] developed integrated label-free biosensors in a microfluidic system by designing biosensor arrays in the device, and enabled researchers to perform simultaneous detection of multiple different cytokines from the sample (Figure 2.7.b, c). In these cases, the whole system incorporates microfluidic channel arrays with integrated optical biosensor arrays and enables high throughput, duplicated, and multiplexed measurement of cytokines in the sample solution. The ability to detect the analytes in parallel provides the means to simultaneously monitor the time-course variation of the amount of different

cytokine species in human samples to study the complex dynamics of the immune system of the host. Furthermore, the high throughput, duplicated measurement from a single sample will offer large sets of data and enable us to obtain a high level of statistical data while reducing false-positive readout signals.

The integrated microfluidic system with label-free biosensing could be utilized for cytokine secretion assay. Cytokine secretion assay provides an approach to study the immune response during the immunity change such as the anti-inflammatory phase arising after systemic inflammation. Instead of quantifying cytokine levels in the blood stream, lymph nodes, or collected samples, this assay directly characterizes immunity-related cellular functional phenotypes. The cytokine secretion assay involves immune cell isolation, stimulation, and cell culturing, followed by cell-secreted cytokine detection. The quantification of cytokines for cytokine secretion assay via conventional methods, such as enzyme-linked immunosorbent spot (ELISpot), is highly laborious, time-consuming, and prohibits rapid immune status monitoring. Thus, measuring cytokines in cell culture medium using label-free biosensors integrated with microfluidic system provides great potential to simplify and accelerate the assay procedure.

Stybayeva et al. demonstrated cell secretion assay using a label-free SPR detection platform incorporating a PDMS based fluidic system (Figure 2.8.a). The platform enabled CD4+T cell separation, stimulation, and incubation and measured CD4+ T cell secreted inflammatory cytokine IFN-γ [73]. The authors used this platform to perform in situ cell secreted cytokine measurements and envision that this might be a potential future device for label-free, sensitive cytokine detection by a desired cell subset. Although the concept of this study has high potential for cytokine secretion assay, the

transferring of cell-secreted samples into SPR detecting platform requires additional process.

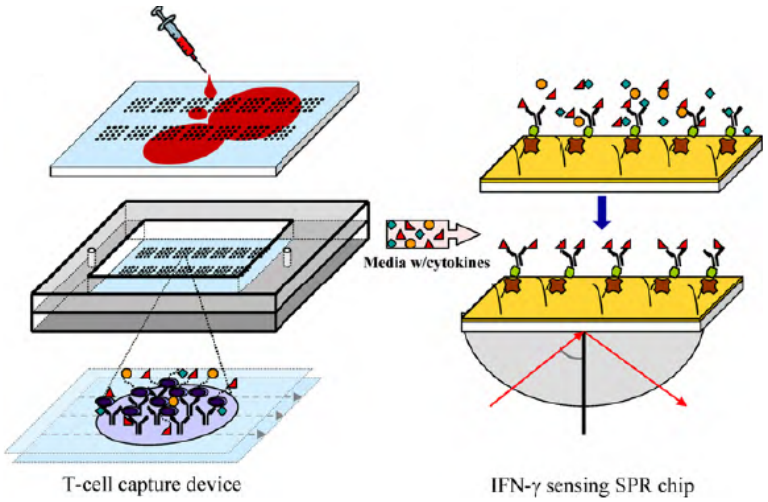

Figure 2.8: Schematic of SPR biosensors integrated with PDMS fluidic system. A glass slides coated with anti-CD4 antibody spots are enclosed inside a flow chamber and exposed to RBC-depleted human blood. Selected CD4 T-cells are activated in situ to secrete cytokines and detected with SPR chip [73].

It has been suggested that biosensor integrated microfluidic systems could overcome the practical limitations of conventional assay techniques and the approach [73] as introduced above. Specifically, biosensing can be performed with on-chip isolation and confinement of cells under microfluidic environments. Revzin's group is a leader in this field and has presented several studies showing these merits. The group developed an integrated apatamer-based amperometric biosensing platform by closely placing immune cells trapped in a microfluidic chamber (Figure 2.9.a). This study demonstrated continuous monitoring of cell secreted IFN-γ or TNF-α [74, 75] and simultaneously detected multiplexed cytokines [76]. Another study demonstrated by the same group developed a microfluidic device using a vacuum actuated PDMS valve structure that provides CD 4 T-cell incubation and label-free detection of cell secreted cytokine detection simultaneously (Figure 2.9.b) [77]. By opening the PDMS valve structure, cell-

secreted cytokines were diffused into the detection chamber. Aptamer-immobilized electrodes in the detection chamber quantified the target cytokine. The same group further designed a similar device platform and demonstrated continuous monitoring of both IFN-γ and TNF-α secreted from T-cells [76]. A more recent study showed intercellular communication of immune cells (Figure 2.9.c) [78]. Two serially connected microfluidic chambers were prepared and each chamber offered an enclosed microenvironment. The upstream chamber contained mitogen-activated monocytes, while downstream chamber kept inactive monocytes. Once TNF-α secreted from the upstream cells reached an adequate level, a PDMS valve was opened and the TNF-α molecules were diffused into the other chamber. The study observed the activation of the initially inactive monocytes by TNF-α.

Offering a confined volume of cells in an enclosed microenvironment is particularly beneficial for label-free biosensors facing limited sensitivity. The small volume of the enclosed microenvironment easily results in enhanced concentration of cell-secreted cytokine. As a result, this feature enables compensating the limited sensitivity of the biosensors. Continuous monitoring of cell-secreted cytokine measurement by label-free biosensors integrated in a microfluidic system enables us to obtain the cytokine secretion rate of the confined cells. Furthermore, extracting the secretion rate from the initial slope of the cytokine production curve could provide a way to rapidly characterize the cellular response while eliminating the long incubation time. To summarize, by integrating a microfluidic system with a label-free biosensing technique, the platforms could provide more practical or technical advantages for cytokine detection as well as cytokine secretion assay.

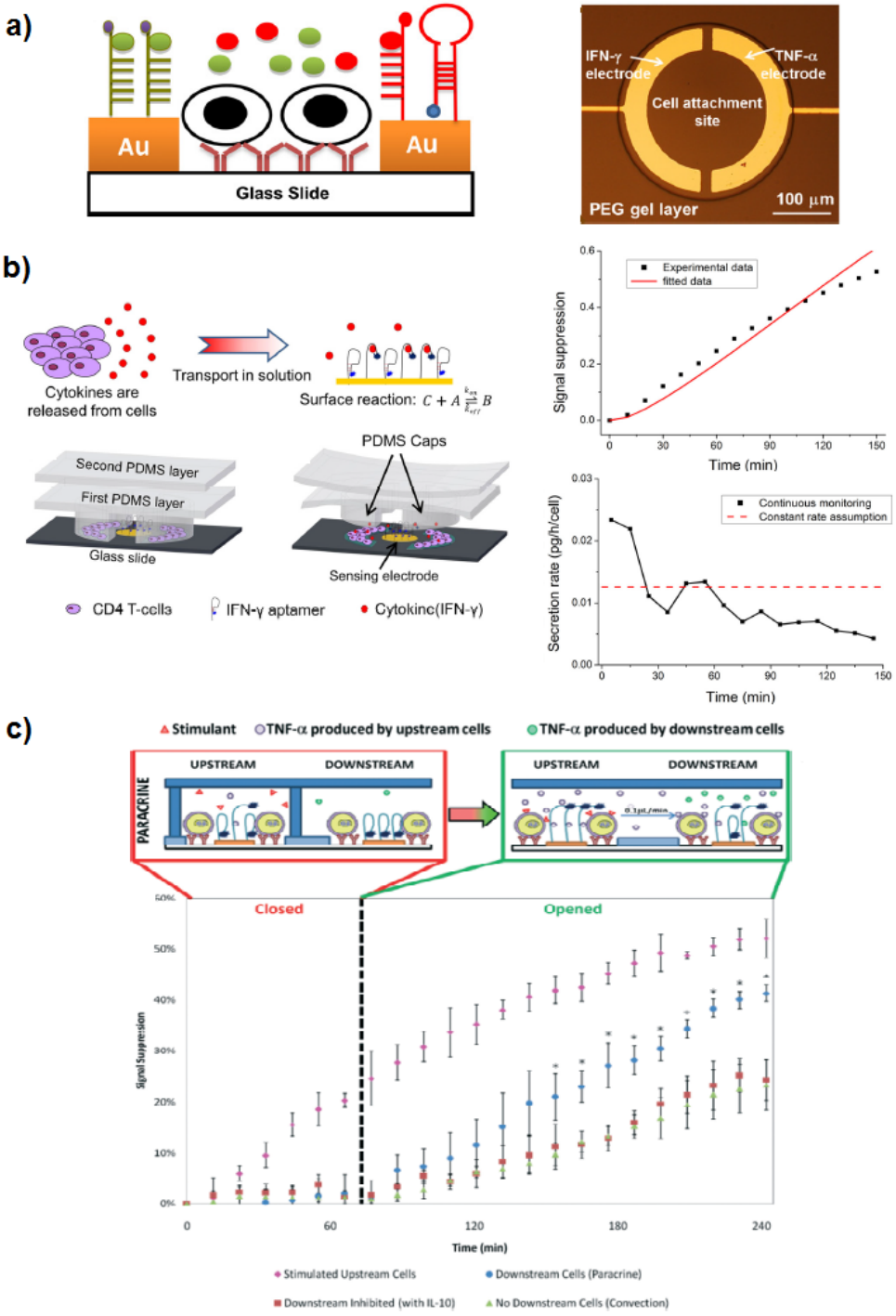

Figure 2.9: a) Aptamer-based cell-secreted cytokine detection platform from Revzin's group [76]. b) Cell secretion signals measured from aptamer-modified electrodes are a function of diffusion and surface binding of the detected molecules. The device was used to measure IFN-γ secretion. Using this approach, we recorded continuous cell-secreted cytokine concentration and experimentally determined secretion rates at different time intervals during a cell secretion experiment [77]. c) Schematic figure of device platform for monitoring cellular crosstalk using reconfigurable microfluidic devices and time dependent TNF-α secretion was monitored [78].

Chapter 3

MoS_2 Based FET Biosensors for Cytokine Biomarker Detection

3.1 Introduction to the Study

Researchers developed nanowires (NWs) and carbon nanotubes (CNTs) based field-effect transistor (FET) biosensors for detecting cancer biomarkers in a range from nM to fM in serum [44-49], proteins in cell growth system was detected of nM level in vitro [50, 51], and affinities/kinetics of protein interactions was quantified with fM-level sensitivities [52]. The fM-level limit-of-detection (LOD) offered by nanoscale FET biosensors for detecting biomarkers would enable label-free, single-molecule-level detection of trace-level amount of biomarkers. The arrays of such biosensors with consistent transistor responses could be used as reliable lab-on-a-chip platforms for precisely determining the kinetics of various biomolecule interactions. However, serious limitations imposed on nanofabrication prohibit the reliable manufacturing of the affordable biosensor chips utilizing one dimensional (1D) nanostructures [44, 48]. In particular, high-quality, small-size NWs and CNTs are required to make biosensors for

concentration monitoring (or single-molecule-level LOD for trace-level amount detection) with fM-level LOD [79]. In particular, for trace-level amount detection, the critical dimensions of the sensing channels need to be comparable to the impact dimensions of charged molecules to maximize the gating effect coming from the charged molecules and achieve very low LOD [47, 55, 56]. CNTs and many NWs are typically produced by bottom-up synthesis methods (*e.g.*, chemical vapor deposition (CVD)). Currently, proper top-down planar nanofabrication processes are limited to produce ordered arrays of such nanostructures, which makes it very challenging to provide parallel high-throughput assay biosensors made from these nanostructures. High-quality Si NW biosensor arrays are able to be fabricated by top-down lithographic techniques [52]. However, the fabrication process of such Si NW arrays usually requires expensive semiconductor-on-insulator (SOI) substrates and exquisite nanolithographic tools, which can result in a high processing cost. Furthermore, due to the high cost, using SiNW biosensor arrays are not very suitable for manufacturing affordable (even disposable) assay chips for practical clinical biosensing applications.

Recently, emerging two-dimensional (2D) atomically layered materials, including graphene, topological insulators (TIs), and TMDCs, attracted a great deal of interest because of their attractive electronic/ optoelectronic properties, large abundance, and compatibility to planar nanofabrication processes [24-35]. Due to their atomically thin layered structures, their transport properties are highly sensitive to the external stimuli, which enable new ultrasensitive 2D FETs suitable for biosensing applications [36-40]. The transistor-based on MoS_2 and other atomically layered semiconductors are expected to show much more sensitive electrical responses in antigen-antibody binding events in

comparison with the conventional transistors made of bulk semiconductors (*e.g.*, Si and III-V compounds). Moreover, all 2D layers have an extremely low density of dangling bonds on their surfaces, which result in high-quality FET channels with low densities of scattering centers (and hence low Flicker noise level), and enable highly sensitive, low-noise-level to detect biomolecules [37, 80-83]. Novoselov *et al.* have established graphene-based FET sensors capable of detecting individual gas molecules absorbed on the graphene channels [84, 85].

In contrast to graphene with zero-bandgap, semiconducting TMDCs (*e.g.*, MoS2) have sizable bandgaps. Therefore, TMDC-based FETs show high On/Off current ratios up to 10^8. This feature, in combination with their atomically thin structures, potentially enables higher detection sensitivities for gas, chemical, and biological sensing applications in comparison with graphene FETs [23, 58, 59]. Wang *et al.* and Sarkar *et al.* recently demonstrated that FET biosensors made into microscale with few-layer-MoS_2 flakes show 100– 400 fM LODs for detecting cancer-related biomarkers [23, 60]. These previous works strongly imply that such TMDC-based FET biosensors may not require sensing channels of nanoscale width to achieve fM-level LODs for concentration monitoring, and the fabrication of such biosensors would not need delicate nanolithographic tools. In addition, several recent nano-manufacturing-related works suggest that monolayer/few-layer TMDC structures and other relevant atomically layered materials have significant potential to be produced over large areas on low-cost substrates (*e.g.*, glass, plastic, or rubber) by utilizing cost-efficient processes such as CVD followed with roll-to-roll transfer[86], addressable deposition[87], and microscale stamping[88-90].

Therefore, it is very promising to develop cost-efficient manufacturing of multiplexing assays based on TMDC transistor arrays in the future.

Toward such predicted bio-assay capability, additional device-oriented research is needed for quantitatively calibrating the sensor responses from multiple sets of TMDC FET biosensors. The calibrated response signals, which are consistent with each other, can synergistically enable precise quantification of biomarker concentrations (or amounts) as well as the affinities/kinetics of biomolecule interactions. Although individual MoS_2 FET biosensors have been fabricated and exhibited very high detection sensitivity[23, 60], the exploitation of multiple devices for quantifying the biomolecule interactions has not been attempted.

In this work, we fabricated multiple sets of MoS_2-based transistor biosensors and validated that these devices can be synergistically utilized to measure the concentrations of analyte in the solutions as well as the affinity and kinetic properties of the analyte-receptor pair. TNF-α, a biomolecule under study, is a pro-inflammatory cytokine and a key biomarker associated with host defense and immunosurveillance [91-94]. Researchers pointed out that TNF-α secreted from immune cells after stimulated with lipopolysaccharide (LPS) – an endotoxin causing septic shock due to severely pronounced immune response of the human body – reflects a functioning innate immune response[95, 96]. All our biosensors exhibited a TNF-α detection limit as low as 60fM despite the small molecular size of the cytokine biomarker (~17kDa) that renders its label-free detection at high sensitivity significantly challenging. Such a low detection limit was obtained in both linear and subthreshold regimes of the transfer characteristics of MoS_2 transistors. In both transport regimes, the electrically measured sensor responses

were calibrated into signal quantities which is independent of the transistor performance. All sets of transistor biosensors showed consistent relationships between calibrated sensor responses and TNF-α concentrations. They produced a standard curve, from which the equilibrium constant of the antibody-(TNF-α) pair was extracted to be K_D=369±48fM. Based on this calibrated sensor, the time-dependent association-dissociation kinetics of the (TNF-α)-antibody pair was further scrutinized and the association/dissociation rates of the (TNF-α)-antibody pair were calculated to be $(5.03\pm0.16)\times10^{8}$ M−1s−1 and $(1.97\pm0.08)\times10^{-4}$ s−1, respectively.

3.2 Materials and Methods

3.2.1 Fabrication and Characterization of MoS_2 transistor biosensor

The MoS_2 transistors were fabricated using a previously reported microprinting method.[57] Few-layer-MoS_2 channel thicknesses were specifically prepared to be 15–20 nm. Such a MoS_2 thickness range has been validated to be in the optimal field-effect mobility values for MoS_2 transistors [97, 98]. The transistor channel lengths (*L*) were ~5 μm and the widths (*W*) ranged from 5 to 8 μm. Ti (5nm)/Au (50nm) paired electrode was served as drain (D) and source (S) contacts, which were facbricated using photolithography followed with metal deposition and lift-off. For the back gate (G), p+-Si substrates were prepared and thermally grown SiO_2 layers (300 nm thick) were used as the back-gate dielectrics. This 300 nm thick SiO_2 layers enable us to quickly identify MoS_2 flakes with suitable thicknesses (*i.e.*, 15–20nm) via a simple color coding method [99]. All electrical measurement processes were performed using an HP-4145B semiconductor parameter analyzer.

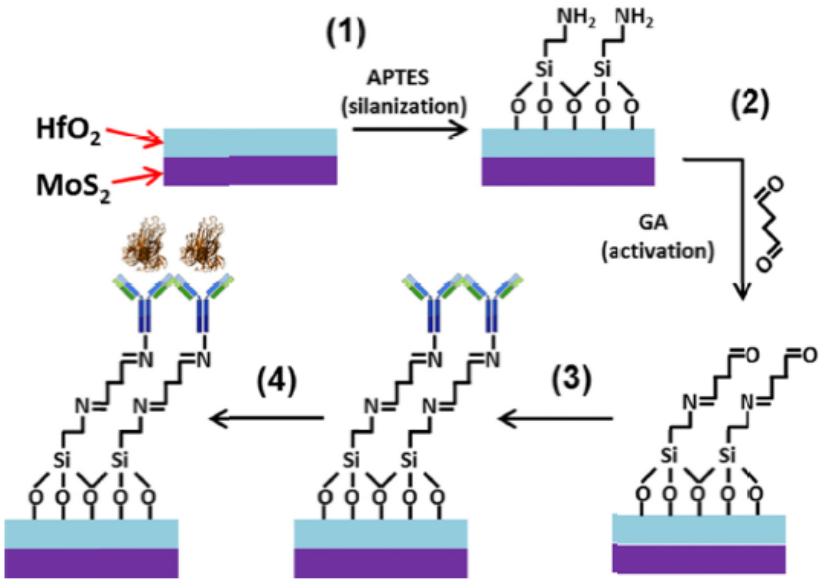

Figure 3.1: Protocol to functionalize a MoS_2 transistor sensor with anti-human TNF-α antibody receptors for detecting TNF-α biomarkers: (1) Immerse the HfO_2-coated MoS_2 transistor sensor into 5% APTES solution and incubate for 1 hour. (2) The HfO_2 surface silanized with APTES reacts with a 5% solution of glutaraldhyde (GA) in PBS for 2 hours, forming chemical linker for antibody binding. (3) Then the HfO_2 surface is incubated with an anti-human TNF- α antibody solution for 1 hour. (4) The as-functionalized sensor is incubated with solutions containing TNF- α with incremental concentrations (2 hours for each concentration) to study the sensor responses at the equilibrium state and the affinity of the (TNF- α) –antibody pair, or the device is subjected to a TNF- α flow in a microfluidic channel for quantifying the time-dependent association/dissociation kinetics of the (TNF- α) –antibody pair.

3.2.2 Bio-functionalization of MoS_2 transistor biosensor

Figure 3.1 elucidates the protocol for functionalizing the HfO_2 effective layer of a MoS_2 transistor sensor with anti-human TNF-α antibody receptors to detect TNF-α molecules. First, pre-fabricated transistor biosensor is immersed in 5% (3-Aminopropyl) triethoxysilane (APTES, Sigma-Aldrich Co. LLC.) in ethanol for 1hour to salinize the HfO2 effective layer with an APTES monolayer. After the incubation, the sensor is rinsed with phosphate buffered saline (PBS) and blown dry by nitrogen gas. The device is subsequently immersed in 5% gluteraldehyde (GA, Sigma-Aldrich Co. LLC.) in PBS for 2 hours followed by rinsing with PBS and brown dry by nitrogen gas. Afterwards, 10 μL of anti-human TNF-α antibody (eBioscience, Inc.) of 50 $\mu g/mL$ concentration in

deionized (DI) water is dropped on the sensor and incubated for 1 hour. To study the equilibrium-state sensor responses, the as-functionalized sensor is incubated with TNF-α solutions with various concentrations (*i.e.*, *n*=60fM, 300fM, 600fM, 3pM, and 6pM; the incubation time for each of the concentrations: ~2 hours). The incubation is performed using the setup shown in Fig. 3.2 (d). After each incubation process, the transfer characteristics of the transistor sensor are examined.

3.2.3 Quantification of the time-dependent association/dissociation kinetics of the (TNF-α)-antibody pair

An as-functionalized MoS_2 transistor biosensor is covered with a polydimethylsiloxane (PDMS) layer containing a microfluidic channel (10 mm in length, 200 μm in width, 50 μm in height), as illustrated in Fig. 3.2 (e). A motorized syringe infusion pump is used to drive the analyte flows into and out of the microfluidic channel through an inlet/outlet tubing (tube diameter: 0.75mm). At the beginning of the measurement of a real-time sensor response curve associated with (TNF-α)-antibody binding, DI water is injected into the sensor with a flow rate of 5 μL/min. At the same time, the MoS_2 transistor is biased under a given V_G and V_{DS}. After the I_{DS} value gets stabilized, the analyte solution with a specific concentration of TNF-α is injected into the sensor.

3.3 Results and Discussion

3.3.1 Developed MoS_2 Transistor Biosensor

The fabrication processes of transistor biosensor with a few-layer MoS_2 sensing channel are illustrated in Figure 3.2. First, a pristine few-layer MoS_2 flake is printed onto a p+-doped Si substrate coated with 300 nm thick SiO_2 (Fig. 3.2 (a)). This printing process is the same as the method previously demonstrated by *Nam et al*.[90] The thickness of the MoS_2 flake selected for making a biosensor is specifically controlled to be 15–20 nm, aiming to achieve relatively high field-effect mobility values (μ = 20 to 30 cm2/Vs) [97, 98]. After the MoS_2 printing, metallic drain/source (D/S) contacts (5 nm Ti/50 nm Au) are fabricated using photolithography followed with metal deposition, lift-off. Then a back-gated MoS_2 transistor is subsequently formed (Fig. 3.2 (b)). To make a capacitive coupling between the microfluidic reservoir (or channel) and the MoS_2 transistor channel, a 30 nm thick HfO_2 layer is deposited on the top of the MoS_2 channel via atomic layer deposition (ALD) (Fig. 3.2 (c)). Also this HfO_2 layer serves as an effective layer for biofunctionalization. Additionally, 100 nm thick SiOx is sputtered on D/S contacts to minimize the current leakage between D/S contacts and microfluidic components (Fig. 3.2 (c)). Before the TNF-α sensing, anti-human TNF-α antibody is functionalized on the HfO_2 effective layer. The detailed antibody functionalization procedure is illustrated in Fig. 3. 1. A large open liquid reservoir made from polydimethylsiloxane (PDMS) is integrated on top of the MoS_2 transistor (Fig. 1(d)) to measure the MoS_2 transistor sensor responses from different TNF-α concentrations under the thermodynamic equilibrium condition and determine the affinity of the (TNF-α) – antibody pair. This setup is simple and enables the rapid loading of various analyte

solutions. To measure the association-dissociation kinetics of (TNF-α)–antibody pair, a microfluidic channel is integrated on top of the transistor sensor, and a motorized syringe pump is used for driving the TNF-α solution flow through the microfluidic channel (Fig. 3.2 (e)). Such a setup enables stable laminar flows of analyte solutions and minimize the noise induced by the liquid loading processes, which is required for precisely analyzing the real-time kinetic processes of antibody-(TNF-α) binding. Also Figures 3.2 (d) and (e) show the circuit setups for measuring the transistor sensor responses. In addition, Fig. 3.2 (f) illustrates the cross-sectional view of a MoS_2 transistor sensor for the TNF-α sensing. Other device fabrication and characterization details were already described in the previous section 3.2.

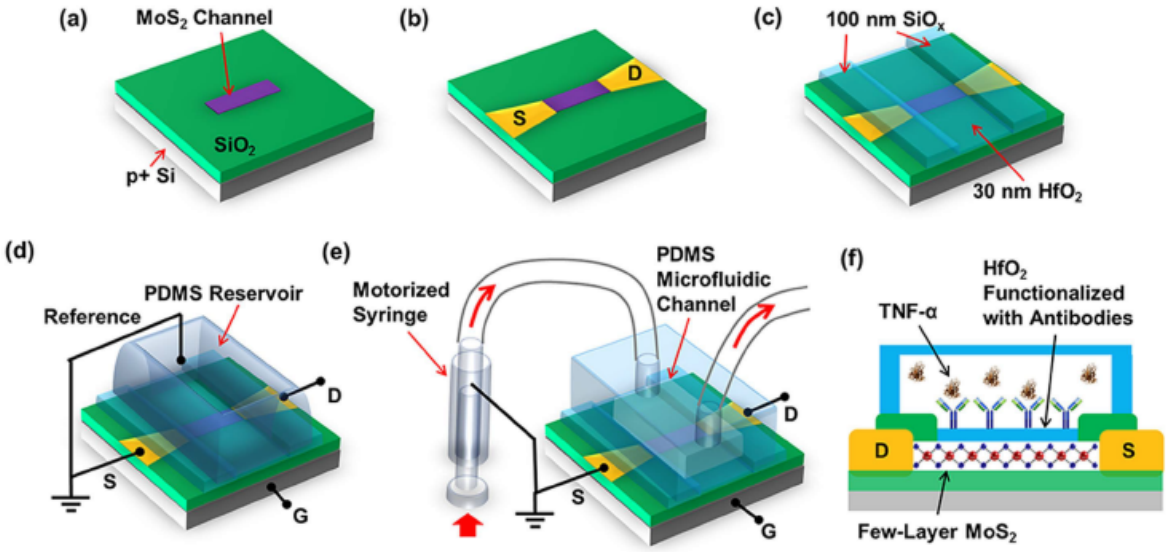

Figure 3.2: Flow chart for fabricating MoS_2 transistor biosensors: (a) printing of a few-layer MoS_2 flake onto a p+-Si/SiO2 substrate; (b) fabrication of Ti/Au D/S contacts; (c) ALD growth of the HfO_2 effective layer on top of the MoS_2 channel and coating of D/S contacts with thick SiO_x layers; (d) integration of a PDMS liquid reservoir on top of a MoS_2 transistor biosensor for measuring sensor responses from different TNF-α concentrations under thermodynamic equilibrium condition and determining the affinity of the (TNF-α)-antibody pair; (e) integration of a microfluidic inlet/outlet tubing kit driven by a motorized syringe pump on top of a biosensor for quantifying the association-dissociation kinetics of the (TNF-α)-antibody pair.

Figure 3.3 (a) shows the optical micrograph (OM) of an exemplary MoS_2 transistor with channel length (L) and width (W) of 5 and 6 µm, respectively. Figure 2 (b) displays the photograph of an as-fabricated MoS_2 transistor biosensor integrated with a PDMS liquid reservoir. The reservoir is ~4 mm deep and is ~1 mm in diameter, which is punched into a PDMS block with length, width, thickness of 2, 1, and 0.4 cm, respectively. Figure 3.3 (c) shows the photograph of a biosensor integrated with a microfluidic channel coupled with an inlet/outlet tubing kit. Other details about the dimensions of PDMS fluidic components are illustrated in the previous section 3.2.

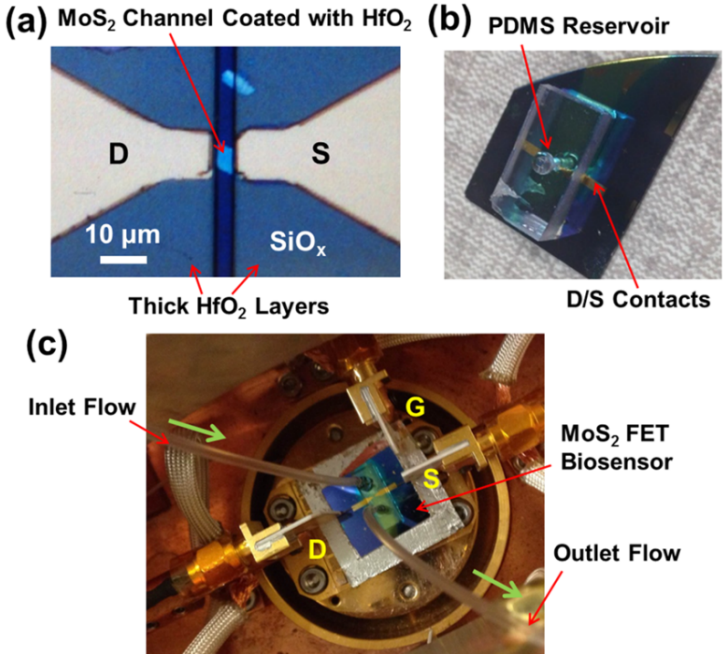

Figure 3.3: Optical micrographs or photographs of (a) an exemplary MoS_2 transistor with channel length (L) of 5 and width (W) of 6 µm, respectively; (b) an as-fabricated MoS_2 transistor biosensor integrated with a cylindrical liquid reservoir, which is punched into a PDMS block and is ~4 mm deep and is ~1 mm in diameter; (c) a biosensor integrated with a microfluidic channel connected with an inlet/outlet tubing kit, which is driven by a motorized syringe infusion pump.

First we detected the sensor responses from different TNF-α concentration under the thermodynamic equilibrium condition. The biosensor setup shown in Fig. 3.3 (b) is used for this measurement. For each transistor biosensor, the static transfer features (*i.e.*,

drain-source current (I_{DS}) – back gate voltage (V_G) curves acquired under a fixed drain-source voltage (V_{DS})) are measured at each stage, following the sequence of (1) bare transistor, (2) antibody functionalization, and introduction of TNF-α solutions with concentrations of (3) 60 fM, (4) 300 fM, (5) 600 fM, (6) 3 pM, and (7) 6 pM. To exclude the effect of the I_{DS}-V_G hysteresis, all I_{DS}-V_G curves are collected by sweeping V_G from -100 V to 100 V with a sweep rate of 10 V/s. Other details about different stages and transistor characterizations are described in the previous section 3.2.

3.3.2 Sensor Responses Measured in the Linear Transport Regimes of MoS_2 Transistor Biosensors

Figure 3.4 exhibits the sensor responses measured in the linear transport regimes of MoS_2 transistor sensors. Specifically, Fig. 3.4 (a) shows the transfer characteristics of an exemplary sensor measured at various detection stages, and the I_{DS} data are plotted in the linear scale. The transfer characteristics of this sensor show a strong dependence on TNF-α concentrations, and the TNF-α detection limit is estimated to be ~60 fM. We choose a fixed value for V_G within the linear regimes of all I_{DS}-V_G curves (*e.g.*, V_G = 98 V, as denoted by the dashed vertical line in Fig. 3. 4 (a)). The I_{DS} values measured under this V_G change according to different detection states and such I_{DS} data could be utilized as a sensor response signal. However, such a response signal is highly rely on the transistor performance parameters (*e.g.*, transconductance (g_m) and threshold voltage (V_T)). Therefore, in the analysis of a given detection state, the I_{DS} signals attained by different MoS_2 transistors may exhibit a poor device-to-device consistency due to the non-uniformity of MoS_2 transistors. Although such an issue could be eliminated through

optimizing the material deposition and device fabrication processes. It is highly desirable to calibrate sensor response quantity independent to the device performance.

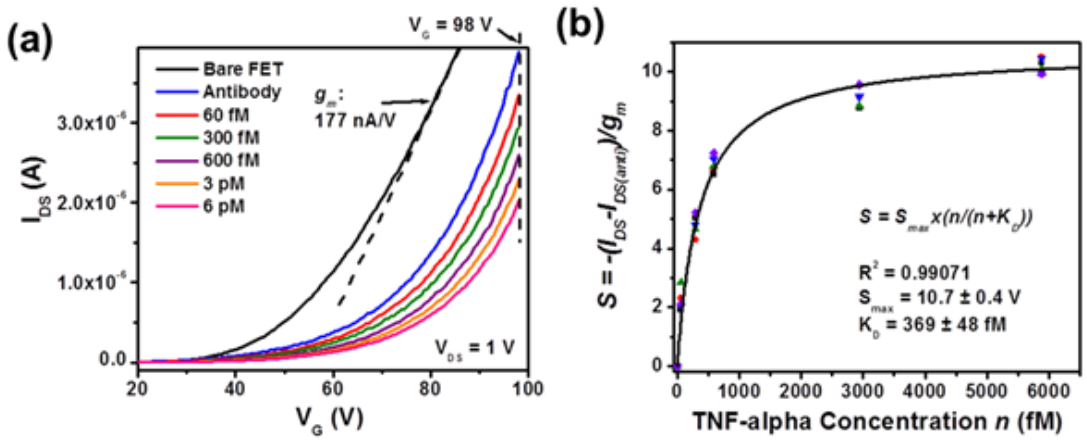

Figure 3.4: Sensor responses collected in the linear transport regimes of MoS_2 transistor biosensors. (a) Transfer characteristics of an exemplary MoS_2 transistor sensor detected at various biodetection stages, following the sequence of (1) bare transistor, (2) antibody functionalization, and inputs of TNF-α solutions with concentrations of (3) 60 fM, (4) 300 fM, (5) 600 fM, (6) 3 pM, and (7) 6 pM. (b) A set of calibrated linear-regime responses (S) measured from five different MoS_2 transistor sensors with respect to TNF-α concentration from 60 fM to 6 pM (n). These S-n relationships well fitted with Langmuir isotherms and the dissociation constant (K_D) of the (TNF-α)- antibody pair is extracted to be 369+48 fM.

The linear regime of an I_{DS}-V_G characteristic curve collected from a microscale MoS_2 transistor sensor in a specific biodetection state expressed as Equation (3.1). In our experiments, it is detected that for a given transistor sensor, the g_m values extracted from different I_{DS}-V_G curves that correspond to different biodetection states are very close and can be approximated as a constant for this sensor. For example, the g_m value of the sensor illustrated in Fig. 3. 4 (a) is extracted to be ~177 nS at V_{DS} = 1 V. Based on this observation and Equation (3.1) and the implication from previous works achieved by Duan et al. and Ishikaw et al.[52, 100], a calibrated sensor response quantity (S) is derived and expressed in Equation (3.2). The $I_{DS(anti)}$ is the I_{DS} value measured in the "antibody functionalization" state of a sensor biased under a set of fixed V_{DS} and V_G, and I_{DS}-$I_{DS(anti)}$ indicates the I_{DS} variation induced by introducing TNF-α molecules. An I_{DS}

variation normalized by the g_m of this sensor results in a sensor response quantity directly related to the change in the V_T of the sensor (*i.e.*, ΔV_T). Although ΔV_T is assumed to be completely induced by the charge brought to the HfO_2 effective layer on the top of the transistor channel through (TNF-α)-antibody binding events, ΔV_T is not exactly the binding-event-induced potential change ($\Delta\Phi$) of the effective layer. This is because in this work, ΔV_T is the change in the V_T measured from the back gate. However, ΔV_T and $\Delta\Phi$ have relation of $\Delta V_T = (C_{HfO2}/C_{SiO2})\Delta\Phi$, where C_{SiO2} and C_{HfO2} are the capacitances of the SiO_2 back gate dielectric and the HfO_2 effective layer, respectively. More detailed discussion about this can be found from the dual-gate transistor model illustrated in Figure 3.5. Based on this model, ΔV_T is evaluated by $\Delta V_T = q d_{SiO2}\sigma_{TNF}/k_{SiO2}\varepsilon_0$, where q is the effective charge carried by a TNF-α molecule; d_{SiO2} and k_{SiO2} are the thickness and dielectric constant of the SiO_2 back-gate dielectric layer, respectively; ε_0 is the vacuum permittivity; and σ_{TNF} is the area density of TNF-α molecules bound to the receptor antibody-functionalized effective layer. Therefore, a calibrated response quantity (S) is proportional to the antibody receptor occupancy at the equilibrium state and it is also independent of the MoS_2 transistor performance. These two conditions are critical for the subsequent Langmuir isotherm analysis.

$$I_{DS} = g_m(V_G \quad V_T \quad \frac{V_{DS}}{2}) \tag{3.1}$$

$$S = \frac{I_{DS} \quad I_{DS(anti)}}{g_m} = \quad V_T = \frac{q d_{SiO2} \quad TNF}{k_{SiO2} \quad 0} \tag{3.2}$$

Figure 3. 4 (b) plots the calibrated responses obatined from the linear transport regimes of five different sensors with respect to TNF-α concentration (n). The detailed transfer characteristics of these five devices measured at various biodetection stages are

displayed in Figure 3. 6. Although Figure 3. 6 displays that the transfer characteristics of these five sensors exhibit significant difference in V_T, I_{DS}, and g_m, Fig. 3. 4 (b) shows that the calibrated responses from these sensors are consistent with each other and can serve as a standard curve (*i.e.*, a generic *S*-*n* curve) for TNF-α detection. This standard curve can be well matched with Langmuir isotherms (Equation (3.3)) and the equilibrium (or dissociation) constant (K_D) of the (TNF-α)-antibody pair is extracted to be 369±48 fM; the maximum sensor response (S_{max}) is extracted to be 10.7±0.4 V.

$$S = S_{\max}\frac{n}{n + K_D} \tag{3.3}$$

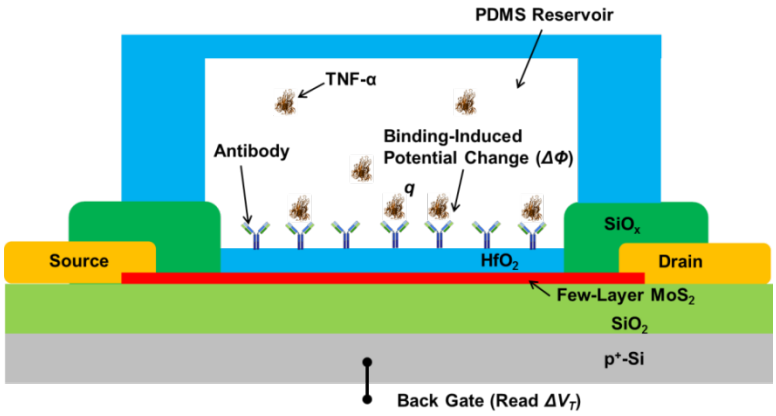

Figure 3.5: The schematic of dual-gate thin-film transistor biosensor model: The binding of TNF-α molecules with the receptor-antibody-functionalized HfO_2 effective layer cause a potential change ($\Delta\Phi$) on this effective layer. $\Delta\Phi$ can be calculated using $= \frac{qN_{TNF}}{C_{HfO2}}$, where q is the charge brought to the HfO_2 effective layer through a single (TNF-α)-antibody binding event; N_{TNF} is the total number of TNF-α molecules bound to the HfO_2 effective layer; C_{HfO2} is the total capacitance of the HfO_2 effective layer. The $\Delta\Phi$ leads a change in the conductive charge ($\Delta Q = C_{HfO2}\Delta\Phi$) in the MoS_2 channel. This ΔQ can cause a change of the threshold voltage (ΔV_T) measured from the back gate (note: not measured from the top gate), and ΔV_T can be evaluated by $\Delta V_T = \Delta Q/C_{SiO2} = (C_{HfO2}/C_{SiO2})\Delta\Phi = \frac{qN_{TNF}}{C_{SiO2}}$, where C_{SiO2} represents the capacitance of the back-gate dielectric layer. Furthermore, N_{TNF} can be obtained using $N_{TNF} = \sigma_{TNF} A$, where σ_{TNF} is the areal density of bound TNF-α molecules on the effective layer and A is the total sensor area. C_{SiO2} can be calculated using $C_{SiO2} = k_{SiO2}\varepsilon_0 A/d_{SiO2}$, where d_{SiO2} and k_{SiO2} are the thickness and dielectric

constant of the SiO_2 back-gate dielectric layer, respectively; ε_0 is the vacuum permittivity. Therefore, $V_T = \frac{qN_{TNF}}{C_{SiO2}} = \frac{qd_{SiO2\ \ TNF}}{k_{SiO2\ \ 0}}$.

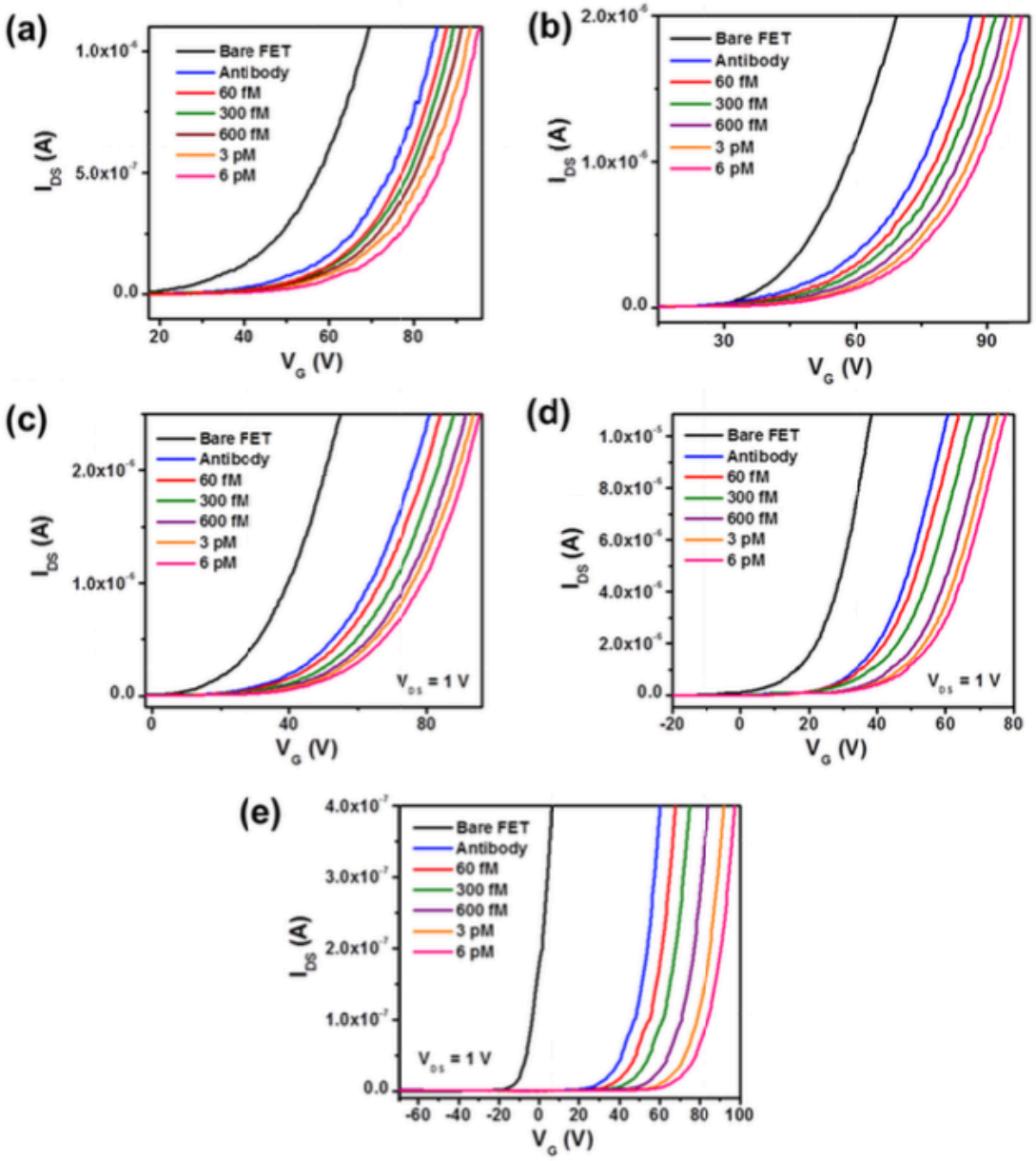

Figure 3.6: Linear-regime sensor responses at the equilibrium state. The transfer characteristics of five different MoS_2 transistor sensors measured at various detection stages: (1) bare transistor(black), (2) antibody functionalization(blue), and inputs of TNF-α solutions with concentrations of (3) 60 fM (red), (4) 300 fM (green), (5) 600 fM (purple), (6) 3 pM (orange), and (7) 6 pM (magenta). The calibrated linear-regime sensor responses from these five devices are plotted in Figure 3.4. b with respect to TNF-α concentration.

3.3.3 Sensor Responses Measured in the Subthreshold Regimes of MoS_2 Transistor Biosensors

Alternatively, sensor responses can also be defined from the subthreshold regimes of MoS_2 transistor sensors. In the subthreshold regime of a transistor sensor, the sensitivity of I_{DS} according to the electrical potential variation (or charge) at the effective layer is much higher than that in the linear transport regime of this sensor. Hence, the responses from the subthreshold regimes of transistor sensors are expected to result in the higher detection sensitivity in comparison with those from the linear regimes. Figure 3.7 (a) displays the transfer characteristics of another exemplary MoS_2 transistor sensor, which were measured at various detection stages. The I_{DS} data are illustrated in the logarithm scale, and the subthreshold regimes are emphasized. We choose a fixed V_G within the subthreshold regimes of all I_{DS}-V_G curves (*e.g.*, V_G = 29 V denoted by the vertical dashed line in Figure 3.7 (a)). The I_{DS} values measured under this V_G clearly change according to different biodetection states and show a strong dependence on TNF-α concentration. Here, the TNF-α detection limit is estimated as low as 60 fM. Similarly, I_{DS} data obtained in the subthreshold regimes of transistor sensors cannot be directly used as standard sensor responses. A calibrated subthreshold-regime response quantity independent of the transistor performance is required.

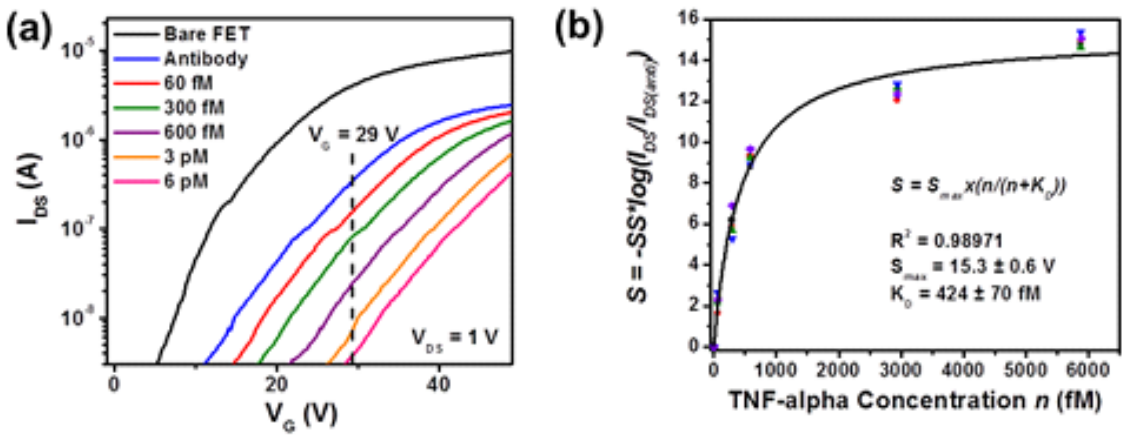

Figure 3.7: Sensor responses collected in the subthreshold regimes of MoS_2 transistor biosensors. (a) Transfer characteristics of an exemplary MoS_2 transistor sensor measured at various biodetection stages, following the order of (1) bare transistor, (2) antibody functionalization, and inputs of TNF-α solutions with concentrations of (3) 60 fM, (4) 300 fM, (5) 600 fM, (6) 3 pM, and (7) 6 pM (Here I_{DS} data are shown in the logarithm scale, and the subthreshold regimes are emphasized); (b) a set of calibrated subthreshold-regime responses (S) collected from five different MoS_2 transistor sensors with respect to TNF-α concentration (n). These S-n relationships well fitted with Langmuir isotherms and the dissociation constant (K_D) of the (TNF-α)-antibody pair is extracted to be 424+70 fM.

In the subthreshold regime of a microscale MoS_2 transistor sensor, the I_{DS}-V_G relationship detected from a specific biodetection state can be expressed by Equation (3.4). The I_T is the I_{DS} value measured at V_G=V_T under a given V_{DS}; *SS* is the subthreshold swing. As observed in our experiments, although the functionalization of a transistor sensor with receptor antibodies (*i.e.*, the transition from "bare transistor" to "antibody functionalization" states) can result in an observable reduction of the *SS* of this sensor. The *SS* value does not significantly change among the subsequent biodetection states, including the inputs of incremental concentrations of TNF-α sample. Thus, for a given as-functionalized transistor sensor, *SS* can be approximated as a constant. Based on this observation, a calibrated subthreshold-regime sensor response quantity (*S*) is derived from Equation (3.4) and articulated in Equation (3.5). In the equations, $I_{DS(anti)}$ is the drain-source current measured in the "antibody functionalization" state of a sensor biased

under a set of fixed V_{DS} and V_G; and I_{DS} is the drain-source current measured from a subsequent biodetection state (*i.e.*, a specific TNF-α concentration). Similar to the calibrated linear-regime response quantity articulated in Equation (3.2), this subthreshold counterpart is also directly related to ΔV_T, independent of the transistor performance, and proportional to σ_{TNF}.

$$I_{DS} = I_T \cdot 10^{(V_G - V_T)/SS} \tag{3.4}$$

$$S = SS \cdot \log \frac{I_{DS}}{I_{DS(anti)}} = V_T = \frac{qd_{SiO2} \quad TNF}{k_{SiO2} \quad 0} \tag{3.5}$$

Figure 3.7 (b) shows the calibrated subthreshold-regime responses (*S*) measured from five different sensors with respect to TNF-α concentration (*n*). The detailed transfer characteristics of these five devices measured at various biodetection stages are shown in Figure 3.8. As displayed in Figure 3.8, the transfer characteristics of these five sensors exhibit significant difference in V_T, I_{DS}, and *SS* parameters. However, as plotted in Fig. 3.7 (b), the calibrated *S*-*n* curves measured from these devices are consistent with each other and well fitted with Langmuir isotherms (Equation (3.3)). Here, the equilibrium constant (K_D) of the (TNF-α)-antibody pair is extracted to be 424±70 fM, which is consistent with the K_D value extracted from the linear-regime sensor responses (*i.e.*, 369±48 fM). The S_{max} value is fitted to be 15.3±0.6 V, which is about 40% larger than that extracted from the linear-regime responses (*i.e.*, 10.7±0.4 V). This observable discrepancy was not fully understood. However, this could be temporarily attributed to the different back-gate V_G levels required for biasing sensors in subthreshold and linear regimes, which could result in different magnitudes of electric field penetrating through

few-layer MoS_2 channels as well as HfO_2 effective layers and leaking into the analyte solution. This could lead to different degrees of the modification of electrical-double-layers around sensors and therefore different degrees of the screening of the charges brought through analyte-receptor binding pairs.

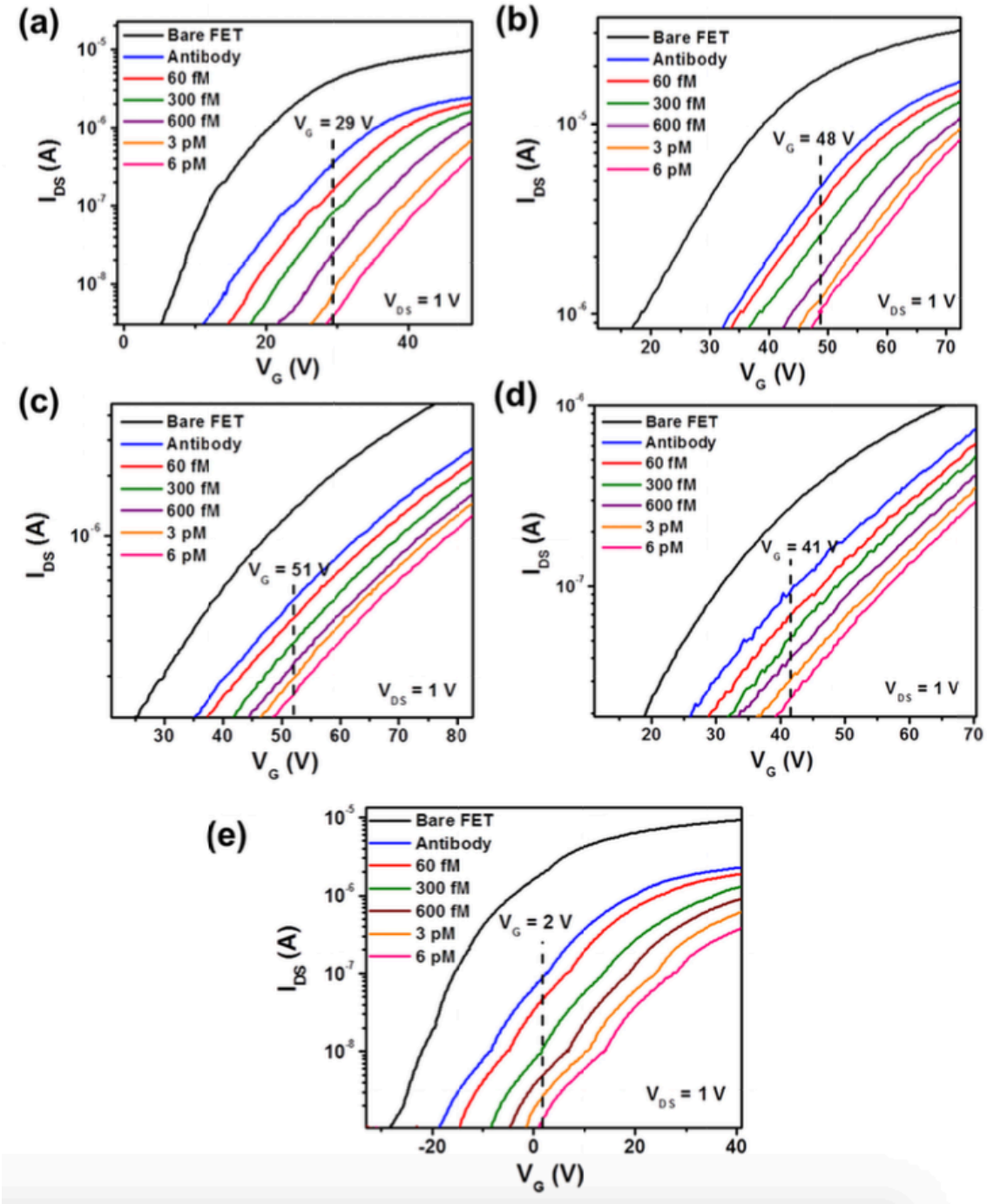

Figure 3.8: Sensor responses at the equilibrium state at subthreshold-regime. The transfer characteristics of five different MoS_2 transistor sensors detected at various biodetection stages, following the order of (1) bare transistor, (2) antibody functionalization, and inputs of TNF-α solutions with concentrations of (3) 60 fM, (4) 300 fM, (5) 600 fM, (6) 3 pM, and (7) 6 pM. The calibrated subthreshold-regime sensor responses from these five devices are shown in Fig. 3.7 (b) with respect to TNF-α concentration.

3.3.4 Sensitivity Data acquired from both Linear and Subthreshold Regimes

Although the I_{DS} signals collected from both linear and subthreshold regimes can be mathematically normalized to consistent device-independent response quantities using Equations (3.2) and (3.5). The physical limit-of-detection of a transistor biosensor is indeed determined by the sensitivity of I_{DS} to the variation of analyte concentration (dn) and the noise level of electrically measured I_{DS} signals. This I_{DS} sensitivity is quantitatively defined as the relative change in I_{DS} per change in n (*i.e.*, $Sensitivity = \frac{dI_{DS}}{I_{DS}}/dn$). Figure 3.9 illustrates and compares the sensitivity data obtained from (a) the linear-regime I_{DS} signals measured from the five sensors shown in Fig.3.6 and (b) the subthreshold-regime I_{DS} signals from the five sensors shown in Fig. 3.8. All differential sensitivity values are collected at TNF-α concentration of n = 60 fM. This provides critical information about the sensitivity required for obtaining fM-level detection limits. Figure 3.9 displays that the subthreshold-regime I_{DS} sensitivities (0.52$\pm$0.3 %/fM) are statistically higher than the linear-regime I_{DS} sensitivities (0.14$\pm$0.02 %/fM). Therefore, subthreshold-regime sensor responses are more desired in achieving high detection sensitivity. However, we should aware that the ultimate detection limit of a transistor sensor is also restricted by the signal-to-noise ratios of electrically measured I_{DS} signals. Furthermore, to detect low-abundance molecules, the non-specific adsorption of target

molecules could also strongly affect the detection limit. The further study of these aspects is beyond the scope of this work but will be addressed in the future research.

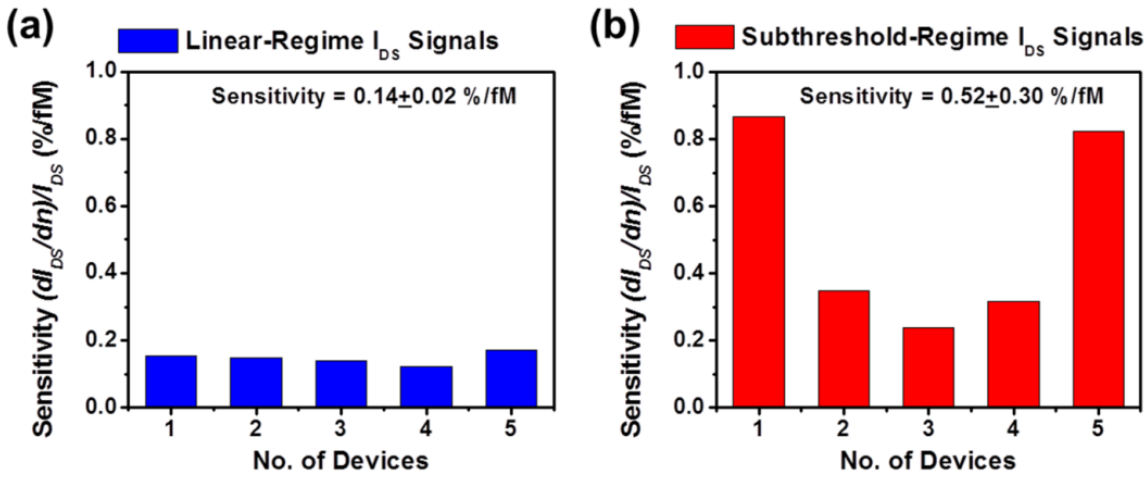

Figure 3.9: Sensitivity data obtained from (a) the linear-regime I_{DS} signals measured from the five sensors shown in Fig. 3.6 and (b) the subthreshold-regime I_{DS} signals measured from the five sensors shown in Fig. 3.8. All differential sensitivities were calculated at TNF-α concentration of n = 60 fM (*i.e.*, $Sensitivity = \frac{1}{I_{DS}}\left(\frac{dI_{DS}}{dn}\right)|_{n=60\,fM}$).

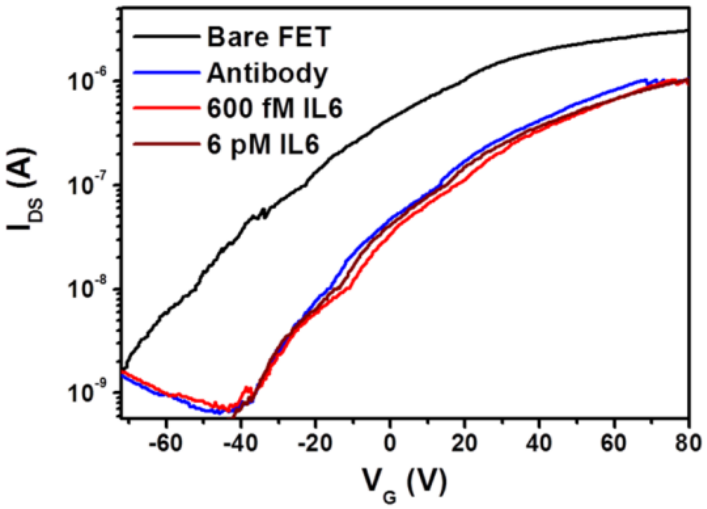

Figure 3.10: A negative control test of the specificity test of MoS_2 transistor biosensors: The transfer characteristics of a control sensor measured at stages of (1) bare transistor, (2) antibody functionalization (functionalized with anti-human TNF-α receptor antibodies), and inputs of IL-6 solutions with concentrations of (3) 600 fM and (4) 6 pM.

3.3.5 Developed Biosensor Specify test to the target molecule

To calculate the detection specificity of our MoS_2 transistor sensors, a sensor functionalized with anti-human TNF-α antibody is used for detecting interleukin-6 (IL-6) cytokine. Figure 3.10 displays the transfer characteristics of this sensor measured at various stages, including (1) bare transistor, (2) antibody functionalization, and inputs of IL-6 solutions with concentrations of (3) 600 fM and (4) 6 pM. Figure 3.10 shows that the presence of IL-6 that is not specific to TNF-α antibody did not induce prominent change in the transfer characteristics. Such experimentally observed weak sensor responses to IL-6 indicate a negligible nonspecific adsorption of IL-6 molecules on the sensor surface. This may represents an effectively blocking of the densely-packed self-assembled monolayers of APTES on HfO_2 effective layers.

3.3.6 Time-dependent Association/Dissociation Kinetics of the (TNF-α)-Antibody Pair

The biosensor setup illustrated in Fig. 3.3 (c) is used for measuring the time-dependent association/dissociation kinetics of the (TNF-α)-antibody pair. The details about microfluidic liquid handling and data recording are described in the section 3.2. Figure 3.11 (a) shows real-time sensor responses of (TNF-α)-antibody binding measured under different TNF-α concentrations (*i.e.*, n = 60 fM, 600 fM, 3 pM, and 6 pM). Each of the time-dependent response curves was collected from a different MoS_2 transistor sensor and all sensor responses were normalized using $S = SS \cdot \log\left(I_{DS}/I_{DS(anti)}\right)$ (*i.e.*, Equation (3.5) to calibrate subthreshold-regime responses). Figure 3.12 illustrates the detailed transfer characteristics of these transistor sensors measured before the input of

TNF-α samples, from which the required *SS* parameters were obtained. Additionally, the operation points (*i.e.*, the fixed V_G and V_{DS} values, under which a real-time response curve was measured) are also labelled in Fig. 3.12. In Figure 3.11 (a), the red arrow indicates the onset time, at which the solutions with specific TNF-α concentrations were filled into the particular biosensor. The real-time response curves in Fig. 3.11 (a) show that the association rate of the (TNF-α)-antibody pair rises with increasing TNF-α concentration. The rise segment of each real-time response curve well fitted with the first-order absorption equation (*i.e.*, Equation (3.6)) [37]. In the equation (3.6), S_{eq} is the sensor response at the final equilibrium state; k_{on} and k_{off} are association and dissociation rates, respectively; $k_{on}n+k_{off}$ relates to the rising slope of the linear regime of the response curve. Table 3.1 lists the fitting results of S_{eq} and $(k_{on}n+k_{off})$ values for n = 60 fM, 600 fM, 3 pM, and 6 pM. These S_{eq} values extracted from the real-time binding responses are consistent with the sensor responses directly calculated at the equilibrium state, after a long (~2 hour) incubation process (*e.g.*, the equilibrium-state response data shown in Fig. 3.7 (b)). In particular, Fig. 3.11 (b) displays the extracted S_{eq} data as a function of TNF-α concentration, which also fitted with Langmuir isotherm. Here, the equilibrium constant (K_D) is extracted to be 326±37 fM and the maximum response (S_{max}) is calculated to be 15.6±0.2 V. Both are consistent with those extracted from the equilibrium-state subthreshold-regime responses shown in Fig. 3.7 (b).

$$S = S_{eq}(1 \quad e^{(k_{on}n+k_{off})t}) \qquad (3.6)$$

	n=60 *fM*	600 *fM*	3 *pM*	6 *pM*
S_{eq} (V)	2.07 ± 0.03	10.7 ± 0.5	13.9 ± 0.06	14.7 ± 0.13
$(k_{on}n \pm k_{off})$ (s^{-1})	$(3.68 \pm 0.15) \times 10^{-4}$	$(6.94 \pm 0.46) \times 10^{-4}$	$(1.74 \pm 0.10) \times 10^{-3}$	$(3.28 \pm 0.10) \times 10^{-3}$

Table 3.1: The fitting results of the real-time sensor response curves shown in Fig. 3.9 (a) those were fitted with Equation (3.6). The table lists the extracted S_{eq} and $(k_{on}n+k_{off})$ parameters for n = 60 fM, 600 fM, 3 pM, and 6 pM.

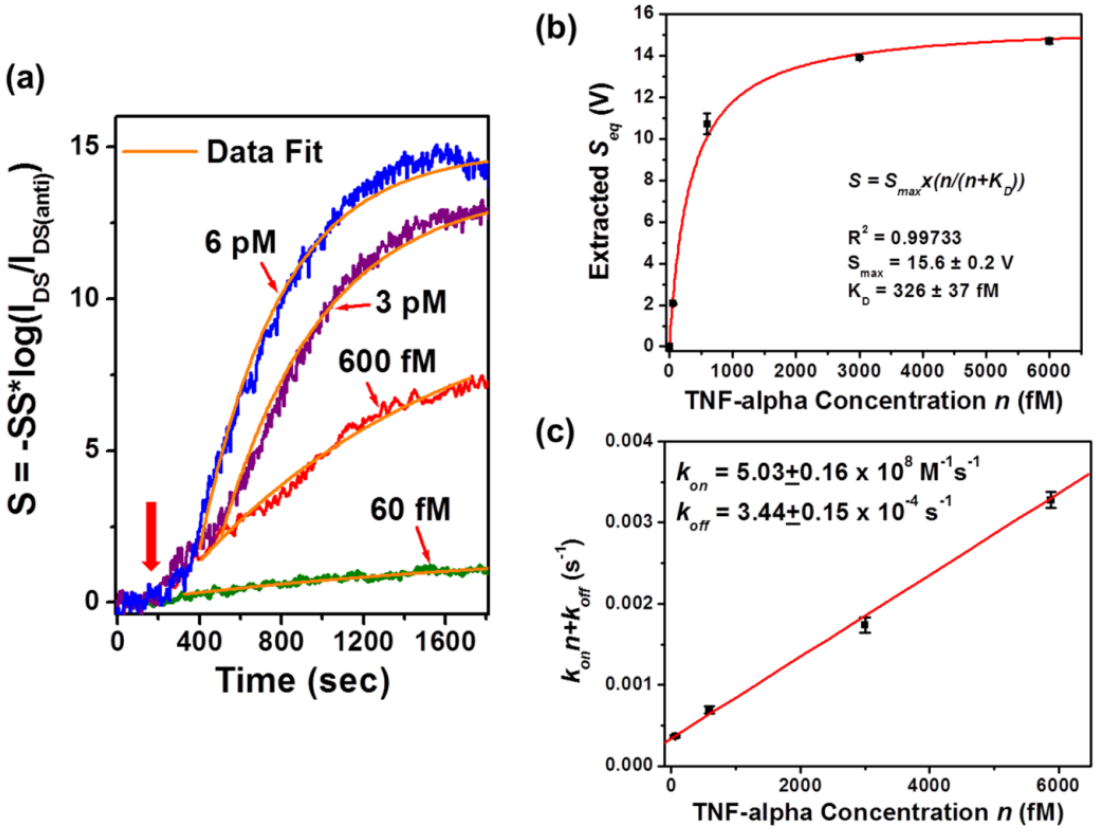

Figure 3.11: Time-dependent association kinetics of the (TNF-α)-antibody pair: (a) real-time sensor responses of (TNF-α)-antibody binding measured under different TNF-α concentrations (n = 60 fM, 600 fM, 3 pM, and 6 pM). Each of the response curves was collected from a different MoS_2 transistor sensor and all responses were normalized using Equation (3.5). The rise parts of the binding response curves are fitted with Equation (3.6). (b) The equilibrium-state responses (S_{eq}) extracted from this fitted plat was illustrated as a function of TNF-α concentration, which can be further fitted with Langmuir isotherm. The equilibrium constant (K_D) is calculated to be 326±37 fM. (c) The extracted $(k_{on}n+k_{off})$ data plotted as a function of TNF-α concentration (n). The linear fitting of this $(k_{on}n+k_{off})$-*versus*-n graph results in rate constants of k_{on} = (5.03±0.16) x10^8 $M^{-1}s^{-1}$ and k_{off} = (1.97±0.08) x10^{-4} s^{-1}.

To evaluate k_{on} and k_{off} parameters, the extracted $(k_{on}n+k_{off})$ data are illustrated as a function of TNF-α concentration (n) (see Fig. 3.11 (c)). The linear fitting concludes in rate constants of k_{on} = (5.03±0.16) x10^{8} $M^{-1}s^{-1}$ and k_{off} = (3.44±0.15) x10^{-4} s^{-1}. It was observed that this fit is not sensitive to the dissociation rate (k_{off}) because of its small numerical value. To attain a better quantification of k_{off}, we directly measured the real-time dissociation kinetics of the (TNF-α)-antibody pair. Specifically, two as-functionalized MoS_2 transistor biosensors were incubated (more than 2 hours) in solutions with TNF-α concentration of 600 fM and 3pM, respectively. The incubation time was selected so than antibody-(TNF-α) association/dissociation processes reach to the equilibrium state. Afterwards, these fully incubated sensors were rinsed with pure buffer solution and the calibrated sensor responses were recorded as a function of the lapsed time, as shown in Fig. 3.13. The Figure 3.13 illustrates that the sensor responses decreased with time, which was attributed to the unbinding events. The response curve measured from the device incubated with TNF-α concentration of 600 fM well fitted with a monoexponential decay function (*i.e.*, the desorption equation expressed in Equation (3.7)). In the equation (3.7), S_r represents the sensor response corresponding to the areal density of bound molecule residues after the desorption process. This fit results in k_{off} = (1.97±0.08) x 10^{-4} s^{-1}, from which the affinity equilibrium constant K_D is also estimated to be $K_D=k_{off}/k_{on}$= 392 fM. This K_D value is also consistent with those extracted from the equilibrium-state sensor responses (*i.e.*, K_D values extracted in Fig. 3.4 and 3.7). From this fit, S_r is calculted to be 3.0±0.2 V and S_{eq} is 9.2±0.4 V. This denotes that ~33% of bound TNF-α molecules are expected to remain absorbed on the sensor even after a long rinsing process.

$$S = \left(S_{eq} \quad S_r\right)e^{\ k_{off}t} + S_r \qquad (3.7)$$

$$S = \left(S_{eq} \quad S_2 \quad S_r\right)e^{\ k_{off}t} + S_2 e^{\ k_2 t} + S_r \qquad (3.8)$$

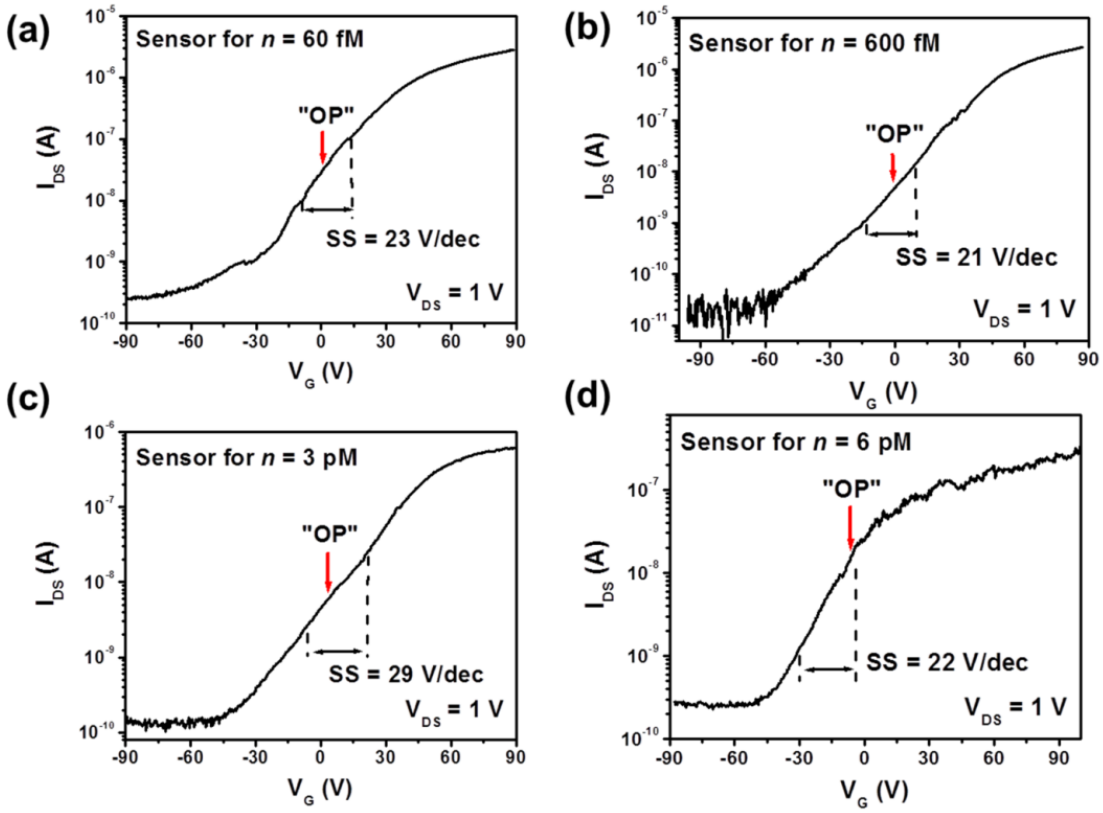

Figure 3.12: Transfer characteristics of four different MoS_2 transistor biosensors measured before introducing TNF-α samples, from which the subthreshold-swing (*SS*) parameters were obtained for normalizing the real-time subthreshold-regime sensor responses (Equation (3.5)). These sensors were utilized to quantify the real-time kinetics of (TNF-α)-antibody binding under different TNF-α concentrations (*n*) of (a) 60 fM, (b) 600 fM, (c) 3 pM, and (d) 6 pM. The operation points (OP, *i.e.*, the fixed V_G and V_{DS} values, under which a real-time response curve was measured) are marked by the red arrows.

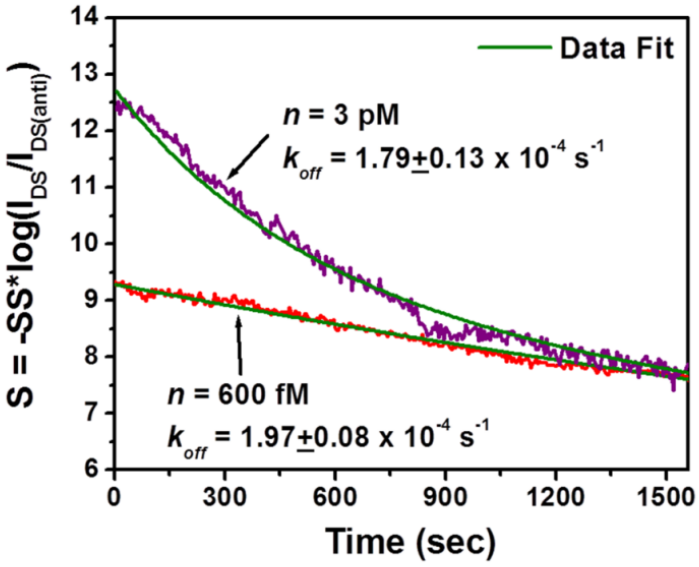

Figure 3.13: Time-dependent dissociation kinetics of the (TNF-α)-antibody pair measured from two MoS_2 transistor sensors that were incubated in solutions with TNF-α concentration of n = 600 fM and 3 pM for about 2 hours and subsequently rinsed with the pure buffer solution.

The response curve measured from the device incubated with 3 pM concentration of TNF can be hardly fitted with monoexponential Equation (3.7). We notice that it can be fitted with a bi-exponential decay equation (Equation (3.8)). As a result, S_{eq} = 13.6±1.0 V, S_2 = 4.5±0.2 V, S_r = 2.9±0.3 V, k_2 = (2.0±0.16) x 10^{-3} s^{-1}, and k_{off} = (1.79±0.13) x 10^{-4} s^{-1} as obtained. As reported by several previous works [37, 101, 102], the bi-exponential behavior of sensor response is probably due to the multivalent antigen-antibody binding, which may become more prominent with increasing the analyte concentration. This elucidation is reasonable because the antibody used in this work is polyclonal. To fully study the association/dissociation kinetics of multivalent binding processes, a more complicated model for describing (TNF-α)-antibody binding is needed.

Finally, it should be noted that for our current MoS_2 transistor sensors, the calibrated sensor responses do not explicitly rely on HfO_2 layer thickness (t_{HfO2}). All

sensors discussed above have 30 nm thickness HfO_2 effective layers. To further experimentally prove that the sensor responses of our sensors do not strongly depend on HfO_2 layer thickness (t_{HfO2}), we fabricated additional sensors with t_{HfO2} = 60 nm. Figure 3.14 (a) displays the transfer characteristics of an exemplary sensor with t_{HfO2} = 60 nm, which were measured from a set of incremental TNF-α concentrations. From such transfer characteristics, we extracted calibrated subthreshold-regime responses (S) at V_G = − 25 V (V_T ~ − 10 V) and plotted them as a function of TNF-α concentration (n) (see the red stars shown in Fig. 3.14 (b)). This S-n relationship is consistent with those measured from the sensors with t_{HfO2} = 30 nm. This result proves that the calibrated sensor response values do not strongly rely on the HfO_2 effective layer thickness.

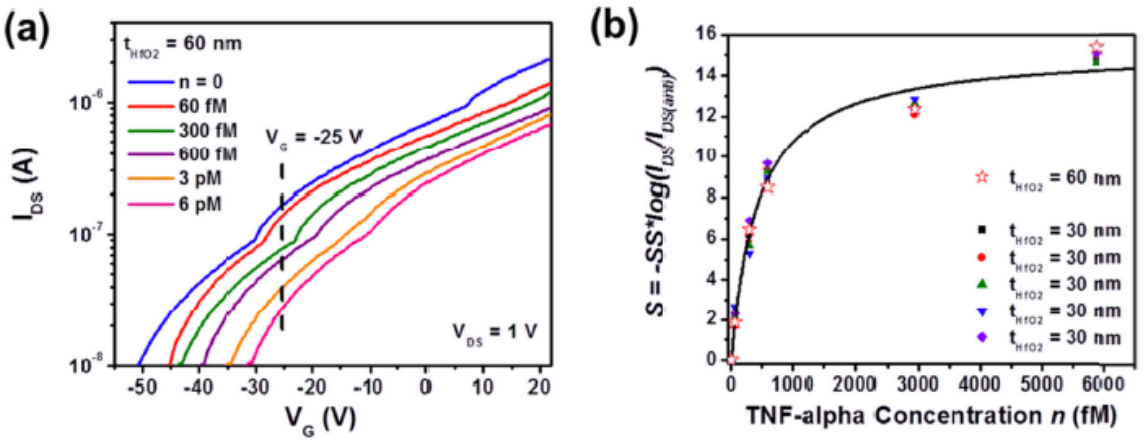

Figure 3.14: Sensor responses collected in the subthreshold regime of a MoS_2 transistor biosensor with a 60 nm thick HfO_2 effective layer (i.e., t_{HFO2} = 60nm). (a) Transfer characteristics of the MoS_2 transistor sensor with t_{HfO2} = 60 nm, which were detected from a set of incremental TNF-α concentrations (i.e, n = 0, 60 fM, 300 fM, 600 fM, 3 pM, and 6 pM) (b) The calibrated subthreshold-regime responses (S) measured from this sensor (labeled as red starts) with respect to TNF-α concentration (n). This *S-n* relationship calculated from this sensor with t_{HfO2}=60 nm is consistent with those measured from the sensors with t_{HfO2} = 30 nm. This result proves that the calibrated sensor response values do not strongly rely on the HfO_2 effective layer thickness.

Chapter 4

Multiplexed Nanoplasmonic Temporal Profiling of T-Cell Response under Immunomodulatory Agent Exposure

4.1 Introduction to the Study

T cells are major cell types in the recognition and effector mechanisms of the adaptive immune system.[103] A presence of antigenic stimulant triggers multiple cytokine-mediated intracellular signaling pathways that drive the proliferation, differentiation, and cytotoxicity activation of T cells. These T-cell responses are critical in regulating the protection of the body from pathogenic invasions and cancer development.[104, 105] However, undesirable pro-inflammatory or tissue-damaging cytotoxic responses of T cells can cause immune-related disorders, such as allergies,[106] autoimmune diseases,[107] transplant rejection,[108] and graft versus host disease (GVHD).[109] Certain immunosuppressive therapeutic agents "turn off" T-cell function by blocking cytokine-mediated pro-inflammatory intracellular signaling pathways by prohibiting cytokine gene expression of the cells.[110] However, excessive immunosuppression can be harmful, promoting opportunistic infections and immune

tolerance to cancer development.[111] It is highly challenging to precisely maintain a healthy immune reaction by immunosuppressive modulation therapy because of the highly dynamic nature of T-cell immune responses.

Profiling the cytokine secretion behaviors of T cells provides a means to accurately monitor the cellular functional states of the adaptive immune system. High-precision monitoring of the transient (and presumably subtle) variations of a cellular functional state requires continuous measurements of T-cell secretion profiles for multiple cytokine species. However, an attempt to achieve such cytokine secretion profiling using conventional processes, which involve cell culture, cell culture medium supernatant collection, and repeated sandwich immunoassays for analyte measurement, is time-consuming, wasteful, and expensive due to the need for a large amount of workload, samples, consumables, and assay agents. In previous study, Liu et al. [76, 112] demonstrated continuous cell-based cytokine secretion assays using label-free aptamer-based electrode biosensors integrated with microfluidic cell isolation structures. Their label-free biosensing approach is perhaps more accurate and convenient than conventional cell secretion assays by placing cells near the sensing area, which could minimize the time delay due to analyte diffusion in the measurement and eliminate the need for sample storage and transfer. However, it may still fall short of capturing subtle variations and whole information of cellular immune functions owing to its suboptimal limit of detection (1-10 ng/mL) and device design prohibiting simultaneous analysis of more than two analytes.

Our recent study[63] has demonstrated a multiplexed immunoassay that allows rapid, high-sensitivity, high-throughput, sample-sparing detection of several different

cytokines in human serum using nanoplasmonic biosensor microarrays. This assay involves localized-surface plasmon resonance (LSPR) imaging of biosensors integrated in a microfluidic platform as a key detection principle.[113],[114] The LSPR biosensor structure incorporates arrayed gold nanorod (AuNR) particle patterns conjugated with antibodies, in a confined microfluidic channel and provides the advantage of biosensor integration.[115] Measurements of LSPR image-intensity shifts resulting from analyte binding to the AuNR particle sensor surfaces allow for label-free, nanoplasmonic optical measurements of target biomolecules.[1] According to our previous study,[63] this immunoassay exhibits highly advantageous features, such as a short sampling-to-answer time (~ 30 min), which is the time required for the whole process involving analyate sample loading, incubation, and washing, a large dynamic range (~10 -10,000 pg/mL), a low operating sample volume (~ 1 μL), and multiplexed analysis capability.

Herein, we implemented our nanoplasmonic multiplexed immunoassay technique and quantitatively characterized dynamic functional response of antigen-stimulated Jurkat cells (human leukemic T-cell line) expose to an immunosuppressive agent. Our multivariate functional measurements of Jurkat cells revealed dynamic secretion signatures of the T-cell immune response as a result of immunosuppressive agent treatments. Similarly, the cellular functional monitoring capability demonstrated in this work could be extended to continuous secretion assay by means of sensor integration in a microfluidic system. This may facilitate the future development of a nanoplasmonic multiplexed assay-based diagnostic tool useful for personalized immune regulation treatment.

4.2 Methods and Materials

4.2.1 Microfluidic Channel Fabrication

Molds for constructing the PDMS microfluidic structures were fabricated on a silicon wafer using photolithography-based micromachining techniques followed by deep reactive ion-etching (Pegasus 4, SPTS Technologie Ltd, Allentown, PA, USA). The silicon molds were silanized with (tridecafluoro-1,1,2,2-tetrahydrooctyl)-1-trichlorosilane vapor (United Chemical Technologies) for 1 hr under vacuum to facilitate subsequent release of PDMS from the molds. A PDMS precursor (Sylgard-184, Dow Corning) was prepared by mixing a PDMS curing agent with the PDMS base (wt:wt=1:10), poured onto the silicon molds and cured overnight in a 60°C oven. Two separate fully cured PDMS structures with microfluidic channels were fabricated using different molds: one for patterning the arrayed AuNRs biosensor stripes on a glass substrate and the other for forming the analyte detection layer of the LSPR biosensor microarray chip.

4.2.2 LSPR Nanoplasmonic Biosensor Microarray Fabrication

A piranha-cleaned glass substrate was first oxygen-plasma treated at 20 W for 120 s. Then, a colloidal solution suspending positively charged CTAB-coated AuNRs (Nanoseedz, Hong Kong) were flown into PDMS microfluidic patterning channels covered by the plasma treated glass substrate. The surface of the glass substrate was negatively charged. The AuNRs were immobilized onto the glass substrate by means of electrostatic interactions and formed bar-shaped parallel sensor array patters. Subsequently, 1mM of 10-carboxy-1-decanethiol (C10) (Dojindo, Japan) was dissolved in 10% ethanol, loaded into the microfluidic patterning channels, and incubated overnight

to functionalize the AuNR surfaces with C10, which replaced CTAB through a ligand exchange process. 0.4 M EDC (1-ethyl-3-[3-dimethylaminopropyl] carbodiimide hydrochloride, Thermo Scientific) and 0.1 M NHS (N-hydroxysuccinimide, Thermo Scientific) were mixed at a 1:1 volume ratio in 0.1 M MES (1-ethyl-3-[3-dimethylaminopropyl] carbodiimide hydrochloride, Thermo Scientific) solution. 10 μL of the EDC/NHS/MES solution was loaded to the same microfluidic channels and incubated for 20 min to activate the ligand. This was followed by antibody coating of the AuNR sensor patters that involved loading of probe antibodies (anti-human IL-2, IFN-γ, TNF-α, IL-10, ebioscience, USA) in deionized water at a concentration of 50 μg/mL into individual patterning channels. Subsequently, 1% BSA in deionized water solution was loaded through the channels and incubated for 20 min for sensor surface passivation to eliminate nonspecific binding of biomolecules. At the end of every incubation step above, the sensor surfaces were thoroughly washed using deionized water, and any excessive solution and unbound molecules were removed.

4.2.3 Jurkat Cell Culture Reagents

Jurkat cells (CRL-2901, ATCC) were cultured in RPMI (RPMI-1640, ATCC) growth medium supplemented with 10% fetal bovine serum (30-2020, ATCC). Cells were incubated at 37°C with 5% CO_2 and 100% humidity in a CO_2 Cell Culture Incubator (Thermo Scientific). The culture medium was replaced every 2-3 days. The cells were collected by centrifugation at a speed of 1200g for 5 min and suspended in culture medium for the assays in this study.

4.2.4 Cell Secretion Assay Protocol

A cell culture medium of 2 mL suspending Jurkat cells at a concentration of $2.5x10^6$ cells/mL was loaded to one of the wells of a 6-well plate (Figure 4.1 a). A mixture of phorbol 12-myristate 13-acetate (PMA, Sigma-Aldrich) at 100ng/mL and Ionomycine (Sigma-Aldrich) at 1000ng/mL dissolved in deionized water was added into the prepared cells to activate them to secrete cytokines. Subsequently, these cells were incubated for 2 hours. A supernatant of 10μL was collected from the cell culture medium in the cell pool of the 6-well plate (Figure 4.1.a). This supernatant volume is less than 1% of the total cell culture medium volume, which allowed us to minimize the concentration changes resulting from collecting the supernatants. 6μL out of the 10μL supernatant collected was directly loaded into the LSPR biosensor microarray chip for cytokine quantification. After a 120-min incubation process, the immunosuppressant, tacrolimus (Sigma-Aldrich), was added into the cell pool at a concentration of 0, 0.1, 1, or 10ng/mL and incubated for 60 min. The supernatant sample was repeatedly collected from each cell pool every 60 min after the PMA/Ionomycin stimulation and every 10 min after the TAC administration. To fully expose the cells to the stimulant and TAC and to collect a sample from a uniformly mixed cell culture medium, the 6-well plate was manually shaken every time before collecting the supernatant. A syringe infusion pump was used to load the sample to the chip at an infusion rate of 2 μL/min for 3 min. Each sample loaded to the chip was incubated for 30 min and washed with PBS. The 30-min incubation time was determined from real-time binding measurements for the four different analyte types of various concentrations. We found that the analyte-binding event typically reached an equilibrium state within 30 min after the sample loading (Figure 4.2).

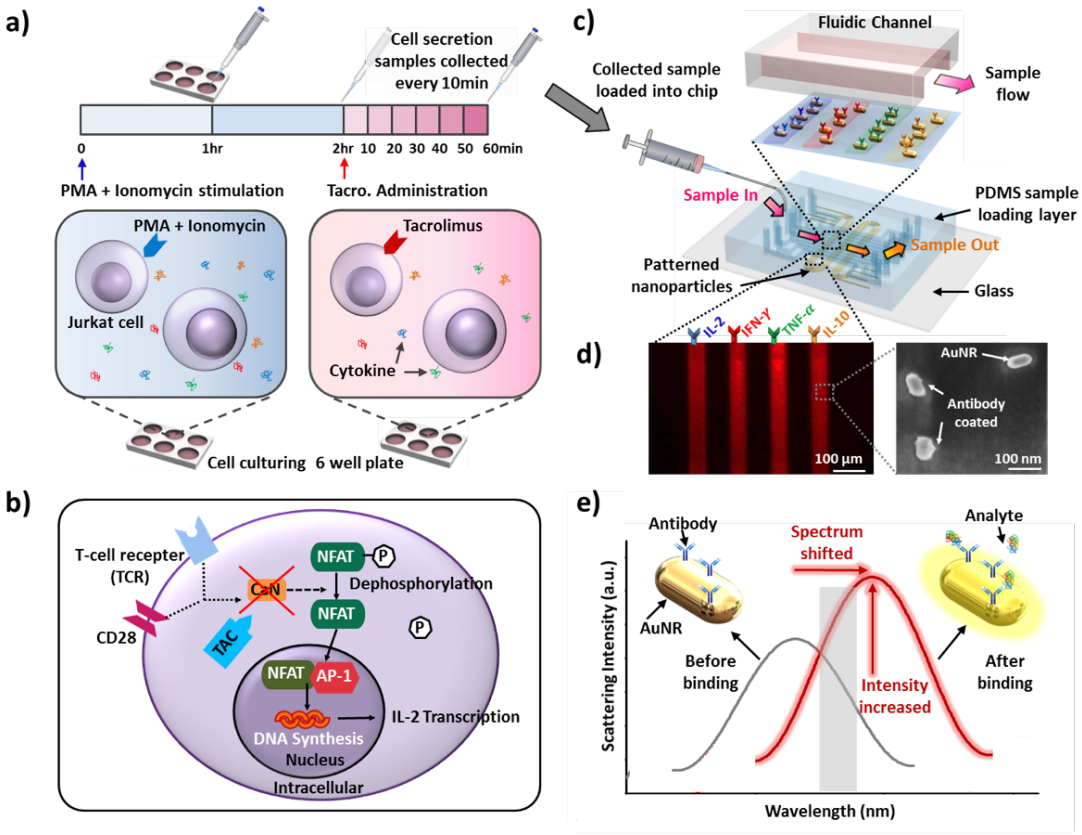

Figure 4.1: (a) Assay process involving Jurkat T-cell stimulation and tacrolimus administration. Prepared Jurkat T cells were activated by PMA and Ionomycine and incubated for 2 hrs in a 6-well plate. This was followed by TAC administration and incubated for one hour for cytokine secretion pathway alteration. During the first two-hour incubation period, cell-culture supernatant samples were collected every 60 min, and samples were collected every 10 min after dosing TAC to the cells. (b) T-cell intracellular cytokine secretion pathway and cellular-level effect of TAC. (c) Multiplexed cytokine detection using LSPR nanoplasmonic biosensor microarray chip. Collected samples were directly loaded into the chip through the top sample-loading PDMS channels. The bottom glass substrate, coated with patterned antibody-functionalized AuNR particles, was covered with sample loading channels. d) Dark-field image of four parallel AuNR array patterns and SEM image of individual AuNR biosensors immobilized on glass. Non-uniform nanoparticles surfaces show their antibody-coated surfaces. (e) Principle of LSPR dark-field intensity imaging of LSPR nanoplasmonic biosensor microarrays. The surface binding of a targeted antigen at the sensing surface causes the sensor image intensity to increase as a result of both the spectral redshift and intrinsic intensity enhancement of the AuNR scattering light. Measuring the intensity change enables us to quantify the amount of the analyte in the sample.

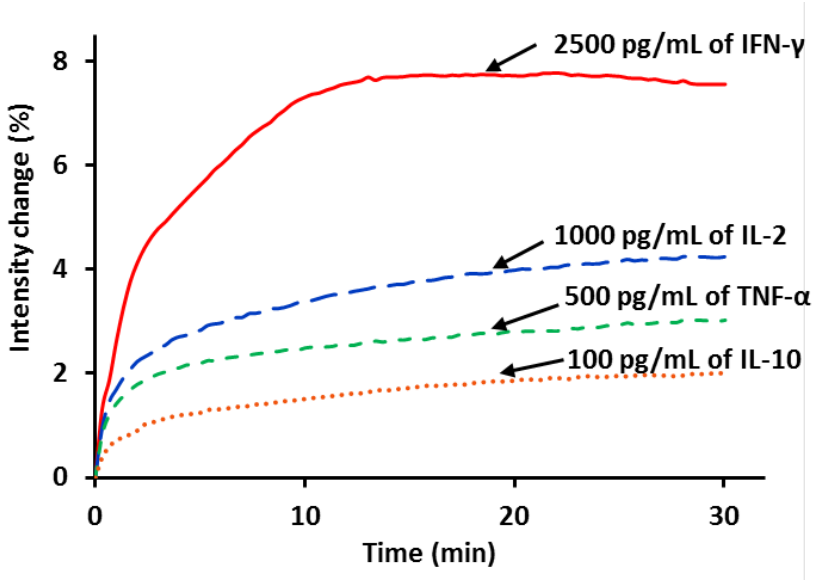

Figure 4.2: Real-time binding curves obtained from LSPR nanoplasmonic biosensor assay for four different cytokines (Red line – 2500 pg/mL of IFN-γ, Blue line – 1000 pg/mL of IL-2, Green line – 500 pg/mL of TNF-α, and orange line – 100 pg/mL of IL-10). A mixture of purified IL-2, INF-γ, TNF-α, and IL-10 at the different concentrations was loaded into the device and incubated for 30 min.

4.2.5 Cell Viability Test

Cells stimulated and incubated with TAC were collected and stained with 10% of trypan blue (302643, Sigma-Aldrich) v/v in PRMI solution and immediately examined under a microscope for cell viability test. It was observed under the transmission mode of the microscope that dead cells were stained with dye and colored blue while healthy cells remained uncolored.

4.2.6 LSPR Microarray Chip-to-chip Variance Characterization

Signal consistency was validated across different LSPR microarray chip devices. To this end, cytokine samples of known concentrations were loaded to two out of ten sample-detection microfluidic channels of each chip and measured their signal intensities. The coefficient of variance (CV, defined as the ratio of standard deviation to the mean

signal intensity value) of the signals was calculated to be 8.49 % across 15 chips after loading the background buffer PBS. This small chip-to-chip sensor performance variance (CV<10%) reveals the reproducibility and stability of our LSPR microarray assay, which minimizes errors that would result from using different chips for cell secretion measurements.

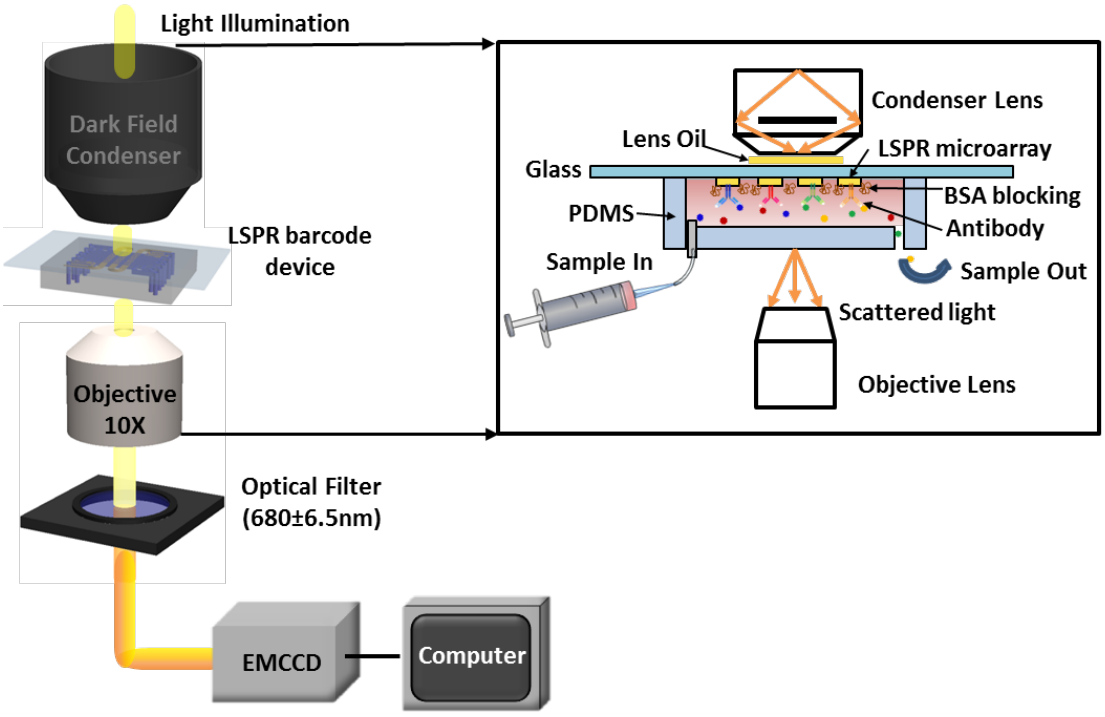

Figure 4.3: Schematic of the dark-field microscopy setup for LSPR biosensor microarray imaging. In the dark-field LSPR imaging process, light-source illumination from the top is first introduced to the dark-field condenser lens. The illumination light hits the sensor surfaces of the underneath chip with its central light beam blocked. This only allows the scattered light from the sensor image to be collected by the objective lens and subsequently filtered by the optical bandpass filter. In our study, the chip device was tightly mounted on a motorized stage and placed in the microscopy system for the entire measurement. The sample was both loaded to the device and washed using a syringe pump.

4.2.7 LSPR Dark-field Imaging Protocol

The fabricated and prepared LSPR biosensor microarray chip was mounted on a motorized stage (ProScan, Prior Scientific) to position the on-chip sensing spot at ease and to automate the signal scanning (Figure 4.3). A dark-field condenser (NA=1.45,

MBL12000, Nikon) was closely placed to the backside of the glass substrate (the opposite side of the AuNR-deposited sensor side) using lens oil. The light scattered from the AuNR nanoplasmonic biosensor arrays was collected using a 10x objective lens under the chip and then filtered by a band-pass filter (674-686nm, Semrock). This light signal was collected by an electron-multiplying CCD (EMCCD, Photometrics) camera and analyzed using NIS-Elecment BR analysis software. Further analysis was performed using our customized Matlab code.

4.3 Results and Discussion

4.3.1 Jurkat Cell Secretion Assay Sample Preparation

Jurkat cells, a commonly used human leukemia cell line for characterizing T-cell receptor signaling pathways[15], were assayed in a 6-well culture plate (Figure 4.1.a). Briefly, Jurkat cells were activated by treatments with phorbol 12-myristate 13-acetate (PMA) and Ionomycine (see Methods section) to induce T-cell receptor (TCR)-independent stimulation responses.[116] A supernatant of 10 μL from each culture well was collected every 60 min and then loaded into the nanoplasmonic microarray chip for multiplexed cytokine measurements during the 2-hr incubation period after adding PMA and Ionomycine.

After the 2-hr incubation period, four different concentrations (0, 0.1, 1, 10 ng/mL) of tacrolimus (TAC) were added into each cell culture pool (Figure 4.1.a). TAC is a potent immunosuppressive drug widely used to prevent T-cell induced allograft rejection.[117, 118] Figure 4.1.b illustrates the signaling mechanism of T cells and how TAC acts on the mechanism. When antigen-presenting cells co-interact with the TCR and

CD28-receptor of T cells, the co-stimulation triggers activation of calcineurin, which promotes dephosphorylation of NFAT and its translocation into the nucleus. In the nucleus, NFAT binds AP-1 proteins cooperatively to promote transcription of several cytokines.[119] The introduction of TAC to activated T cells inhibits the activation of calcineurin through interacting with FK506 binding proteins, which results in the suppressed cytokine secretion of the cells. Tracking the levels of cytokines secreted by T cells therefore provides a functional understanding of how TAC can effectively alter intracellular signaling events and the resulting T-cell functional response.

In this study, we designed experiments to monitor cellular functional changes of Jurkat cells previously stimulated with PMA and Ionomycine every 10 min after their exposure to TAC. A previous study by Khalaf et al.[120] showed that the secretion of cytokines from T cells significantly increases at 2 hrs after PMA and Ionomycine stimulation through heightened AP-1 activity. Based on this information we waited for 2 hrs after stimulation with PMA and Ionomycine to ensure that the Jurkat cells were fully activated before the dosing of TAC and the subsequent monitoring of the Jurkat cells' immune responses.

4.3.2 LSPR Nanoplasmonic Biosensor Microarray Chip

The LSPR nanoplasmonic biosensor microarray chip used in this study consists of two layers: a bottom glass layer and a top polydimethylsiloxane (PDMS) layer (Figure 4.1.c). The bottom glass layer contains four meandering strips of antibody-coated AuNRs, which were deposited by a one-step microfluidic patterning method.[63] The top PDMS layer has ten parallel microfluidic channels placed orthogonally with respect to

the AuNR strips on the bottom glass layer. This device design yielded 120 sensing spots in total on a single chip. Each individual channel could hold a sample volume of 350 nL (200 μm × 35 mm × 50 μm). Inlet and outlet wells of 0.75 mm in diameter were constructed in the top PDMS layer for sample loading and washing. Three identical segments of four collocating AuNR parallel strips in each microfluidic channel permitted three measurement repeats for each sample, which allowed us to obtain statistically meaningful readouts (Figure 4.4). We successfully functionalized each of the four AuNR strips with an anti-cytokine antibody targeting against interleukin-2 (IL-2), interferon-gamma (IFN-γ), tumor-necrosis-factor alpha (TNF-α), or interleukin-10 (IL-10), using the standard EDC/NHS chemistry (see details in Method section; Figure 4.1.d, left panel). It is known that T cells normally secret these four cytokines upon activation. We further utilized scanning electron microscopy (Figure 4.1.d, right panel) to verify that individual, antibody-conjugated AuNRs were uniformly distributed on the glass substrate with an inter-particle distance > 100 nm. This sufficiently long inter-particle distance was critical for avoiding plasmonic coupling between adjacent particles that could diminish analyte detection sensitivity.[63] Simultaneous detection of these four cytokines could provide predictive information and mechanistic insights for unraveling the complex and adaptive nature of T-cell immune response under stimulation and immunemodulation.[4, 121, 122]

The nanoplasmonic biosensor microarray chip was mounted on a dark-field imaging microscopy stage for signal detection. When target analytes bound to the antibody-functionalized AuNRs, the local refractive index change induced a redshift of the scattering spectrum of the nanoparticles, which was translated into an intensity increase of the sensor-pattern image (Figure 4.1.e). The whole AuNR biosensor

microarray image was then captured in real time using an electron multiplying charge coupled device (EMCCD) and analyzed by a customized Matlab code.

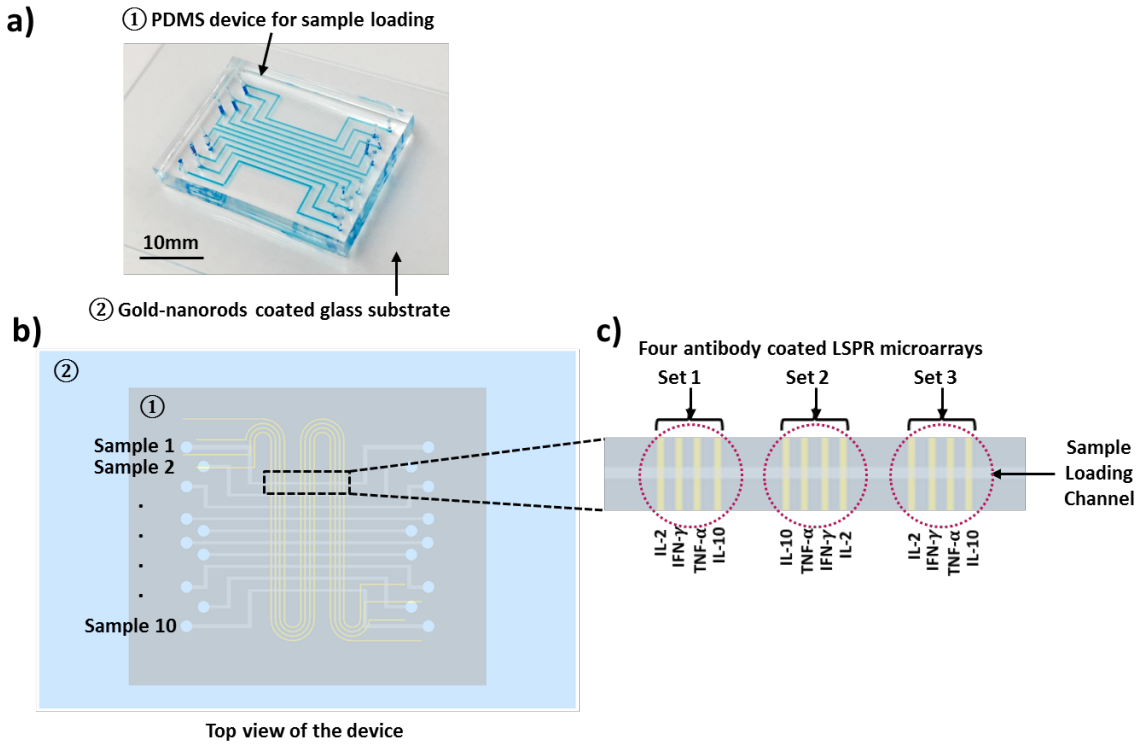

Figure 4.4. a) Photo image of LSPR nanoplasmonic biosensor microarray chip constructed with 120 sensing spots for cytokine detection. The device consists of a PDMS-based sample-loading/detection channel layer and a glass substrate with four meandering parallel sensor stripe patterns of gold nanorods (AuNRs). The surfaces of the AuNRs were conjugated with antibodies targeting four different types of cytokines (L-2, INF-γ, TNF-α, and IL-10). b) Top view of the device. Ten sample loading microfluidic channels were covered by the glass substrate with its AuNR sensor patterns orthogonal to the microfluidic channels. c) Magnified view of AuNR biosensor patterns, which have three repeats of four parallel arrays, each functionalized with antibodies targeting one of the four cytokines above. This arrangement allowed for triplicate measurements across the four cytokines with each sample, which minimized measurement error.

4.3.3 Cytokines Standard Curve Acquisition and Validation with ELISA

Prior to multiplexed analyte detection, we first performed parallel calibration for the LSPR biosensors on the microfluidic chip. Standard curves acquired for each cytokine allowed us to determine the dynamic range and limit of detection (LOD) of the sensors. To this end, we spiked a PBS solution with purified IL-2, IFN-γ, TNF-α, and IL-

10 of known concentrations (from 100 pg/mL to 2500 pg/mL) and quantified scattering intensity changes due to the target analyte binding to the AuNR biosensor microarrays. Here, the concentration range of our interest is smaller than the dynamic range of the biosensors reported in our previous study[12] Figure 4.5.a shows three sets of AuNR biosensor images with their intensities increasing with analyte concentrations. We recorded intensity values of LSPR sensing spots before (I_0) and after ($I_0 + \Delta I$) sample incubation and plotted standard curves showing the fractional intensity shift $\left(\frac{\Delta I}{I_0}\right)$ as a functions of cytokine concentrations (Figure 4.5.b). We further determined the limit of detection (LOD) for each cytokine, given by $\frac{3\sigma}{k_{slope}}$, where σ was the standard deviation of the background noise signal amplitude and k_{slope} was the regression slope of each calibration curve. The LOD for the four cytokines were 31.23 pg/mL, 26.08 pg/mL, 35.40 pg/mL, and 21.43 pg/mL for IL-2, IFN-γ, TNF-α, and IL-10, respectively.

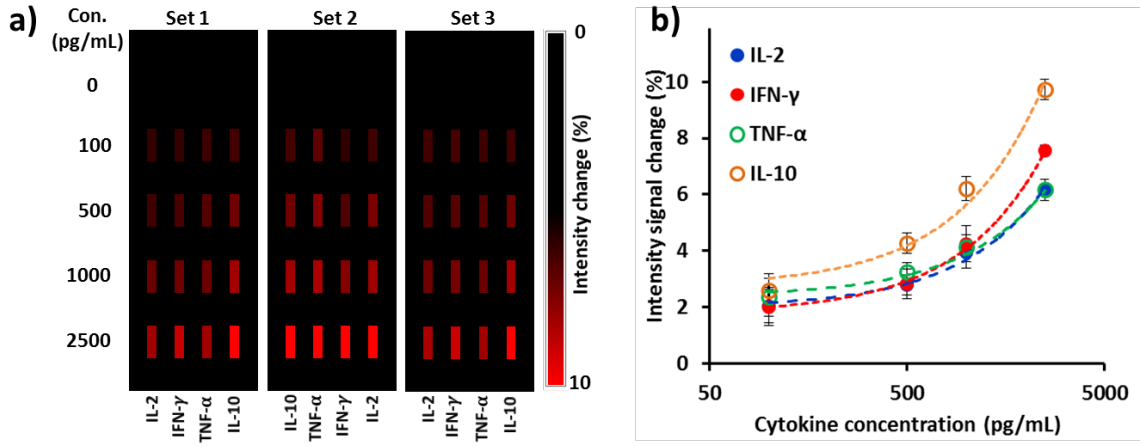

Figure 4.5: (a) Mapping of intensity variations at LSPR microarray sensing spots for four different types of cytokines at different concentrations. (b) Standard curves of purified IL-2, IFN-γ, TNF-α, and IL-10 obtained from LSPR nanoplasmonic biosensor microarray chip. These curves were obtained from the intensity images in (a). Our device allows for triplicate measurements for each sample analysis with three sets of four parallel LSPR sensor stripe patterns integrated within the same detection microfluidic channel, which minimizes measurement error.

We further compared readouts from the LSPR nanoplasmonic biosensor microarray chip with those of the "gold standard" ELISA (HumanCytoSet™, Invitrogen) (Figure 4.6). PBS solutions spiked with unknown concentrations of cytokines as well as cell culture supernatant samples containing cytokines secreted from T cells were prepared before being assayed using the LSPR nanoplasmonic biosensor assay and ELISA. An excellent correlation (R^2 = 0.931) between measurements from the LSPR nanoplasmonic biosensor assay and ELISA was obtained for samples across a wide dynamic range. Thus, the accuracy of the LSPR nanoplasmonic biosensor assay for cytokine secretion assays was validated with superior performance as compared to ELISA (Figure 4.6).

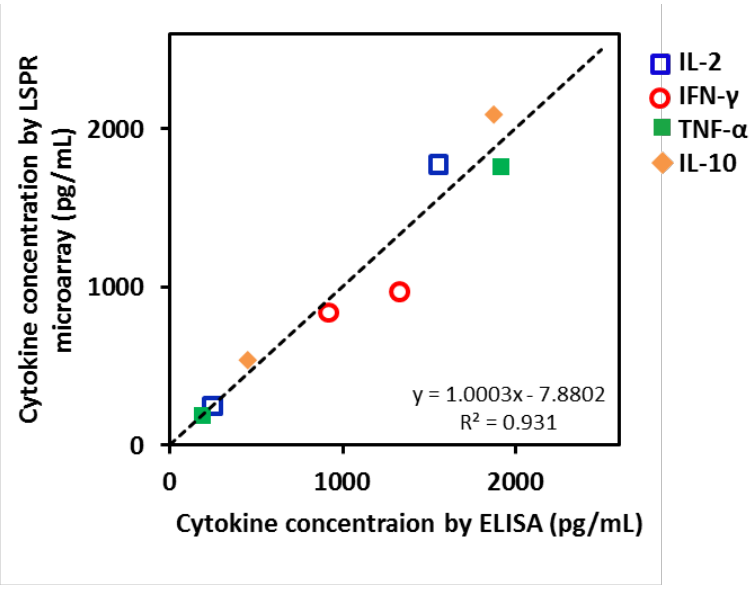

Figure 4.6: Correlation of LSPR biosensor assay data vs. ELISA data obtained from identical samples.

Furthermore, the LSPR nanoplasmonic biosensor assay provides several advantages over the conventional ELISA immunoassay (Table 4.1). First, the total assay time required for the LSPR measurement after the sample loading is 30 min, which is 8 times shorter than that of ELISA (4 hrs). The LSPR assay is label-free and able to

eliminate many process steps that involve tagging with secondary antibodies carrying labels and washing unbound agents. Second, the LSPR biosensor microarray chip only requires a small sample volume of ~1 μL for the measurement. This enables us to perform multi-time-point measurements through repeated sampling of small-volume cell-culture supernatants without significantly altering the analyte concentration in the original sample. Moreover, our LSPR biosensors have a large dynamic range (10-10000 pg/mL), which is suitable for multiplexed analysis of analytes coexisting in a single sample with large concentration variations.

The multiplexed LSPR nanoplasmonic biosensor assay requires less sample volume compare to ELISA. We calculated the volume required for the LSPR nanoplasmonic biosensor assay and ELISA. In LSPR nanoplasmonic biosensor assay, we obtained 12 data points with 10 μL of cell culture medium from triplicate measurements of the four target cytokines. To obtain the same amount of data with the standard singleplexed ELISA technique, the total volume of 50 $\mu L \times 12 = 600\ \mu L$ would be needed.

Additionally, Multiplexed LSPR nanoplasmonic biosensor is expected to be more cost effective than ELISA. Leng et al.[123] estimated the cost of commercial kit (R&D systems)-based ELISA measurement to be $16.53/analyte. Our LSPR assay costs $1.06/analyte in a multiplexed setting, where multiple analyte species are detected in parallel within the same chip device. This cost is estimated as follows:

Each LSPR biosensor microarray chip requires10 μL of gold-nanoparticles (stock price; 10 mL for $200), thus the AuNR material cost is $0.2/chip. The glass substrate costs $43.7/72 = $0.6/chip. We use 2$\mu L$ of each antiboby out of 1 mL stock solution ($229), which is diluted 10 times for agent loading with ease. The total cost for the four

antibodies is \$229×4 × $\frac{2}{1000}$ =\$ 1.832/chip. We estimate the labor charge for the entire 2-hour process, which includes device preparation, sample loading, sample detection, and data collection, to be \$20/hr × 2 hour =\$40/chip. Thus, the total cost of our LSPR biosensor assay involving 8 different samples, each having 4 target analytes, is only \$1.06/chip for analysis of each analyte.

	LSPR Microarray	ELISA
Assay Time	30 min	4 hour
Sample Volume	Minimum $1\mu L$	Minimum $50\mu L$
Dynamic Range	10-10000 pg/mL	10-1000 pg/mL
Multiplex	Four or more	Single
Cost per assay	\$1.06/sample	\$16.53/sample

Table 4.1 Comparison of LSPR biosensor assay and ELISA.

4.3.4 Dynamic Cytokine Secretion Profile Measurement

Some researchers have studied the dynamics of T-cell cytokine secretion[124] or demonstrated highly multiplexed single-cell cytokine secretion measurement[125] aiming to understand the T-cell functional response. Access to a technique allowing multiplexed measurements of dynamic cytokine secretions is critically important for fully assessing antigen-specific T-cell functional response.[104] Given the intrinsic complexity of the cytokine network, T-cell functional response assessed by a single detection parameter is unlikely to reflect the whole picture of cytokine-mediated cellular functions.[17] In addition, cytokine production from antigen-specific T-cell response can be highly

transient [17] and dynamic[126]. The standard method of gauging immunosuppression relies only on serially measured drug levels in serum with no functional assessment of T-cell responses. Therefore, knowledge from multiplexed time-course measurements of cytokine secretion should be extremely valuable.

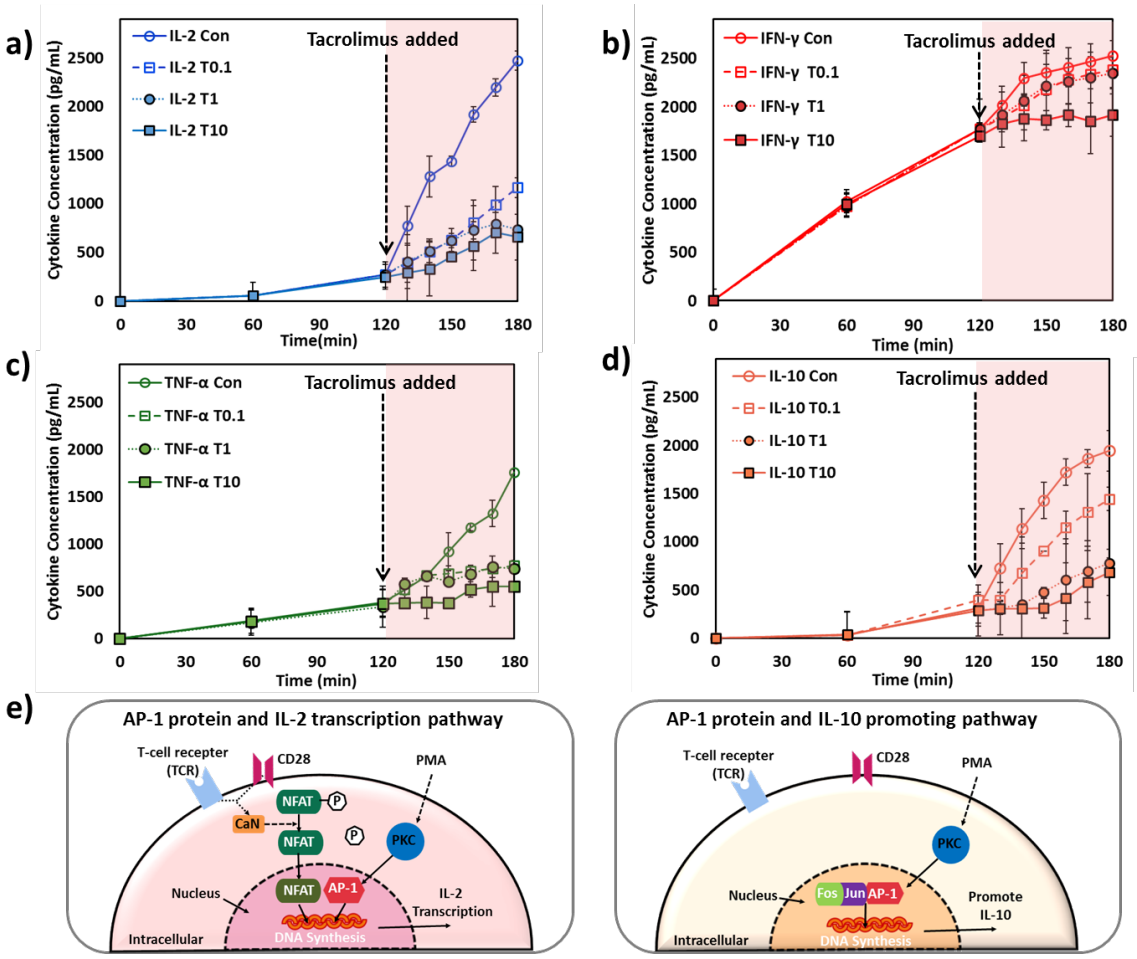

Figure 4.7: Temporal cytokine secretion profiles of Jurkat T cells for (a) IL-2, (b) IFN-γ, (c) TNF-α, and (d) IL-10 during two serial incubation periods: (1) two hours after PMA and Ionomycin stimulation and (2) one hour after TAC administration. The label of "Con" represents data from TAC-free control measurement in the second incubation period with the PMA/Inomycin stimulated cells. The labels of "T0.1," "T1," and "T10" represent data from the second incubation period after dosing TAC at the concentrations of 0.1, 1, and 10 ng/mL, respectively. The schematics in (e) and (d) show AP-1-mediated T-cell secretion pathways of IL-2 and IL-10, respectively.

To obtain temporal T-cell cytokine secretion profile, we collected a series of small-volume supernatant samples from Jurkat cell culture medium at different time points and sequentially loaded each of them into a separate microchannel of the LSPR nanoplasmonic biosensor microarray chip. Secretion curves for IL-2, IFN-γ, TNF-α, and IL-10 clearly demonstrated activated and immune suppressed states of Jurkat cells that were sensitive to different concentrations of TAC (Figure 4.7.a-d). Variations across the secretion profiles of the four target cytokines likely reflected their different functional roles and secretion mechanisms mediated by different intracellular signaling pathways as discussed below. The high temporal resolution of the LSPR nanoplasmonic biosensor microarray chip for cytokine secretion measurements allowed us to capture transient states of immune suppressed T cells that occurred within the first 10 min after TAC administration.

It is well known that T cells activated by antigen stimulation secrete cytokines, such as IL-2 and IFN-γ, via an NFAT-mediated regulatory pathway (Figure 4.1.b).[119, 127] The presence of TAC blocks NFAT dephosphorylation due to intracellular calcineurin inhibition, which hinders the transcription and secretion of NFAT-dependent cytokines by T cells.[128] Our results show that IL-2 and IFN-γ secretions from Jurkat cells were suppressed under the high TAC-dose levels (Figure 4.7. a, b). Moreover, IL-2 concentration reached a plateau around 50 min after TAC administration at concentrations of 1 and 10 ng/mL (Figure 4.7.a). The plateau of cytokine secretion profile indicates complete IL-2 secretion inhibition for Jurkat cells.

Activated Jurkat cells with no TAC dosing (Figure 4.7. a, control) showed a sharp elevation of IL-2 secretion at 2 hrs after PMA and Ionomysin stimulation. This abrupt

secretion elevation likely could be attributed to the onset of AP-1 protein activation accompanying NFAT in the T-cell nucleus, forming stable DNA binding sites to initiate transcriptional processes for cytokine secretion (Figure 4.7.e).[119] Previous research has revealed that AP-1 activation in T cells upon exposure to PMA is a delayed process that arises around 2 hrs after stimulation.[21,][129] AP-1 activation leads to an elevated inflammatory response with heightened cellular secretion of pro-inflammatory cytokines, including IL-2, IL-6, CXCL8, TNF-α, as well as the anti-inflammatory cytokine, IL-10.[120] This is consistent with our control data for IL-2, TNF-α, and IL-10. Furthermore, there are research reports suggesting that AP-1 activity does not affect IFN-γ expression, which is again similar to our observation of no leap of IFN-γ secretion from Jurkat cells.[130]

TAC also inhibits the transcription of NF- κB in the T-cell nucleus and regulates secretion of pro-inflammatory cytokines.[118] TNF-α, is a NF- κ B dependent cytokine[118, 129] and a good indicator of the inflammation suppression effect of TAC on the immune system. Figure 4.7.c shows that TNF-α secretion under the doses of TAC (T0.1, T1, T10) exhibited different profiles than the control. There were notable deviations in TNF-α secretion from control at 20 min after dosing 0.1 and 1 ng/mL of TAC, whereas TNF-α secretion suppression already started within 10 min of treatment with the 10 ng/mL TAC.

IL-10 is known to counter-regulate and inhibit T-cell activation and proliferation by suppressing the expression of pro-inflammatory cytokines, such as IL-2, IL-5 and IFN-γ.[131-133] Interestingly, after its immediate secretion shutdown upon TAC treatments, IL-10 secretion gradually recovered after 10, 20, and 30 min exposure with

TAC doses of 0.1, 1, and 10 ng/mL, respectively. This unique secretion pattern of IL-10 might be attributed to a feedback reaction of IL-10 production to pro-inflammatory cytokines that were already secreted by Jurkat cells.[120, 134] The presence of pro-inflammatory cytokines in the cell culture at significant concentrations likely continued to promote production of IL-10 even after the TAC-induced secretion suppression took place.

We further verified that cell death was not responsible for deceased levels of cytokine secretions. To this end, we performed viability tests on Jurkat cells treated with stimulants and TAC (Figure 4.8 and Table 4.2). Across all four conditions (Con, TAC 0.1, 1, 10 ng/mL), only 3.05 – 4.25% of Jurkat cells lost viability, suggesting a negligible effect of cell death on our assays.

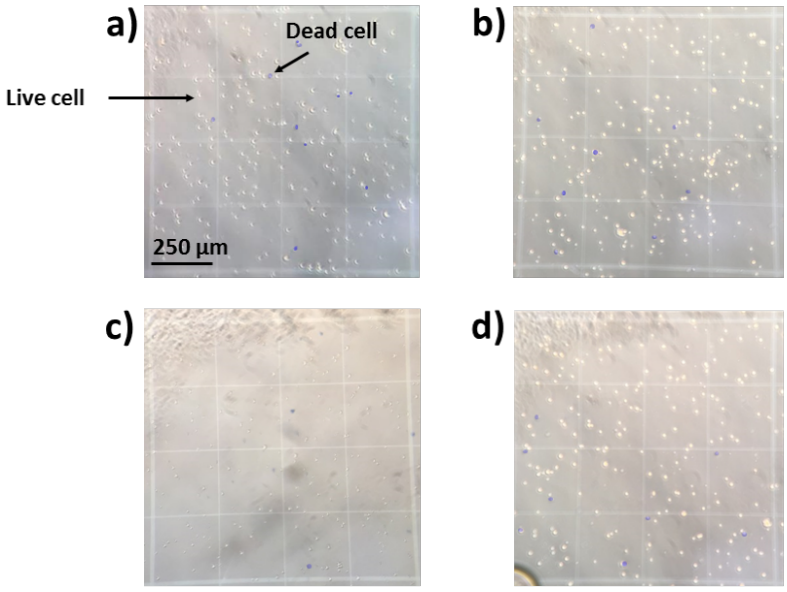

Figure 4.8: Cell viability test using trypan blue solution. The images were taken using a hemocytometer after adding the trypan blue solution to the Jurkat T-cells after all the assay experiments under the conditions in a)-d).

	Condition	Total cell #	Dead cell #	Viability (%)
a)	Control	235	10	95.75
b)	TAC 0.1 ng/mL	234	8	96.59
c)	TAC 1 ng/mL	235	8	96.6
d)	TAC 10 ng/mL	229	7	96.95

Table 4.2: Cell viability test result using trypan blue solution. The Jurkat T-cells after all the assay experiments under the conditions shown in Figure 4.8. a)-d). All cases resulted in cell viability over 95%, which indicates that the cytokine secretion suppression was not primarily due to cell death.

4.3.5 Transient Variations of Cytokine Secretion Rate

We extracted the cytokine secretion rate (pg/min) from the slope of the line connecting the two subsequent data points in each 10-min interval of the secretion curves in Figure 3 and plotted secretion rate variations over time for all the four target cytokines (Figure 4.9). The temporal variation of the cytokine secretion rate provides information useful for understanding the interplay between proinflammatory cytokines and T-cell functional response after TAC administration. As expected, the transient evolutions of the rapidly changing cytokine-release behavior of the Jurkat T cells exhibit both drug dose- and time-dependent characteristics.

The data show an immediate reduction of the IL-2 secretion rate after the peak value at 10 and 30 min after dosing TAC of 1 and 10 ng/mL, respectively (Figure 4.9.a). In contrast, the 0.1 ng/mL dose did not completely cease the IL-2 cytokine secretion throughout the 60-min observation period, as indicated by the monotonically increasing secretion-rate curve. A similar reduction of the secretion rate was observed for IFN-γ as well upon TAC administration. The values of the IFN-γ secretion rate converged to a

small value near the end of the assay regardless of the TAC concentrations (Figure 4.9.b), which were derived from the near-end plateaus of all the original IFN-γ secretion-profile curves (Figure 4.7.b). The TNF-α secretion rate experienced gradual variations over 60 min for the three different TAC-dose levels. The rate eventually reached a near-zero value for all the TAC-dose levels while the control experiment resulted in a nearly monotonically increasing curve. The TAC dose of 10ng/mL was especially inhibitive and immediately ceased the TNF-α secretion, and the secretion rate became nearly zero within the first 10 min. Such information may have important implications for the dose effect of TAC on various immune functions.

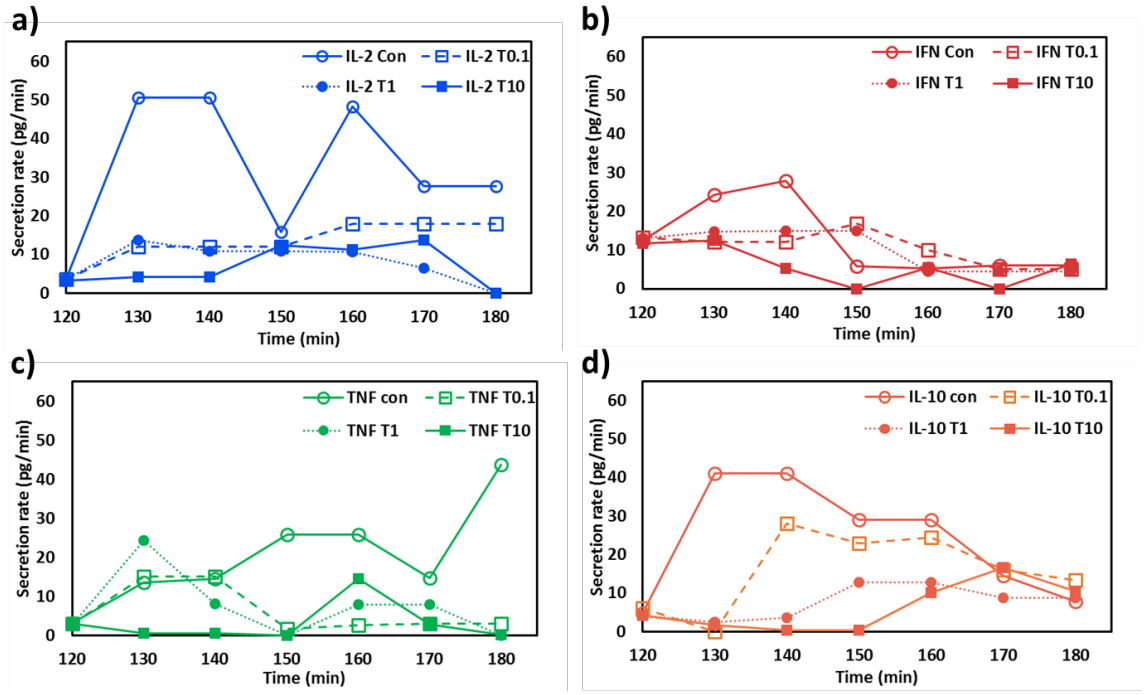

Figure 4.9: Time-course cytokine secret rate variations of Jurkat T cells for (a) IL-2, (b) IFN-γ, (c) TNF-α, and (d) IL-10 during the one-hour incubation period after TAC administration. At the time point at t = 120 min is the point at which the TAC administration takes place. The labels of "Con," "T0.1," "T1," and "T10" represent the same conditions as in Fig. 4.7.

The data for IL-10 show an intriguing secretion characteristic with a distinct re-heightened secretion rate during the 60-min period (Figure 4.9.d). The initially depressed secretion rate of IL-10 might be a result of the combined contributions from both the drug exposure and the lowered pro-inflammatory cytokine expression in that time frame. The subsequent increase in the IL-10 secretion rate likely reflects a delayed anti-inflammatory feedback response of the cells to the peaked secretion of IL-2 and IFN-γ found in the early stage of the post-TAC administration period. Such IL-10 secretion dynamics could be explained by the IL-10-mediated autocrine regulation of T-cell functions.[135]

To summarize, we demonstrated the use of LSPR nanoplasmonic biosensor microarrays for obtaining temporal cytokine secretion profiles of Jurkat cells under immunosuppressive modulation. The multiplexed time-course cytokine secretion data obtained from this work enabled us to characterize dynamic features of the functional response of Jurkat cells after their exposure to an immunosuppressant, tacrolimus. The T-cell functional response is governed by an orchestration of dynamic secretions of multiple cytokine species. Thus, the multi-analyte (IL-2, IFN-γ, TNF-α, and IL-10), multi-time-point detection provided a unique opportunity to obtain a broad picture of cellular functional states rapidly modulated by immunosuppressive agents. Variations in the degree and timing of the TAC-induced secretion suppression across these cytokines under a given drug administration condition offer important and clinically relevant insight to more precisely modulate immune responses beyond the historically standard practice of monitoring serum drug levels.

Chapter 5

Integrated Nanoplasmonic Sensing for Cellular Functional Immunoanalysis using Human Blood

5.1 Introduction to the Study

Localized surface plasmon resonance (LSPR) is a plasmonic phenomenon that arises around nanoscale structures or nanoparticles of noble metal when light is illuminated onto a nanoscale featured sensing surface. When the incident light frequency matches the natural frequency of electron oscillation of the conductive metal nanoparticles, the interactions between the incident light and the nanostructured surface modify the energy of the internal vibronic states of the particles and trigger the LSPR. As a result of the high sensitivity of the plasmon resonance to changes in the local refractive index, LSPR detection techniques have been implemented into various label-free quantitative analyses of antigen-antibody interactions, analyte surface density, and protein surface binding kinetics [69, 136, 137]. Moreover, the resonance wavelength and intensity can be readily modified by the temporal or irreversible absorption of analyte as small as protein, nuclei acids and cytokine [138]. As a result, LSPR-based biosensing has

attracted much attention from researchers in biomedical sciences and offers great potential in clinical diagnosis.

Cytokines, immunomodulating protein biomarkers secreted from immune cells, are indicators of the functional status of the human immune system. They play critical roles in regulating cell signaling, cell differentiation, and inflammatory response in the immune system.[139, 140] For example, the cytokine secretion from immune cells in response to pathogenic invasions is an indicator of infection that shows a time-course change of the diseased condition of human host.[141] However, such immune reactions are often extremely dynamic and occur quickly. Thus, rapid immunoassay that affords comprehensive characterization and quantitative analysis of cytokines secreted from immune cells is the key for precisely determining the subtle variations and the dynamic characteristics of cellular immune functions in the host.[142, 143]

Conventional enzyme-linked immunosorbent assay (ELISA) is a widely used method for quantification of cytokines. Benefiting from its cost-effective mass use, simple parallel array-type operation, and relatively high sensitivity, ELISA has become the most common tool for clinical diagnosis of pathogenic attacks on patients. However, the need for secondary antibodies binding to the target analytes results in a long sample preparation time and high complexity in sample labeling. Moreover, the fluorescent-based detection scheme requires a large amount of sample volume to achieve a sufficient signal-to-noise ratio for detection. Recent advances in the label-free surface plasmon resonance (SPR) detection technique overcome the aforementioned shortcomings of ELISA by eliminating the tedious labeling process. However, the SPR detection technique still requires bulky instruments based on the Kretschmann arrangement

incorporating a prism coated with a thin metal layer and free space optics, while yielding a longer surface plasmon decay length δ_d than the LSPR technique. These features make the bedside application of the SPR technique challenging. Specifically, the need for bulky optical components in the SPR technique hinders the detection platform to be miniaturized and integrated with other systems such as point-of-care microfluidic devices. While the longer surface plasmon decay length δ_d yields a higher sensitivity to a bulk refractive index change, it is less responsive to changes closer to the surface as compared to LSPR, which is essential for detecting antigen-antibody binding that occurs near the sensing surface [144]. The LSPR technique takes the advantage of simple and cost-effective optics, which is highly desirable for microfluidic integration. More important, the LSPR technique yields precise and quick responses to the local refractive index changes resulting from the surface adsorption of target molecules. As such, it has been proven to be an effective *label-free* detection method for antibody-antigen binding as compared to the aforementioned biosensing techniques [145-148].

The detection limit of the LSPR technique for molecular sensing is on the order of a few pM. It should be noted that however, both the detection limit and the sensitivity of the LSPR technique are highly dependent on the sensing platform and the size of the target molecule [149, 150]. In particular, cytokines are small molecules with a molecular weight < 30 kDa. The small size of cytokines greatly hinders the LSPR-based detection in clinical applications and disseminations. There have already been several approaches based on sandwich-type immunoassays with secondary antibodies or secondary particles to improve the detection limit of LSPR technique for natural biomolecules [147, 151]. However, these approaches lose the original advantage of label-free LSPR biosensing

that enables rapid, dynamic biomolecular detection. To the best of our knowledge, quantitative analysis of immune cell-secreted cytokine molecules from human blood has never been demonstrated with a LSPR platform. The implementation of LSPR biosensing for human blood samples faces more challenges due to the presence of other complex blood components in addition to the immune cells and the analytes under study.

In this study, we developed a LSPR-based optofluidic immunoassay technique that could precisely determine the concentrations of small cytokine molecules secreted from immune cells in human blood with an ultra-small sample volume and a much shortened assay time. Specifically, we successfully demonstrated a LSPR sensing platform device that could seamlessly allow isolating and trapping target immune cells from human lysed blood, cell incubation and stimulation, and detecting cell-secreted cytokines such as TNF-α on a single chip. Our technique employed an approach of spatially confining analytes within a small microfluidic chamber with a volume of a few μL. This approach effectively increased the concentration of cytokines secreted from the trapped immune cells to a detectable range while compensating the limitations of the conventional LSPR technique for small-molecule detection. The enrichment of cytokines in such a small chamber volume further facilitated the analyte-antibody interactions and reduced the time required for achieving the equilibrium binding state [152]. As a result, the microfluidic LSPR immunoassay platform reported here achieved quantitative detection of cytokine secretion from a desired subset of immune cells down to a cell population as few as 1,000 cells, which drastically reduced the sample volume by approximately 100 times and shortened the total assay time by 3 times as compared to the conventional cytokine secretion assays.

5.2 Materials and Methods

5.2.1 Microfluidic Device Fabrication

The integrated optofluidic LSPR device consists of three different layers. The middle layer for cell separation and incubation chamber was fabricated using micromachined technique by photolithography and followed a deep reactive ion-etching (DRIE) (Deep Silicon Etcher, Surface Technology Systems, Allenton, PA). The silicon mold was silanized with (tridecafluoro-1,1,2,2,-tetrahydrooctyl)-1-trichlorosilane vapor, United Chemical Technologies) for 1 hour in vacuum to facilitate subsequent release of PDMS structures from the mold. The PDMS prepolymer (Sylgard-184, Dow Corning) was prepared by thoroughly mixing the PDMS curing agent with the PDMS base monomer (wt : wt = 1 : 10) and poured onto the silicon mold and cured overnight at 60°C oven.[153] Fully cured PDMS structure was peeled off and treated with O_2 plasma for PDMS-PDMS bonding with prepared supporting PDMS layer. The supporting PDMS layer is a 5 mm thick layer with no special features, except those for supporting fluidic interconnects for the device inlet/outlet and for sustaining the water cap between the light probe and the PDMS channel.

5.2.2 LSPR Sensor Chip Preparation

The LSPR signal detection sensor chip, ZEONORTM 8 spot array-SAM surface, was purchased from Lamdagen (Menlo Park, CA). The LSPR sensor surface was activated with 20 μL of mixed 0.4M EDC (1-ethyl-3-[3-dimethylaminopropyl]carbodiimide hydrochloride, Thermo Scientific) and 0.1M NHS (N-hydroxysuccinimide, Thermo Scientific) at a 1:1 volume ratio in 0.1M MES(1-ethyl-

3-[3-dimethylaminopropyl]carbodiimide hydrochloride, Thermo Scientific) solution for 20 mins. After the surface activation, the primary TNF-α antibody (DY210, R&D Systems) was diluted to 100 $\mu g/mL^{-1}$ in 1x PBS and 20μL, injected to the detection surface, and incubated for 60 min. To eliminate the non-specific binding on the detection surface, 20 μL of 1% BSA (Albumin, from bovine serum, SIGMA) in 1x PBS and 1x casein (5x Casein block solution, Surmodics BioFX) blocking buffer were flown into the detection chamber and incubated for 20 min. During all the process, the solutions were loaded using a syringe pump (LEGATO210, Kd Scientific)) at 5 $\mu L\ min^{-1}$. And between every step, the detection surface was thoroughly washed to remove any excessive solutions or molecules using 40μL of 1x PBS at 5$\mu L\ min^{-1}$

5.2.3 THP-1 Cell Culture and Reagents

THP-1 cells (TIB-202, ATCC) were cultured in RPMI (RPMI-1640, ATCC) growth medium supplemented with 0.05mM 2-Mercaptoethanol (21985-023, Life technologies) and 10% Fetal Bovine Serum (30-2020, ATCC). Cells were cultured at 37°C with 5% CO_2 and 100% humidity, and the cell culture medium was replaced every 2-3 days. The cells were collected by centrifugation at a speed of 1200g and resuspended in RPMI for subsequent experiments.

5.2.4 Cell Quantification and Viability in the Device

The prepared THP-1 cells were stained by 1μM Calcein AM (C3100MP, Invitrogen) and incubated for 30min before fluorescence microscopy imaging for cell quantification and viability test. A 130W mercury lamp (Intensilight C-HGFIE, Nikon)

was used for fluorescent illumination. Calcein AM was visualized with a FITC filter set (excitation; 498 nm, emission; 530 nm, Nikon). We employed two methods to quantify the cell population loaded in the device. First, we calculated the total number of cells introduced to the inlet by multiplying the original cell concentration with the total volume injected into the device. Hence, the population of isolated cells by the micro-pillars was estimated by subtracting the number of cells collected at the outlet. We also quantify the cell population by measuring the fluorescent intensity of the stained cells, which is proportional to the concentration of the fluorophore labeling the cells. We made control chambers, each with the same area and volume as the incubation chamber of the device, and loaded Calcein AM-stained cells with their population varied. We obtained the standard curve showing the fluorescent intensity at each chamber as a function of the cell population. The fluorescent intensity integrated over the whole image of the cells in the chamber was then fit back to the standard curve to quantify the population of the cells loaded in the device.

5.2.5 Blood Sample Preparation and CD45 Cell Captured with Polystyrene micro-beads

One milliliter of whole blood sample was incubated with 10 mL of RBC Lysis Buffer (00-4333-57, eBioscience) at a 1:10 volume ratio for 12-15 min. After the lysis, 20-30 mL of 1x PBS was added into the mixture and centrifuged at 400 g for 10 min. We aspirated all the plasma and red blood cells and resuspended the remained cells into RPMI medium. To prepare the polystyrene beads, 100 μL of biotinelated polystyrene beads (CP01N, Bangs Laboratory, Inc.) were washed with 1 mL of D.I. water for three

times and centrifuged at 1200 g for 15 min in between. After the thorough washing, the beads were resuspended into 2 mL of washing buffer (0.1M PBS (10X PBS), pH 7.4) and gently mixed with 80 μL of CD45 antibody (MHCD4515, Life technologies) for 30 min at room temperature. After the incubation, the CD45 conjugated beads were washed three times as described above and made ready for the use of capturing CD45 surface marker cells.

5.2.6 LSPR Detection Setup and the Spectrum Data Analysis

The LSPR sensor chip was illuminated by the light source (HL-2000 tungsten halogen light, Ocean optics) which generates a continuous spectra of light from 400~700 nm. The incident light propagating along the illumination fiber embedded at the center of the light probe (R400-7-UV-VIS, Ocean optics) was introduced perpendicular to the sensing surface. The reflected light signal from the detection surface was collected by the detection fibers of the light probe, which connected with a spectrometer (HR-4000, Ocean optics) (Figure 5.1). The absorbance spectrum of the detection surface was obtained using commercial signal processing software (Spectra Suits, Ocean Optics) that subtracts the measured intensity of the reflected light from the originally known intensity of the incident light at each wavelength over the spectral band of 400 to 700 nm. All the collected data were analyzed by a MATLAB code to obtain the regression curve and find the peak wavelength from the absorbance spectrum curve. [154]

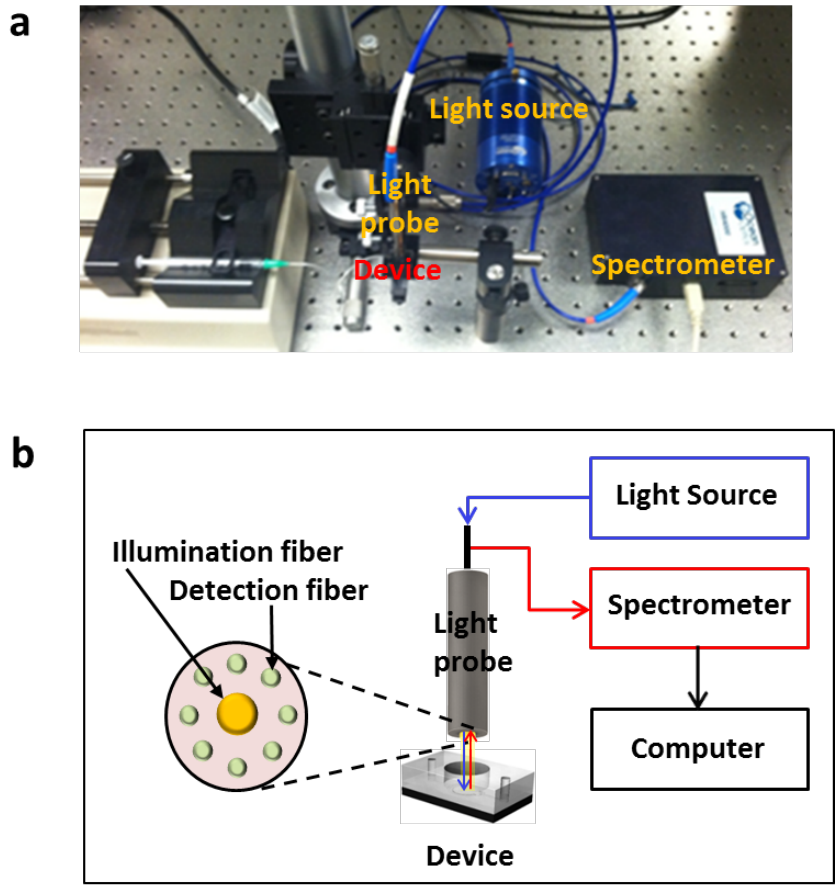

Figure 5.1: LSPR detection setup (a: real optics setup image and b: schematic optics setup) used for obtaining the absorbance spectrum of the LSPR detection surface of the optofluidic platform. The setup includes a light source, a light probe, a spectrometer, and a signal-processing computer. The light probe has a core illumination fiber connected to the light source and a bundle of embedded optical fibers. The light source provides a full spectrum of light that excites the gold nanostructured LSPR detection surface. The bundled optical fibers collect the light reflected from the detection surface. The collected reflected light signal transfers into the spectrometer and by pass through the grating, mirror and CCD detector, the light spectrum is converted into electrical signal for analyzing.

5.3 Results and Discussion

5.3.1 LSPR Detection and Device Design

As briefly mentioned above, LSPR arises when the frequency of the collective oscillation of electrons near the surface of a conductive metal nanoparticle matches the excitation light frequency. At the resonance wavelength, the light field induces a dipolar

response of the conducting electrons as shown in Figure 5.2.a. Binding of a biomolecule onto the surface of a noble metal (in this study, the metal is gold) nanoparticle causes a change in the near-field refractive index around the nanoparticle. As a result, the absorbance of light changes, and this change results in a shift of the absorbance spectrum peak (Figure 5.2.a). Such a LSPR spectrum wavelength peak shift can be described using the equation 5.1 [155].

$$\Delta\lambda_{max} = m\Delta n[1 - \exp(^{-2d}/_{l_d})] \qquad (5.1)$$

Here m is the bulk refractive-index response of the nanoparticles, Δn is the change in refractive index induced by the absorbate, d is the effective thickness of the adsorbed layer, and l_d is the characteristic electromagnetic field decay length.[155] The refractive index of the depositing monolayer of biomolecules is approximately 1.45, [156] which is higher than the refractive index of water medium. Thus, if there occurs a biomolecule binding event on the nanoparticle surface, Δn and d will increase, resulting in a red shift of the resonance peak wavelength.

Our optofluidic device was composed of two polydimethylsiloxane (PDMS) layers serving as a supporting layer and a microfluidic layer, respectively, and one LSPR sensing layer with a circular detection pattern of gold nanoparticles deposited at its center, which is shown as the yellow spot on the black bottom layer in Figure 5.2.b and the AFM image. The gold nanoparticle detection surface was illuminated under a full spectrum of 400-700 nm light from the core of the light probe placed above the device. The reflected light from the sensing surface was collected by a bundle of optical detection fiber in the light probe (Fig. 5.2.b, Fig. 5.1). The gold nanoparticles deposited on the sensing surface were functioned with 10-Carboxy-1-decanethiol (C10) and activated

following the general 1-Ethyl-3-(3-dimethylaminopropyl)carbodiimide (EDC) activation protocol [154]. The activated carboxylic group on the gold nanoparticles could then form esters with the amine groups on the primal antibody (Figure 5.2.c).

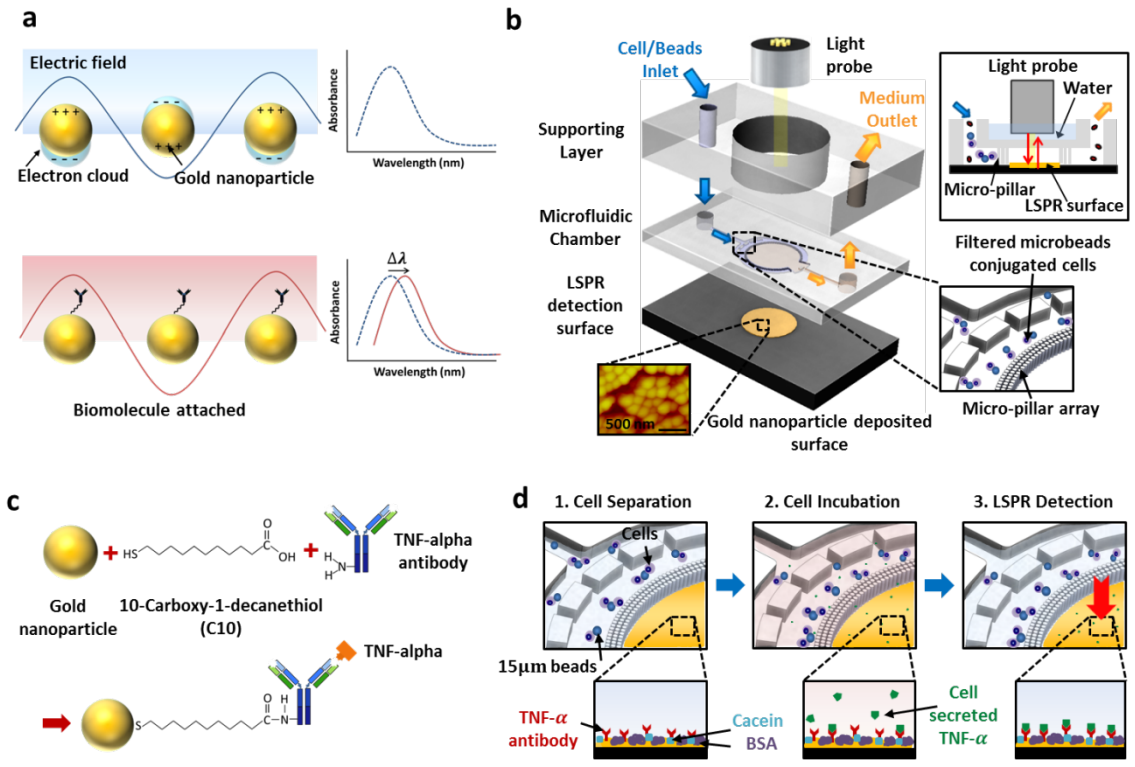

Figure 5.2: (a) Principle of nanoplasmoic biosensing based on LSPR at gold nanoparticle surfaces. (b) Schematic of integrated LSPR optofluidic platform device. The bottom layer is a gold nanoparticle-deposited (or gold nanostructured) surface for LSPR detection. The magnified image (lower left) is an AFM image of the gold nanostructured LSPR detection surface. The middle layer includes a microfluidic chamber and channels. The chamber has integrated micro-pillar arrays (shown in the middle right schematic) to trap bead-bound target cells. The top layer provides structural support for light probe alignment and for cell/reagent injection and ejection. The cross-sectional schematic (upper right) shows the arrangement of the device and the light probe consisting of an illumination core and a bundle of detection optical fibers. (c) The gold nanostructured detection surface is functionalized with a chemical ligand (C10). The C10 ligand has a carboxylic group that binds with the amine group of the probe antibody molecule. (d) Concept of multi-functional LSPR optofluidic operation. Each illustration shows the soft lithographically patterned polydimethylsiloxane (PDMS) microstructures on the flipped side of the middle layer and the sensing surface of the bottom layer.

The microfluidic chamber layer, mainly providing the function of trapping and incubating cells, was shown in the middle in Figure 5.2.b. A unique circular structure

composed of three arrays of micropillars with the pillar diameter of 30 μm diameter and the pillar edge-to-edge gap distance of 5 μm was incorporated around the sensing surface to isolate and enrich the target immune cells before the cells were stimulated and incubated for cytokine secretion and detection (Figure 5.2.c, micro-pillar array). The diameter of the center region of the microfluidic chamber was set to be 3.2 mm, with a height of 50 μm. This chamber was connected to the inlet and outlet (0.75 mm in diameter) by channels of 200 μm and 50 μm in width and height, respectively. The total channel volume was calculated to be approximately 3 μL. Such a small chamber size enabled rapid accumulation and diffusion of cell-secreted cytokines, and therefore acutely reducing the volume and incubation time required for the target analyte binding to the LSPR sensing surface. The top supporting PDMS layer provided structural support for injecting the sample with a syringe pump and sustaining a water cap filling the gap between the light probe and the detection surface (Figure 5.2.b panel in the up right). The water cap served to minimize the refractive index mismatch at the interfaces, to increase the signal-to-noise ratio by suppressing background noise arising from thermal gradients and air fluctuations [157], and to prevent direct contact between the probe and the sensing surface.

Figure 5.2.d illustrates the processes of the label-free LSPR optofluidic cellular functional immunoanalysis technique developed for human blood samples. Our technique integrated cell isolation and enrichment, cell stimulation and incubation, and detection of cytokines secreted from isolated immune cells on a single chip. The general assay steps using the device are described as follows: The target cells were first attached to 15 μm-diameter polystyrene beads conjugated with antibodies specifically binding to the cells'

surface marker proteins. The bead-bound cells were then introduced into the device from the inlet, trapped by the micro-pillar arrays owing to the mechanical rigidity of the beads, and incubated in the microfluidic chamber. After stimulated by endotoxin solution for 2 hours, the cells produced cytokines (e.g. TNF-α), which readily diffused into the detection surface through the gaps between the micro-pillars and captured by the primary antibodies covalently immobilized on the nanostructured gold surface (Figure 5.2.d). Binding of the cytokines on the nanostructured gold surface altered the LSPR absorbance spectrum of the detection spot. We measured the spectrum peak shift using a custom-built LSPR detection setup shown in Figure 5.1. The illumination fiber in the light probe was connected to the broad-spectrum light source and used to excite the detection surface to induce the LSPR effect. The reflected light was then collected by the detection fibers also embedded in the light probe, and the light signal was collected by the spectrometer and converted to electrical signals for further analysis.

5.3.2 On-chip Cell Trapping Performance

On-chip cell trapping with our LSPR device was demonstrated first for a human acute monocytic leukemia cell line (THP-1) and then for CD45+ immune cells isolated directly from lysed human blood as shown in Figure 5.3. THP-1 cells are commonly used as a model for mimicking the function and regulation of monocytes and macrophages and for immunocytochemical analysis of protein-protein interaction. CD45+ immune cells represent a group of immune cells that express CD45 surface marker, a type I transmembrane protein assisting in T-cell activation. The polystyrene microbeads were initially conjugated with antibodies that specifically interact with cell surface biomarkers:

CD14 for THP-1 cells and CD45 for CD45+ immune cells in lysed blood sample, respectively. The prepared microbeads were diluted to a concentration of 1.4×10^6 mL^{-1} in PBS and then mixed with THP-1 cells at a 1:1 ratio in the cell culture medium (RPMI) for one hour to form immune cell-bead conjugated pairs. This process was repeated for CD45+ cells after a whole blood sample was red blood cell (RBC)-lysed as shown in Figure 5.3.a (also see Materials and Methods). The fluorescence microscopy image in the top panel of Figure 5.3.b verifies that the immune cell-bead conjugation scheme worked in lysed blood. Here, the image shows that bead-bound CD45+ cells, freestanding immune cells, which could be either other immune cell subpopulations or unbound CD45+ cells, and residual RBCs were co-existing in the lysed blood sample.

We subsequently loaded the lysed blood sample into the device using a syringe infusion pump at a constant flow rate of 5 $\mu L\, min^{-1}$. The unbound cells and other components in the original blood escaped through the pillars and washed out through outlet (middle panel in Figure 5.3.b, 5.4) while the cells attached to the microbeads were efficiently captured by the micro-pillar arrays (the bottom panel in Figure 5.3.b). Here, the microbeads exhibited the capability of both isolating the target immune cells from the blood and ensuring high-fidelity cell trapping with the micro-pillar arrays. Mammalian cells are typically soft and elastic due to the lack of the rigid cellular wall possessed by plant cells. As a result, they can be easily deformed under external pressure and squeezed to escape through the gap between the micro-pillar arrays. In contrast, the microbeads behave as solid carriers and prevent the undesired escape of the target cells attached to them. As proved by the fluorescent intensity measurement of the cell population in the device (Figure 5.3.c, 5.4.b), the microbead attachment of cells enabled the trapping rate

to reach nearly 95% while unbound cells were trapped only at a rate of around 50% (Figure 5.3.d). The image in Figure 5.3.b shows that the cell-to-bead conjugation ratio is not necessarily 1:1 for all the pairs. However, this does not affect the accuracy of our method to quantify the trapping rate (see Materials and Methods).

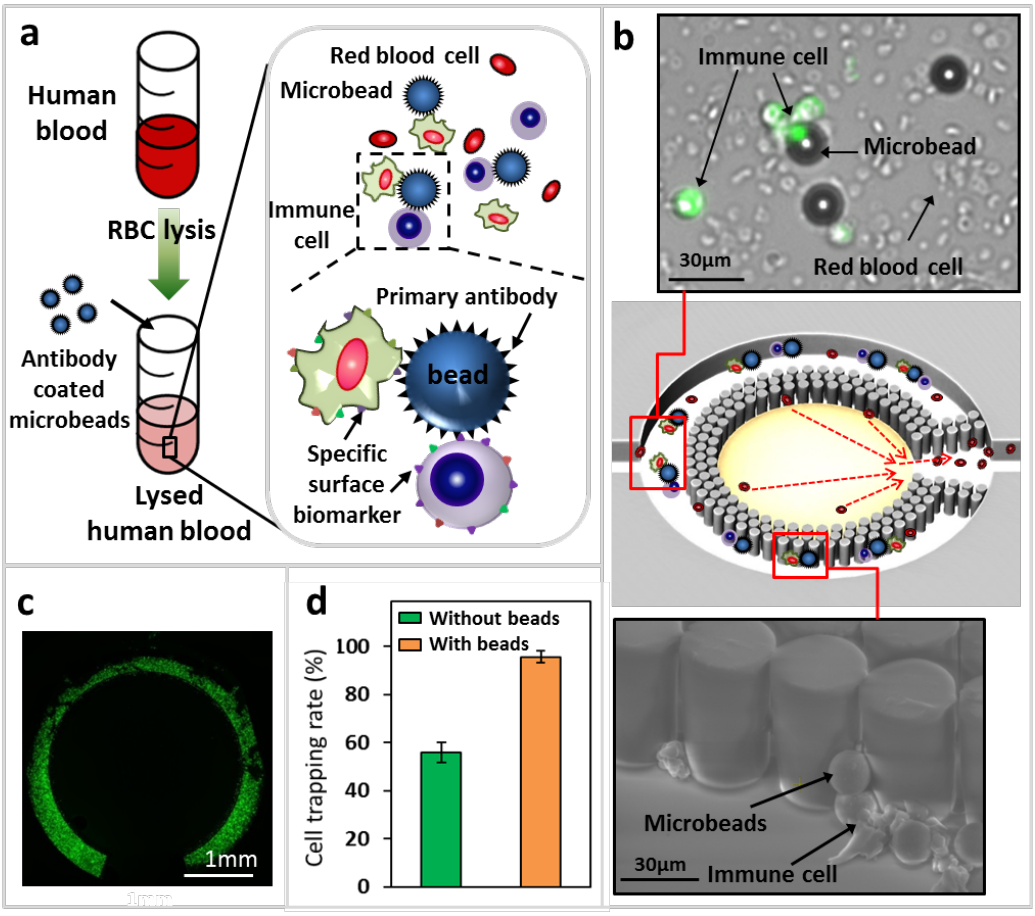

Figure 5.3: (a) Process of conjugating target immune cells with primary antibody-coated microbeads for their subsequent extraction from lysed human blood. Here, the human whole blood was first red blood cell (RBC)-lysed with the buffer to remove some fraction of the entire RBCs. The primary antibody-coated microbeads were then mixed with the lysed blood. Cells expressing a particular surface marker protein species were specifically bound to the microbeads. This process formed cell-bead conjugate pairs. (b) Process of isolating and trapping target white blood cells using micro-pillar arrays. The lysed blood sample containing the cell-bead conjugate pairs and residual RBCs was loaded into the device. The upper optical microscopy image shows bead-bound cells in the lysed blood sample. The lower scanning electron microscopy (SEM) image shows cell-carrying microbeads trapped by the micro-pillar arrays. (c) Fluorescence image showing the whole microfluidic chamber structure with trapped calceinAM-stained THP-1 cells. (d) Cell trapping rates for freestanding THP-1 cells and bead-bound cells. The cell-bead

conjugation scheme increased the trapping rate up to 95% from 50-60%, which was achieved without the conjugation process.

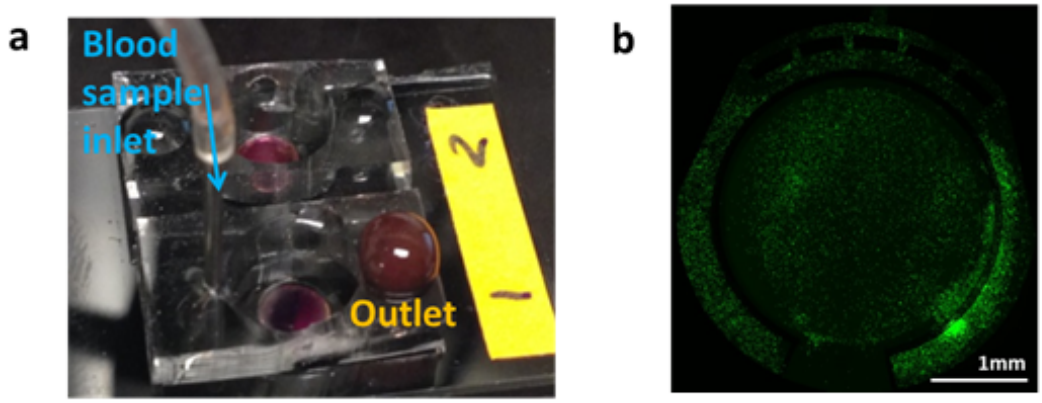

Figure 5.4: (a) Photo image of the real LSPR optofluidic device with lysed blood loaded from the inlet. Unfiltered blood cells and other blood contents are ejected from the outlet. The cells trapped in the device were bounded to the microbeads, and stimulated and incubated for on-chip immunofunctional assay. (b) Fluorescence image of freestanding calceinAM-stained cells loaded to the device without microbead conjugation. Approximately, the half of the loaded cells were squeezed out, escaped through the micro-pillar arrays, and moved out to the detection surface region of the device.

5.3.3 Dynamic Detection of Biomolecular Surface Binding

We selected purified natural TNF-α as the analyte cytokine species in our assay and characterized the device's performance for dynamic analysis of biomolecular surface binding events. The gold nanostructured detection surface of the device was first functionalized with anti-human TNF-α, which served as the capture antibody of the surface. The remaining uncovered detection surface was coated with blocking buffer containing 1% BSA and casein molecules to prevent non-specific adsorption of TNF-α molecules. The TNF-α solution was then introduced to the device and incubated for 1 hour to allow the analytes fully engage with the primary antibodies. For each step described above, we thoroughly washed the LSPR detection surface with PBS solution to stabilize it against solvent annealing and avoid non-specific binding of the introduced

molecules to it. The LSPR peak wavelength throughout the entire process was continuously monitored (Figure 5.5). Exposure of the activated carboxy-terminal conjugated gold nanostructured surface to the anti-human TNF-α induced a red shift of 2.5-3.0 nm as a result of covalent ester group formation. Addition of the blocking buffer resulted in a weaker red shift (1nm) mainly due to the smaller sizes of the BSA (MW. ~66.5 k Da.) and casein (MW. ~28-32 kDa.) than that of the antibody (MW. ~150 kDa.).

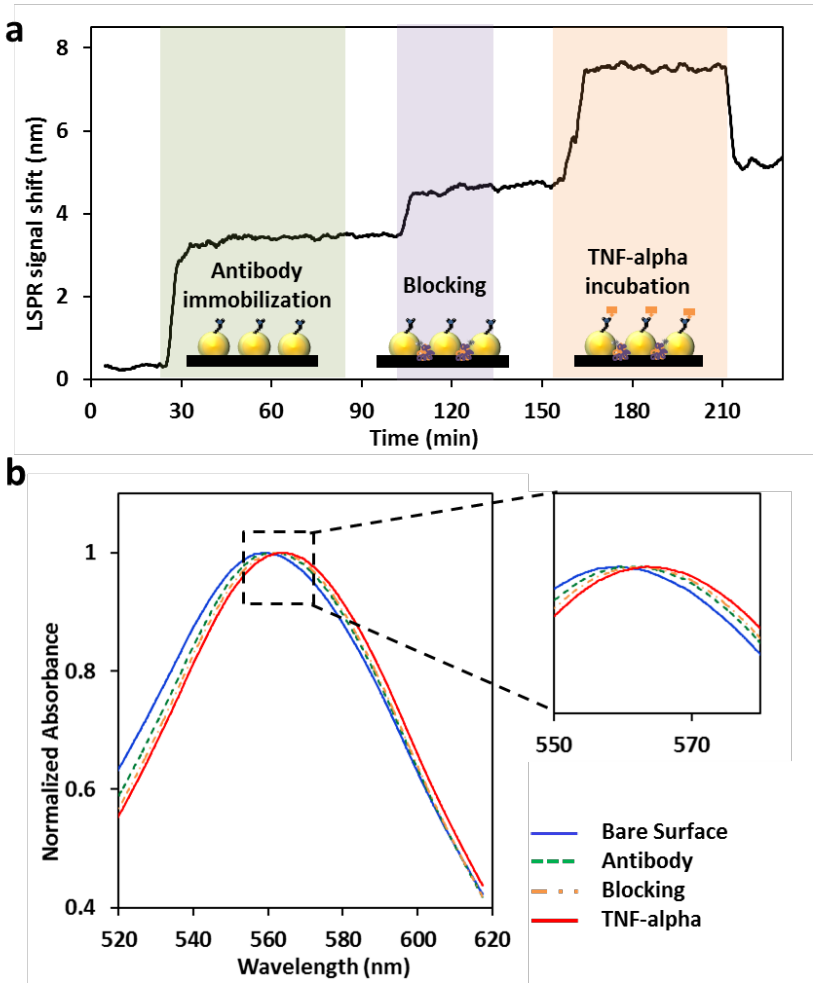

Figure 5.5: (a) Real-time LSPR signal shift during LSPR biosensor surface preparation and analyte detection processes. The green region shows the time-course absorbance spectrum peak shift of the LSPR detection surface during the primary antibody immobilization process with an incubation time of 60min. The purple region shows the LSPR peak shift during the surface blocking process by BSA and cacein molecules. The orange region shows the LSPR peak shift during the process of loading purified TNF-α to the detection surface with an incubation time of 60min. At the end of each process, the entire detection surface was washed with PBS buffer to

eliminate the non-specific binding of reagent and analyte molecules. (b) Normalized LSPR absorbance spectra corresponding to the processes in (a).

Introducing 5.85 nM of TNF-α yielded a further red shift because of the specific interactions between TNF-α and the antibody. The subsequent blue shift was possibly due to the removal of physically adsorbed TNF-α during rinsing. We further examined the selectivity of our sensing surface towards TNF-α by introducing unpaired analyte, elafin, and a mixture of elafin and TNF-α analyte into the device (Fig. 5.5.a, 5.6). The LSPR peak wavelength red shifted only when TNF-α molecules were present in the solution (Figure 5.5.a orange region, Figure 5.6.a blue region), while no shift was observed with the other type of analyte, elafin, introduced (Figure 5.6.b purple region) to the detection surface. The total time required for the LSPR detection surface preparation prior to the assay was 2.5 hours, which is much less than that of the conventional ELISA methods, which typically take an overnight process for detection surface preparation (Figure 5.5.a).

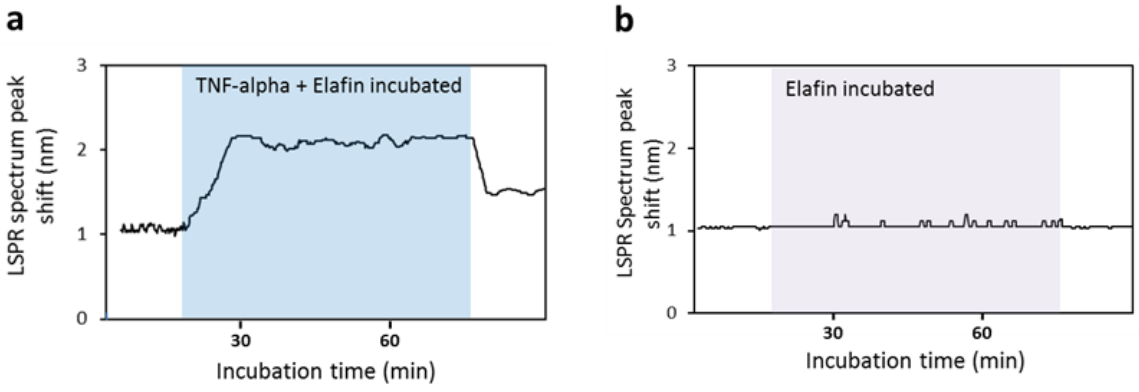

Figure 5.6: (a) Real-time LSPR spectrum peak shift upon loading a mixture of 250ng/mL of TNF-α and 250ng/mL of elafin to the detection surface of the device. The detection surface was prepared with Anti-human TNF-α serving as the probe antibody, followed by a blocking process with 1% BSA and cacein. The blue region represents a 1h-incubation process of the mixture sample. The effective spectrum peak red-shifted by ~0.3 nm after washing the detection surface. (b) Real-time LSPR spectrum peak shift upon loading 250ng/mL of purified elafin to the same detection surface as in a. The purple region represents a 1h-incubation process of the elafin sample. Loading only elafin cytokines resulted in unnoticeable LSPR spectrum peak shifts.

5.3.4 TNF-α Standard Curve and Validation with ELISA

Prior to our LSPR cellular functional assays using real blood samples, we first obtained the analyte standard curve using purified TNF-α (DY210, R&D systems) solution of known concentrations ranging from 100 – 500 ng/mL. With the increasing concentration of TNF-α, the LSPR peak wavelength shifted linearly from 0.1076 nm to 0.6779 nm (Figure 5.7.a). This TNF- α standard curve provided the correlation between the analyte concentration and the LSPR spectrum peak shift. Additionally, we compared our LSPR immunoassay results together with those obtained from the conventional ELISA method (DY210, R&D systems) using a commercial plate reader (Synergy H1, BioTek) for three unknown concentrations of natural TNF-α samples (Figure 5.7.b). Each spectrum shift obtained from the LSPR detection was converted to a TNF-α concentration value using the standard curve in Figure 5.7.a. Similarly, the conversion of the ELISA signal was performed using a calibration curve collected during the experiment. Figure 5.7.b showed an excellent linear correlation (R^2=0.9937) between the results from the LSPR immunoassay and the ELISA analysis for the TNF-α samples.

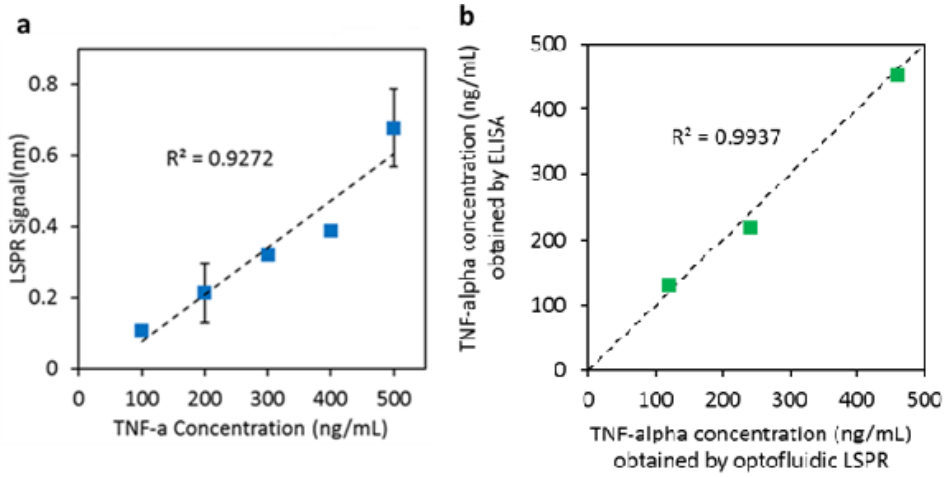

Figure 5.7: a) Purified TNF-alpha standard curve. b) TNF-α concentration obtained by the conventional ELISA technique versus TNF-α concentration detected using the integrated LSPR

optofluidic platform for the same TNF-α sample of three unknown concentrations. A high correlation (R^2 = 0.99378) was obtained between the data from the two different methods, which validates the performance of our device for LSPR biosensing.

5.3.5 Integrated Optofluidic LSPR Cellular Functional Analysis

After cross-validation of the biosensing performance of the LSPR platform with the ELISA technique, THP-1 cells suspended in buffer solution were loaded into the LSPR device for on-chip cell separation, incubation, stimulation, and detection of cell-secreted TNF-α. Figure 5.8.a,b show results obtained from LSPR signal shifts due to binding of TNF-α secreted by LPS-stimulated cells with their population and the LPS concentration varied. The amount of TNF-α increased monotonically with the LPS concentration and the population of THP-1 cells incubated in the device. Incubation and stimulation of 20,000 THP-1 cells at a LPS concentration ranging from 5 to 25 ng/mL resulted in LSPR spectrum shifts of 0.1901, 0.3445, and 0.7004 nm, each corresponding to TNF-α secretion at a concentration of 163.36, 296.13, and 602.05 ng/mL, respectively. At a LPS concentration of 25 ng/mL, the LSPR signal shifted by 0.1761 nm (151.37 ng/mL), 0.3085 nm (265.14 ng/mL), 0.4412 nm (379.20 ng/mL), and 0.7235 nm (621.93 ng/mL) with 1,000, 5,000, 10,000, and 20,000 THP-1 cells, respectively. (values inside the parentheses corresponded to concentrations of TNF-α obtained from the standard curve.) Under the same incubation and stimulation conditions, our optofluidic platform device allowed us to observe the TNF-α secretion from cells as few as 1,000, which is a 100 times less than that required in the conventional cellular immunophenotyping assay. The minimum cell population for detection, which is determined by measuring the LSPR spectrum shift equivalent to 3 times the standard deviation of the background noise from

a blank device (without loaded cells), was about 533 cells. Typically, there exist on average 7,000 leucocytes in 1 μL of human blood. It follows that our LSPR optofluidic platform yields a detection limit that permits the assay with a human blood volume as small as 100 pL.

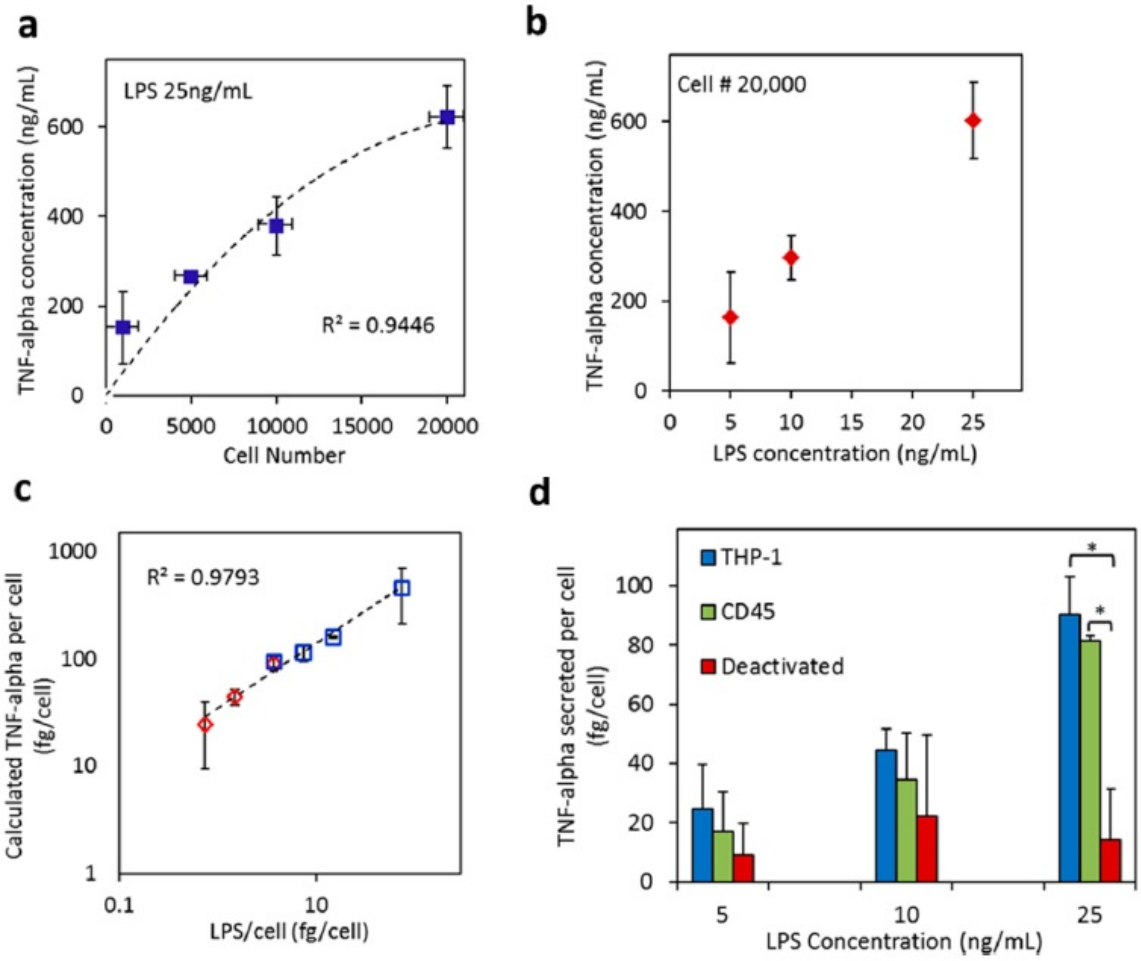

Figure5.8: (a) TNF-α concentration versus population of trapped cells upon LPS stimulation at 25ng/mL. The minimum detectable cell population achieved by the LSPR optofluidic platform device is estimated to be 533 cells from curve extrapolation and background noise measurement. (b) TNF-α concentration versus LPS concentration upon stimulating cells of a fixed population of 20,000. (c) Quantity of TNF-α molecules secreted per cell versus quantity of LPS molecules available for stimulation per cell. (d) Quantity of TNF-α molecules secretion per cell for normal THP-1 cells, CD45 cells, and LPS-deactivated cells loaded to and stimulated in the device at varying LPS concentration. The p-values calculated using the paired Student's t-test indicate significant differences ($P<0.05$ (*)) in the TNF- α -secretion behaviors of the functional and deactivated cells. All the plots were obtained from LSPR spectrum peak shifts of the detection surface of the optofluidic platform device.

It should be noted that a strong correlation (R^2=0.9793) was found between TNF-α secretion per cell and available LPS molecules per cell as shown in Figure 5.8.c. A similar trend was also observed in our previous study that TNF-α secreted from each THP-1 cell was proportional to the number of LPS molecules available for each cell.[158]

We further prepared cell cohorts consisting of normal THP-1, immunologically deactivated THP-1, and CD45+ cells isolated from human blood, and measured the level of TNF-α secretion for these cohorts when stimulated at a given LPS concentration between 5 and 25 ng/mL. Previous research [159] reveals that immunologically "deactivated" peripheral blood monocytes may be functionally connected to immunoparalysis, which is associated with adverse outcomes of the severe reaction of a host to infection, such as sepsis. When a patient is in the state of immunoparalysis, the immune cells in the host body secrete an attenuated amount of cytokines. To examine whether our integrated LSPR platform could differentiate the normal and deactivated conditions, we deactivated THP-1 cells by treating them with 10 ng/mL of LPS in the RPMI medium overnight before LSPR biosensing assays. The cells were washed with cell growth media before loaded into the device to remove the remaining LPS. This pretreatment of THP-1 cells with LPS increases the cells' endotoxin tolerance during the second LPS stimulation so that the cells become less sensitive to the stimulation.[160] As such, these deactivated THP-1 cells mimic the conditions resulting from the state of immunoparalysis. As shown in Figure 5.8.d, after normal or deactivated THP-1 cells, both at a fixed population of 20,000, were introduced into the device and stimulated with varying LPS concentrations for 2 hours, TNF-α molecules secreted by the deactivated cells was 2 - 6 times less than those from the normal THP-1 cells. Thus, our integrated

LSPR optofluidic platform enabled quantitative differentiation of the two distinct THP-1 cell cohorts.

5.3.6 LSPR Optofluidic Human Blood Assay

CD45+ cells used in our immunofunctional assay were peripheral blood mononucleated cells (PBMCs) isolated from lysed human blood samples by using CD45 antibody-coated microbeads. These cells are a mixture of immune cells consisting of lymphocytes, monocytes, and macrophages. When exposed to LPS, not all of these cells would respond to the stimulation. It follows that TNF-α secretion levels from THP-1 cells and CD45+ cells will be different under the same LPS stimulation with the same cell number. As can be seen from Figure 5.8.d, the level of TNF-α secreted from THP-1 cells was 1.1 - 1.4 times higher than that from CD45 cells isolated from human blood samples. Moreover, TNF-α secretion levels from CD45+ cells obtained from a healthy donor was significantly higher than that from deactivated THP-1 cells mimicking the immunoparalysis state. Our results in Figure 5.8.d demonstrate the promise of our LSPR optofluidic platform for future rapid monitoring and prognostic determination of infectious diseases based on on-chip human blood cellular immunofunctional analysis.

Chapter 6

Conclusions and Future Work

6.1 Summary of Thesis

This thesis work successfully developed a field-effect transistor platform and LSPR plasmonic platforms with significant advantages for cytokine biomarker detection. In our first study using MoS_2 based field-effect transistors, we achieved rapid, ultra-high sensitivity biosensor for measuring cytokine biomarkers and their surface binding kinetics. In our second study, we demonstrated temporal profiling of the T-cell functional response under immunomodulatory agent exposure using the microarray-type LSPR nanoplasmonic optofluidic device. In this work, we successfully characterized the cytokine secretion behavior of T cells for multiple analytes with a rapid, high-sensitivity, and high-throughput platform. In our third study, we developed an integrated LSPR plasmonic biosensor with microfluidic system for cell secretion assay. This work demonstrated an optofluidic device allowing for on-chip cell separation, stimulation,

incubation and *in situ* measurement of cell-secreted cytokines for human blood samples. A summary of all the presented accomplishments is given in the following sections.

6.1.1 MoS_2-based Field-effect Transistor Biosensor for Cytokine Biomarker Detection

In this study, we demonstrated important device physics and metrics for calibrating the responses of MoS2 transistor biosensors and validated that multiple sensors can be used to enable quantification of low-abundance biomarker molecules as well as the affinities and kinetics of antibody-antigen mediated binding events. In particular, our biosensors showed a TNF-α detection limit at least as low as 60 fM. This low detection limit can be obtained in both linear and subthreshold regimes of MoS2 transistors. We further observed that the sensors worked in the subthreshold regime presented higher current sensitivities in comparison with those in the linear regime. The high subthreshold-regime sensitivities pose significant potential to further lowering down the TNF-α detection limit. In both transport regimes, the detected current signals can be normalized into response quantities independent of the transistor performance, which can efficiently reduce the effect of sensor-to-sensor difference on detecting biomolecules. Based on this calibration method, all sets of our biosensors generated consistent sensor responses with respect to TNF-α concentration and therefore a standard curve for TNF-α quantification was obtained. From this standard curve, the equilibrium constant of the (TNF-α)-antibody pair was calculated to be K_D=369±48 fM for linear-regime responses (or K_D = 424 ± 70 fM for subthreshold-regime responses). Furthermore, the real-time association/dissociation processes of the (TNF-α)-antibody pair were also measured using

multiple sensors. The association/dissociation rates were calculated to be k_{on} = (5.03 ± 0.16) × 108 $M^{-1}s^{-1}$ and k_{off} = (1.97±0.08)×10^{-4} s^{-1}, respectively. This work pose an important foundation for leveraging the excellent electronic properties of emerging atomically layered semiconductors in bio-assay applications, as well as advanced research capability in analyzing biomolecule interactions with fM-level detection sensitivities. Of note, such capability would enable selection of antibodies with a high binding constant with respect to a specific target biomarker molecule, thereby providing a means to further improve the selectivity and reliability of immunoassay.

6.1.2 Multiplexed Nanoplasmonic Biosensor for Temporal Profiling of Cytokines

In this study, we demonstrated the use of LSPR nanoplasmonic biosensor microarrays for obtaining temporal cytokine secretion profiles of T cells under immunosuppressive modulation. Our cytokine secretion assay was rapid, sensitive, and easy to implement for multiplexed, multi-time-point detection. The multiplexed time-course cytokine secretion data obtained from this work enabled us to characterize dynamic features of the functional response of Jurkat T cells after their exposure to an immunosuppressant. The rapid reaction of T cells to the agent clearly reflected its effect in quickly altering cytokine-mediated pro-inflammatory intracellular signaling pathways. To the best of our knowledge, this study is the first to quantitatively characterize dynamic cytokine secretion behaviors under immunosuppressive modulation.

The T-cell functional response is governed by an orchestration of dynamic secretions of multiple cytokine species. Thus, of particular importance in the current study is the demonstrated ability of our method to probe the temporal secretion profiles of

four target cytokines (IL-2, IFN-γ, TNF-α, and IL-10) from T cells. The multi-analyte, multi-time-point detection provided a unique opportunity to obtain a broad picture of cellular functional states rapidly modulated by immunosuppressive agents. Variations in the degree and timing of the TAC-induced secretion suppression across these cytokines under a given drug administration condition offer important and clinically relevant insight to more precisely modulate immune responses beyond the historically standard practice of monitoring serum drug levels. For example, by monitoring both IL-2 and IFN-γ secretion profiles under various TAC doses, we may be able to quickly (< 60 min) estimate a minimum amount of TAC required to inhibit the IL-2-mediated inflammatory response of T cells while maintaining a sufficient level of IFN-γ mediated anti-viral responses. This could prevent overdosing of the immunosuppressant, which could induce adverse effects and cause diseases with over-suppressed innate immunity. In addition, our study suggests that comparing the secretion profile of IL-10 to those of IL-2 and IFN-γ may provide critical information about the T cell's real-time feedback control of pro-inflammatory cytokine secretion via autocrine/paracrine secretion signaling pathways.

The cellular functional monitoring capability demonstrated by the LSPR nanoplasmonic biosensor microarrays may serve as a technological platform to provide precise and personalized real-time immune regulation treatments. With this capability, one may precisely assess temporal variations of the functional behaviors of T cells for a given immunosuppressive agent delivery condition. We envision that our nanoplasmonic biosensing platform will be used as a drug efficacy-screening tool for future personalized medicine while providing detailed information of the immunomodulatory effect of a given agent on the functional behaviors of immune cells.

6.1.3 Integrated Nanoplasmonic Biosensor for Cytokine Secretion Assay

We have developed a novel optofluidic biosensing technique for cellular functional immunoanalysis based on nanoplasmonic LSPR detection. The multifunctional device used in our assay can achieve cell isolation and enrichment, incubation and stimulation, and detection of cell-secreted cytokines on a single chip platform. Our technique successfully demonstrated two noteworthy features. Firstly, the developed technique enabled on-chip trapping of microbead-bound cells with at efficiency over 95% by its micro-pillar arrays. Using the develop LSPR platform device, we successfully demonstrated direct isolation of PBMCs from human blood samples and their immunofunctional analysis. Our technique allowed blood-sample assays by selectively trapping bead-bound CD45+ PBMCs inside a microfluidic chamber while filtering out other undesired blood components. Coupled with the microbead/micropillar-based cell trapping and isolation, our integrated LSPR optofluidic platform provided a novel approach for achieving cellular functional immunoanalysis while eliminating laborious blood sample preparation. To the best of our knowledge, this study is the *first* to demonstrate human blood cellular immunophenotyping with the label-free LSPR nanoplasmonic detection technique. Secondly, our LSPR device is capable of leveraging the LSPR detection for rapid quantification of small-sized, physiologically-relevant cytokines. Our on-chip assay technique incorporated the scheme of confining cells and analyte molecules within a small ($3\ \mu L$) microfluidic chamber, which effectively maintained a high level of concentration even if the absolute number of TNF-α molecules presented to the detection surface was small. This spatial confinement scheme simultaneously achieved assay volume reduction and signal amplification to overcome

the limited sensitivity of LSPR biosensing for cytokine detection. Additionally, the short diffusion path of analytes within the microfluidic chamber allowed the system to rapidly reach the equilibrium state. This reduced the assay time for reagent incubation and LSPR sensing surface preparation, thus decreasing the total assay time. The whole assay process of our technique took only 4 - 5 hours whereas the conventional ELISA method could take nearly 2 days for the same cytokine secretion assay with immune cells.

The limited ability to detect the surface binding of small-sized analytes and the difficulty of handling the complex sample components have prohibited researchers from implementing the LSPR technique for cytokine secretion assays with human blood samples. Our study has successfully overcome these obstacles by the synergistic integration of microfluidic sample handling and separation and integrated LSPR biosensing. Our technique may open the door for a wider use of LSPR biosensing in clinical diagnosis of inflammatory diseases with a simple setup similar to the one used in this study. It could also provide multiplex cytokine detection or a foundation for dynamic *in-situ* monitoring of the cytokine secretion function of immune cells to obtain new insight into cellular immunology in the future.

6.2 Future Research and Applications

Continued work on label-free biosensing platforms for cytokine detection will have a prominent impact on several research applications. The future work of field-effect transistor biosensing technique could explore the development of a multiplexed cytokine detection platform. This platform will have great potential to offer rapid, sensitive and high throughput biosensors for point-of-care diagnosis. The future work of plasmonic

biosensing will implement a cell culture platform incorporating a sensitive nanoparticle-based plasmonic biosensors integrated in a microfluidic system. This microfluidic biosensor integration approach will allow us to simultaneously measure multiple cytokines secreted from immune cells and obtain the parameters signifying the time-varying immune cell response, such as secretion rate, secretion timing and secretion time constant, in addition to the cytokine quantity.

6.2.1 Multiplexed Cytokine Biomarker Detection with FET Biosensors

We envision that the rapidness and high sensitivity of the label-free FET based biosensing platform will facilitate effective characterization of the dynamic nature of the immune functional response of a host. However, the current platform targets a single cytokine species for each sample. As mentioned in the thesis, multiple cytokines play critical roles to regulate the immune system while involving complex cytokine communication networks. To provide a comprehensive understanding of the cytokine-mediated immune response, only measuring a single type of cytokine is unlikely to be sufficient. Detecting multiple cytokines would provide more accurate information about patient's immune conditions. For example, some T-cells are polyfunctional, which is that they secrete multiple types of cytokines (e.g. tumor necrosis factor-α (TNF-α), interferon-γ (IFN-γ), interleukin-6 (IL-6), IL-10, etc.) according to external stimulation. These cytokines are known to positively or negatively secrete from T cells under certain disease condition [161]. Thus, scrutinizing multiple types of cytokine will provide more comprehensive and accurate information about immune condition.

To develop a multiplexed FET biosensing platform for cytokine measurement, we propose to apply a new patterning technique to fabricate sensor arrays functionalized with multiple probe antibodies on a single substrate. Recently, Nam et al. demonstrated MoS_2 nanofabrication technique to transfer prepatterned bulk MoS_2 material on a silicon substrate and fabricated an array of few-layer MoS_2 FET biosensors (Figure 6.1) [90]. We propose to employ this technique to construct few layer MoS_2 flake arrays on a silicon substrate, Subsequently, a PDMS microfluidic channel device will be utilized for selectively functioning different FET biosensor array regions with several types of probe antibodies. We will replace the first PDMS fluidic device with another PDMS layer with microfluidic channels and orthogonally cover the sensing array spots with the new PDMS layer. Assay samples loaded to the device will be able to meet with several different types of probe antibodies, which will allow for multiplexed cytokine measurement from a single sample.

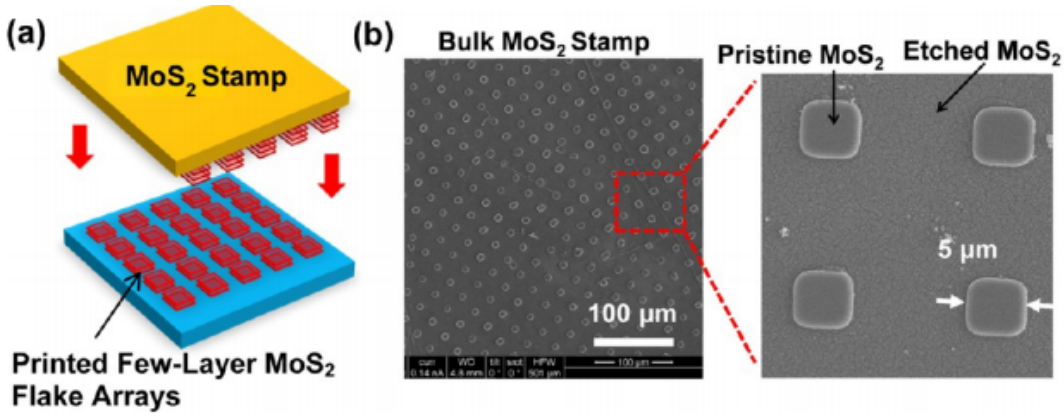

Figure 6.1: (a) Direct transfer printing of prepatterned few-layer MoS_2 flakes onto the substrate. (b) SEM images of a bulk MoS_2 stamp prestructured periodic pillars [90].

It is known that FET biosensors are susceptible to background noise when using complex physiological fluidic samples. Thus, we propose to use diluted human serum samples to diagnose the immune response of the host based on the multiplexed cytokine

measurement. The developed device providing rapid, sensitive, and multiplex cytokine analysis capability will have great potential for a fast, accurate diagnosing tool of scanning immune related diseases under a point-of-care setting.

6.2.2 In situ Cell Secreted Cytokine Measurement with Integrated Plasmonic Biosensors

As mentioned in the beginning of this thesis, immune cell responses are most often characterized by their cytokine secretion behaviors. Characterizing cytokine secretion patterns of immune cells in the bloodstream, lymph nodes, or tissue provides the means to monitor immune responses in humans. Multiplexed detection of different cytokines has been proven powerful for obtaining a more complete picture of immunity [162]. Comprehensive, near real-time monitoring of immune cell secreted cytokine patterns is critical for developing fundamental knowledge of the impact of therapeutic treatments in conditions such as allergy, asthma, autoimmunity, acquired and primary immunodeficiency, transplantation, and infection. In the future, immunomodulatory therapies (including immunosuppression) may be tailored to an individual's immune status based on a panel of their immune cells' functions. As pro- and anti-inflammatory processes occur simultaneously along different time lines for different subpopulations of immune cells, this capability includes identifying unresponsive, or so-called "immunoparalyzed" cells in the relevant clinical context [163]. Thus, different subpopulations of immune cells may concurrently exhibit pro- and anti-inflammatory processes. This observation may be particularly relevant in the setting of acute inflammatory diseases such as sepsis [164] and Crohn's disease [165], in which both "pro-" and "anti-inflammatory phenotypes" have been occurred. Thus, it is important to

develop an immunoassay platform that can measure the functional status of different subpopulations of immune cells in near real-time (Figure 6.2).

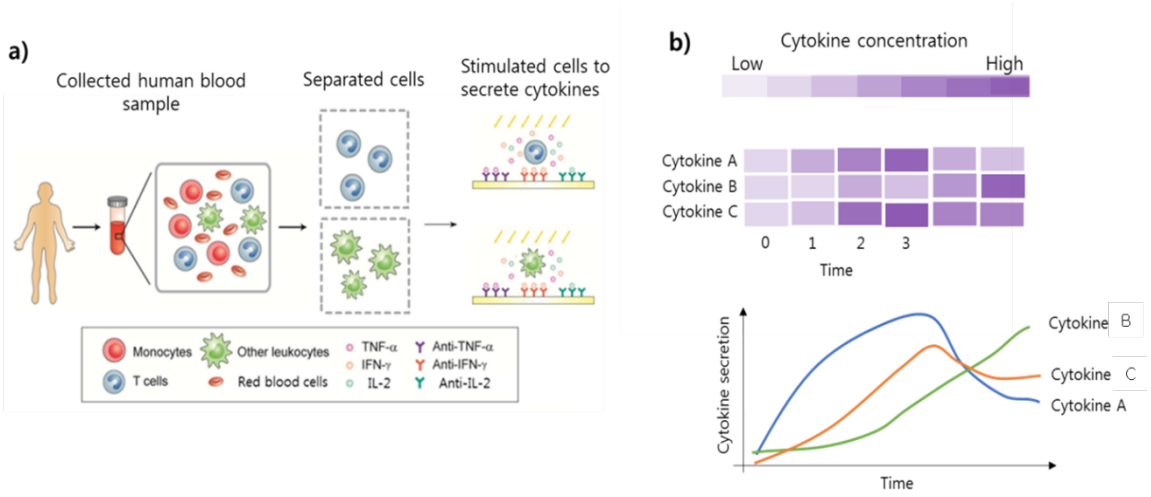

Figure 6.2: Functional immunophenotyping of immune cells. a) Cytokine secretion assay process [142], and b) multi-parametric data obtained from stimulated immune cells.

Integrated label-free plasmonic biosensors in a microfluidic system could be a solution to enable us to study immune cellular response in near real-time. The proposed platform could provide features such as rapidness, high sensitivity, multiplexity, and sensor proximity to cells by combining concepts presented by the two previous plasmonic based biosensing techniques (Chapter 4,5). Nanoparticle based LSPR biosensor will be fabricated by following the protocols from the previous work (Chapter 4) and several types of probe antibodies will be coated on the sensing elements. The prepared sensing substrate will be covered with a PDMS microfluidic device with micro-pillar arrays for cell separation (Chapter 5). Captured cells will be incubated and stimulated in the device by cell stimulant (e.g. LPS, PMA, and Ionomycine) or drug to modulate cells to secret cytokines. The sensing elements placed near the cell incubation area, will simultaneously

detect cytokines secreted from the cells and the quantification result is used for scanning the cellular immune response.

This proposed platform will enable quantitative analysis of multiple cytokine species secreted from various immune cell subpopulations. This platform should allow us to quantitatively observe variations in the cellular immune functions over the course of diseases and/or during immunomodulatory therapy. Such an innovative platform will not only guide accurate patient stratification but also transform clinical practice by guiding precise immunotherapy beyond population-derived drug levels.

Appendices

A. Fabrication of MoS2 based FET biosensor

A.1. Thermal-grown 300nm Silicon Oxide Wafer Cleaning

1. RCA clean; DI water : NH_4OH : H_2O_2 = 5 : 1 : 1, 75 °C, 10 min

A.2. Fabrication of MoS_2 Stamp

1. Prepare a piece of pristine bulk MoS_2 on a copper tape
2. Spin-coat a photoresist layer (SPR 220 3.0) on the MoS_2 piece (CEE 100CB photoresist spinner: 3000 rpm, 40 s, Bake: 115 °C, 60 s)
3. Pattern the photoresist layer spin-coated on top of the MoS_2 surface by photolithography (MA-BA-6 Mask-Bond Aligner: 7 s)
4. Develop exposed layer (MF-319: 60 s)
5. Deposit 100 nm Ti masks (Enerjet Evaporator) followed with lift-off in acetone
6. Perform SF_6-based reactive ion etching (RIE) to transfer the Ti mask pattern onto underlying MoS_2 (Plasmatherm 790: SF_6 10s, 20mTorr, 20sccm, 200W, 2 min)
7. Remove Ti masks in hydrofluoric (HF) acid followed with DI water rinse

A.3. Print out few-layer-MoS_2 flakes onto the SiO_2 substrate

A.4. Fabrication of metal electrodes

1. Spin-coat a photoresist layer (SPR 220 3.0) on the SiO_2 substrate with MoS_2 flakes (CEE 100CB photoresist spinner: 3000 rpm, 40 s, Bake: 115 °C, 60 s)

2. Align a mask for electrodes and pattern the photoresist layer spin-coated on top of the MoS_2 surface by photolithography (MA-BA-6 Mask-Bond Aligner: 7 s)
3. Develop exposed layer (MF-319: 60 s)
4. Deposit 10/50 nm Ti/Au layers (Enerjet Evaporator) followed with lift-off in acetone

A.5. Deposrt HfO_2 layer

Deposit 30 nm HfO_2 layer using atomic layer deposition (ALD) for functionalization of biomolecules (Oxford OpAL ALD: 275 °C water-based recipe)

A.6. Deposit SiOx layer

Deposit 100nm SiO_x layer using an ion-beam sputter for passivation of electrodes (Kurt J. Lesker Lab 18-1)

B. Fabrication of Microfluidic Channel Device

B.1. Fabrication of Microfluidic Channel Mold

1. Photoresist Patterning
    1) Spin coat 3 μm SPR220 photoresist and softbake at 115°C for 90s, manually or using ACS 200 cluster tool.
    2) Expose the photoresist using MA/BA-6 Mask Aligner (Exposure intensity ~20 J/s) for 6 s.
    3) Developed the exposed photoresist using AZ 300 developer for 40 s, manually or using ACS 200 cluster tool.
2. Plasma Etching

    Etch silicon using deep reactive ion-etching (DRIE; Deep Silicon Etcher, STS; Recipe-LNF Pegasus Recipe 1; Etch rate ~ 5 μm/min).
3. Silicon Surface Silanization
    1) O_2 Plasma active the silicon mold surface in March Asher (O_2, 80W, 250mT, 45s)
    2) Place silicon mold in a vauum desiccator and load 100 μL of Silane (tridecafluoro-1 ,1, 2, 2-tetrahydrooctyl)-1-trichlorosilane (United Chemical Technologies) for 1 hr under vacuum.

B.2. Fabrication of PDMS Channel

1. PDMS Precursor Preparation
    1) Mix the Sylgard 184 base and curing agent in weight ratio of 10:1.

2) Degas in vacuum desiccator for 30- 60 min.

2. PDMS Soft Lithography

    1) Place the silanized silicon mold in petri dish.

    2) Pour PDMS over the mold (Thickness 4-9 mm).

    3) Degas in the desiccator for 30-60 min.

    4) Cure PDMS in the oven (60 °C 4 hr- overnight).

    5) Cool down the baked PDMS in ambient.

    6) Peel off PDMS from silicon wafer.

3. Inlet/Outlet Fabrication

    Punch holes through PDMS using Biopsy punch, ∅ 0.75- 1mm.

C. Fabrication of Nanoparticle based LSPR Microarray Device

C.1. Pyrex Glass Slide Clean

1) Piranha Clean (H_2SO_4 : H_2O_2 = 3 : 1) for 10 min.
2) DI water rinse and dry with N_2 gas or air.

C.2. Nanorod Patterning on the Glass Slide

1) Prepare nanorod collide solution (Nanoseedz, Hongkong) and dilute 8 times with DI water.
2) Prepare Piranha cleaned glass and O_2 plasma treat the glass surface and PDMS microfluidic channel with 20 W for 120 s right before patterning.
3) Assemble the glass slide surface with PDMS microfluidic channel and load nanorod solution using syringe infusion pump through inlet and incubate the solution 2 hr- overnight to form the nanoparticle patterns.

C.3. Functioning the Nanoparticles for Sensing

1) Wash the incubated surface with loading DI water through microfluidic channel.
2) 1mM of 10-carboxy-1-decanethiol (C10) (Dojindo, Japan) was dissolved in 10% ethanol, loaded into the microfluidic patterning channels, and incubated overnight to functionalize the AuNR surfaces with C10.
3) Wash the incubated surface with loading DI water through microfluidic channel.
4) 0.4 M EDC (1-ethyl-3-[3-dimethylaminopropyl] carbodiimide hydrochloride, Thermo Scientific) and 0.1 M NHS (N-hydroxysuccinimide, Thermo

Scientific) were mixed at a 1:1 volume ratio in 0.1 M MES (1-ethyl-3-[3-dimethylaminopropyl] carbodiimide hydrochloride, Thermo Scientific) solution. 10 μL of the EDC/NHS/MES solution was loaded to the same microfluidic channels and incubated for 20 min to activate the ligand.

5) Wash the incubated surface with loading DI water through microfluidic channel.
6) Load selected probe antibodies at a concentration of 50 μg/mL (diluted in deionized water) into individual patterning channel and incubated for 45 - 60 min.

D. Microbead and Human Blood Cell Conjugation

D.1. Lysing the Blood Sample

1) Prepare 1 mL of blood sample and add 10 mL lysed buffer. Well mix the medium and incubate for 12 min.
2) Add 20-30 mL pf PBS and centrifuge cells 10 min, 300-400G.
3) Aspirate all the red blood cells and suspend the cells in 1 mL of RPMI cell culture medium.

D.2. Mirospheres 130preparation

1) Prepare microspheres and wash the particles (1-3 times) with 10× volume of DI water (e.g. 100 μL of beads + 1mL of DI water).
2) Centrifuge (1200G for 15min) and resuspend the final pellet in wash buffer to make the microsphere concentration of 0.05% solids (0.5mg/mL) (e.g. Aspirate DI water and add 2mL of 10X PBS). Final washing buffer should be 0.1M PBS (10X PBS) of pH 7.4.
3) Add biotinylated IgG (CD45 antibody) into 2) solution that has been dissolved in the same buffer. (e.g. Prepare 1mL of beads + 40uL of Antibody)
4) Incubate 30min in room temperature with gentle mix.
5) Wash the particles 3 times with 10X volume of DI water. (e.g. 1080uL solution + 10mL of DI water)
6) Resuspend antibody-coated beads in 0.1M PBS of pH 7.4 (10X PBS), to desired storage concentration.

D.3. Microbead and Cell Conjugation

1) Mix the prepared microsphere beads with lysed cells (The number of bead : cell =1:1 is recommended).
2) Incubate mixed particles for 30min in the room temperature with gentle mix.

Bibliography

[1] P. Y. Chen, N. T. Huang, M. T. Chung, T. T. Cornell, and K. Kurabayashi, "Label-free cytokine micro- and nano-biosensing towards personalized medicine of systemic inflammatory disorders," *Advanced Drug Delivery Reviews,* vol. 95, pp. 90-103, Dec 2015.

[2] D. L. Lefkowitz and S. S. Lefkowitz, "Macrophage-neutrophil interaction: A paradigm for chronic inflammation revisited," *Immunology and Cell Biology,* vol. 79, pp. 502-506, Sep 2001.

[3] C. Hartono, T. Muthukumar, and M. Suthanthiran, "Immunosuppressive Drug Therapy," *Cold Spring Harbor Perspectives in Medicine,* vol. 3, p. 15, Sep 2013.

[4] K. Tsuda, K. Yamanaka, H. Kitagawa, T. Akeda, M. Naka, K. Niwa*, et al.*, "Calcineurin Inhibitors Suppress Cytokine Production from Memory T Cells and Differentiation of Naive T Cells into Cytokine-Producing Mature T Cells," *Plos One,* vol. 7, p. 5, Feb 2012.

[5] J. K. Kundu and Y. J. Surh, "Inflammation: Gearing the journey to cancer," *Mutation Research-Reviews in Mutation Research,* vol. 659, pp. 15-30, Jul-Aug 2008.

[6] W. Schulte, J. Bernhagen, and R. Bucala, "Cytokines in Sepsis: Potent Immunoregulators and Potential Therapeutic Targets-An Updated View," *Mediators of Inflammation,* p. 16, 2013.

[7] M. Pai, L. W. Riley, and J. M. Colford, "Interferonn assays-gamma in the immunodiagnosis of tuberculosis: a systematic review," *Lancet Infectious Diseases,* vol. 4, pp. 761-776, Dec 2004.

[8] C. Y. Lin, G. W. Roberts, A. Kift-Morgan, K. L. Donovan, N. Topley, and M. Eberl, "Pathogen-Specific Local Immune Fingerprints Diagnose Bacterial Infection in Peritoneal Dialysis Patients," *Journal of the American Society of Nephrology,* vol. 24, pp. 2002-2009, Dec 2013.

[9] S. A. Rosenberg, J. C. Yang, and N. P. Restifo, "Cancer immunotherapy: moving beyond current vaccines," *Nature Medicine,* vol. 10, pp. 909-915, Sep 2004.

[10] J. F. Rusling, C. V. Kumar, J. S. Gutkind, and V. Patel, "Measurement of biomarker proteins for point-of-care early detection and monitoring of cancer," *Analyst,* vol. 135, pp. 2496-2511, 2010.

[11] B. V. Chikkaveeraiah, A. A. Bhirde, N. Y. Morgan, H. S. Eden, and X. Y. Chen, "Electrochemical Immunosensors for Detection of Cancer Protein Biomarkers," *Acs Nano,* vol. 6, pp. 6546-6561, Aug 2012.
[12] L. Gullestad, T. Ueland, L. E. Vinge, A. Finsen, A. Yndestad, and P. Aukrust, "Inflammatory Cytokines in Heart Failure: Mediators and Markers," *Cardiology,* vol. 122, pp. 23-35, 2012.
[13] M. Reale, M. A. Kamal, L. Velluto, D. Gambi, M. Di Nicola, and N. H. Greig, "Relationship between Inflammatory Mediators, A beta Levels and ApoE Genotype in Alzheimer Disease," *Current Alzheimer Research,* vol. 9, pp. 447-457, May 2012.
[14] S. Siebert, A. Tsoukas, J. Robertson, and I. McInnes, "Cytokines as Therapeutic Targets in Rheumatoid Arthritis and Other Inflammatory Diseases," *Pharmacological Reviews,* vol. 67, pp. 280-309, Apr 2015.
[15] S. R. Targan, S. B. Hanauer, S. J. H. vanDeventer, L. Mayer, D. H. Present, T. Braakman*, et al.*, "A short-term study of chimeric monoclonal antibody cA2 to tumor necrosis factor alpha for Crohn's disease," *New England Journal of Medicine,* vol. 337, pp. 1029-1035, Oct 1997.
[16] J. X. Lin, T. S. Migone, M. Tsang, M. Friedmann, J. A. Weatherbee, L. Zhou*, et al.*, "THE ROLE OF SHARED RECEPTOR MOTIFS AND COMMON STAT PROTEINS IN THE GENERATION OF CYTOKINE PLEIOTROPY AND REDUNDANCY BY IL-2, IL-4, IL-7, IL-13, AND IL-15," *Immunity,* vol. 2, pp. 331-339, Apr 1995.
[17] J. A. Stenken and A. J. Poschenrieder, "Bioanalytical chemistry of cytokines - A review," *Analytica Chimica Acta,* vol. 853, pp. 95-115, Jan 2015.
[18] J. Bienvenu, G. Monneret, N. Fabien, and J. P. Revillard, "The clinical usefulness of the measurement of cytokines," *Clinical Chemistry and Laboratory Medicine,* vol. 38, pp. 267-285, Apr 2000.
[19] M. L. Schmitz, A. Weber, T. Roxlau, M. Gaestel, and M. Kracht, "Signal integration, crosstalk mechanisms and networks in the function of inflammatory cytokines," *Biochimica Et Biophysica Acta-Molecular Cell Research,* vol. 1813, pp. 2165-2175, Dec 2011.
[20] R. A. Seder, P. A. Darrah, and M. Roederer, "T-cell quality in memory and protection: implications for vaccine design (vol 8, pg 247, 2008)," *Nature Reviews Immunology,* vol. 8, p. 1, Jun 2008.
[21] M. S. Luchansky and R. C. Bailey, "Rapid, Multiparameter Profiling of Cellular Secretion Using Silicon Photonic Microring Resonator Arrays," *Journal of the American Chemical Society,* vol. 133, pp. 20500-20506, Dec 2011.
[22] H. K. Hunt and A. M. Armani, "Label-free biological and chemical sensors," *Nanoscale,* vol. 2, pp. 1544-1559, 2010.
[23] D. Sarkar, W. Liu, X. J. Xie, A. C. Anselmo, S. Mitragotri, and K. Banerjee, "MoS2 Field-Effect Transistor for Next-Generation Label-Free Biosensors," *Acs Nano,* vol. 8, pp. 3992-4003, Apr 2014.
[24] M. Chhowalla, H. S. Shin, G. Eda, L. J. Li, K. P. Loh, and H. Zhang, "The chemistry of two-dimensional layered transition metal dichalcogenide nanosheets," *Nature Chemistry,* vol. 5, pp. 263-275, Apr 2013.

[25] B. Radisavljevic, A. Radenovic, J. Brivio, V. Giacometti, and A. Kis, "Single-layer MoS2 transistors," *Nature Nanotechnology,* vol. 6, pp. 147-150, Mar 2011.
[26] T. Korn, S. Heydrich, M. Hirmer, J. Schmutzler, and C. Schuller, "Low-temperature photocarrier dynamics in monolayer MoS2," *Applied Physics Letters,* vol. 99, p. 3, Sep 2011.
[27] K. F. Mak, C. Lee, J. Hone, J. Shan, and T. F. Heinz, "Atomically Thin MoS2: A New Direct-Gap Semiconductor," *Physical Review Letters,* vol. 105, p. 4, Sep 2010.
[28] J. Wang, M. Lundstrom, and I. Electronic Devices Society Of, "Does source-to-drain tunneling limit the ultimate scaling of MOSFETs?," *International Electron Devices 2002 Meeting, Technical Digest,* pp. 707-710, 2002.
[29] M. Bernardi, M. Palummo, and J. C. Grossman, "Extraordinary Sunlight Absorption and One Nanometer Thick Photovoltaics Using Two-Dimensional Monolayer Materials," *Nano Letters,* vol. 13, pp. 3664-3670, Aug 2013.
[30] L. Britnell, R. M. Ribeiro, A. Eckmann, R. Jalil, B. D. Belle, A. Mishchenko*, et al.*, "Strong Light-Matter Interactions in Heterostructures of Atomically Thin Films," *Science,* vol. 340, pp. 1311-1314, Jun 2013.
[31] G. Eda and S. A. Maier, "Two-Dimensional Crystals: Managing Light for Optoelectronics," *Acs Nano,* vol. 7, pp. 5660-5665, Jul 2013.
[32] H. Y. Chang, S. X. Yang, J. H. Lee, L. Tao, W. S. Hwang, D. Jena*, et al.*, "High-Performance, Highly Bendable MoS2 Transistors with High-K Dielectrics for Flexible Low-Power Systems," *Acs Nano,* vol. 7, pp. 5446-5452, Jun 2013.
[33] H. Wang, L. L. Yu, Y. H. Lee, Y. M. Shi, A. Hsu, M. L. Chin*, et al.*, "Integrated Circuits Based on Bilayer MoS2 Transistors," *Nano Letters,* vol. 12, pp. 4674-4680, Sep 2012.
[34] A. Ayari, E. Cobas, O. Ogundadegbe, and M. S. Fuhrer, "Realization and electrical characterization of ultrathin crystals of layered transition-metal dichalcogenides," *Journal of Applied Physics,* vol. 101, p. 5, Jan 2007.
[35] J. Pu, Y. Yomogida, K. K. Liu, L. J. Li, Y. Iwasa, and T. Takenobu, "Highly Flexible MoS2 Thin-Film Transistors with Ion Gel Dielectrics," *Nano Letters,* vol. 12, pp. 4013-4017, Aug 2012.
[36] C. N. R. Rao, K. Biswas, K. S. Subrahmanyam, and A. Govindaraj, "Graphene, the new nanocarbon," *Journal of Materials Chemistry,* vol. 19, pp. 2457-2469, 2009.
[37] P. Avouris, "Graphene: Electronic and Photonic Properties and Devices," *Nano Letters,* vol. 10, pp. 4285-4294, Nov 2010.
[38] W. J. Zhu, D. Neumayer, V. Perebeinos, and P. Avouris, "Silicon Nitride Gate Dielectrics and Band Gap Engineering in Graphene Layers," *Nano Letters,* vol. 10, pp. 3572-3576, Sep 2010.
[39] Y. Q. Wu, Y. M. Lin, K. A. Jenkins, J. A. Ott, C. Dimitrakopoulos, D. B. Farmer*, et al.*, "RF Performance of Short Channel Graphene Field-Effect Transistor," *2010 International Electron Devices Meeting - Technical Digest,* p. 3, 2010.
[40] M. J. Allen, V. C. Tung, and R. B. Kaner, "Honeycomb Carbon: A Review of Graphene," *Chemical Reviews,* vol. 110, pp. 132-145, Jan 2010.
[41] S. Townsend, W. J. J. Finlay, S. Hearty, and R. O'Kennedy, "Optimizing recombinant antibody function in SPR immunosensing - The influence of

antibody structural format and chip surface chemistry on assay sensitivity," *Biosensors & Bioelectronics,* vol. 22, pp. 268-274, Aug 2006.
[42] A. G. Brolo, "Plasmonics for future biosensors," *Nature Photonics,* vol. 6, pp. 709-713, Nov 2012.
[43] T. A. Duncombe, A. M. Tentori, and A. E. Herr, "Microfluidics: reframing biological enquiry," *Nature Reviews Molecular Cell Biology,* vol. 16, pp. 554-567, Sep 2015.
[44] T. D. Ray, L. A. Lewis, S. Gulati, P. A. Rice, and S. Ram, "Characterization of antibodies in human serum against group B Neisseria meningitidis that block complement-dependent bactericidal activity," *Molecular Immunology,* vol. 47, pp. 2247-2247, Aug 2010.
[45] A. L. Timko, C. H. Miller, F. B. Johnson, and V. Ross, "In vitro quantitative chemical analysis of tattoo pigments," *Archives of Dermatology,* vol. 137, pp. 143-147, Feb 2001.
[46] B. P. Timko, T. Cohen-Karni, Q. Qing, B. Z. Tian, and C. M. Lieber, "Design and Implementation of Functional Nanoelectronic Interfaces With Biomolecules, Cells, and Tissue Using Nanowire Device Arrays," *Ieee Transactions on Nanotechnology,* vol. 9, pp. 269-280, May 2010.
[47] G. F. Zheng, F. Patolsky, Y. Cui, W. U. Wang, and C. M. Lieber, "Multiplexed electrical detection of cancer markers with nanowire sensor arrays," *Nature Biotechnology,* vol. 23, pp. 1294-1301, Oct 2005.
[48] M. R. Jacobs and C. E. Good, "Residual Bacterial Contamination of Apheresis Platelets Following Early Culture - Results of a Multi-Site Study of 18,449 Units Using the Verax Pan Genera Detection Assay," *Transfusion,* vol. 50, pp. 30A-30A, Sep 2010.
[49] Y. K. Vashist, G. Uzungolu, A. Kutup, F. Gebauer, A. Koenig, L. Deutsch*, et al.*, "Heme Oxygenase-1 Germ Line GTn Promoter Polymorphism is an Independent Prognosticator of Tumor Recurrence and Survival in Pancreatic Cancer," *Journal of Surgical Oncology,* vol. 104, pp. 305-311, Sep 2011.
[50] Y. X. Huang, H. G. Sudibya, D. L. Fu, R. H. Xue, X. C. Dong, L. J. Li*, et al.*, "Label-free detection of ATP release from living astrocytes with high temporal resolution using carbon nanotube network," *Biosensors & Bioelectronics,* vol. 24, pp. 2716-2720, Apr 2009.
[51] H. G. Sudibya, J. M. Ma, X. C. Dong, S. Ng, L. J. Li, X. W. Liu*, et al.*, "Interfacing Glycosylated Carbon-Nanotube-Network Devices with Living Cells to Detect Dynamic Secretion of Biomolecules," *Angewandte Chemie-International Edition,* vol. 48, pp. 2723-2726, 2009.
[52] X. X. Duan, Y. Li, N. K. Rajan, D. A. Routenberg, Y. Modis, and M. A. Reed, "Quantification of the affinities and kinetics of protein interactions using silicon nanowire biosensors," *Nature Nanotechnology,* vol. 7, pp. 401-407, Jun 2012.
[53] W. R. Yang, K. R. Ratinac, S. P. Ringer, P. Thordarson, J. J. Gooding, and F. Braet, "Carbon Nanomaterials in Biosensors: Should You Use Nanotubes or Graphene?," *Angewandte Chemie-International Edition,* vol. 49, pp. 2114-2138, 2010.
[54] T. S. Pui, A. Agarwal, F. Ye, Y. X. Huang, and P. Chen, "Nanoelectronic detection of triggered secretion of pro-inflammatory cytokines using CMOS

compatible silicon nanowires," *Biosensors & Bioelectronics,* vol. 26, pp. 2746-2750, Jan 2011.
[55] E. Stern, J. F. Klemic, D. A. Routenberg, P. N. Wyrembak, D. B. Turner-Evans, A. D. Hamilton*, et al.*, "Label-free immunodetection with CMOS-compatible semiconducting nanowires," *Nature,* vol. 445, pp. 519-522, Feb 2007.
[56] F. S. Zhou and Q. H. Wei, "Scaling laws for nanoFET sensors," *Nanotechnology,* vol. 19, p. 7, Jan 2008.
[57] J. F. Huang, H. Chen, W. B. Niu, D. W. H. Fam, A. Palaniappan, M. Larisika*, et al.*, "Highly manufacturable graphene oxide biosensor for sensitive Interleukin-6 detection," *Rsc Advances,* vol. 5, pp. 39245-39251, 2015.
[58] Q. Y. He, Z. Y. Zeng, Z. Y. Yin, H. Li, S. X. Wu, X. Huang*, et al.*, "Fabrication of Flexible MoS2 Thin-Film Transistor Arrays for Practical Gas-Sensing Applications," *Small,* vol. 8, pp. 2994-2999, Oct 2012.
[59] D. J. Late, Y. K. Huang, B. Liu, J. Acharya, S. N. Shirodkar, J. J. Luo*, et al.*, "Sensing Behavior of Atomically Thin-Layered MoS2 Transistors," *Acs Nano,* vol. 7, pp. 4879-4891, Jun 2013.
[60] L. Wang, Y. Wang, J. I. Wong, T. Palacios, J. Kong, and H. Y. Yang, "Functionalized MoS2 Nanosheet-Based Field-Effect Biosensor for Label-Free Sensitive Detection of Cancer Marker Proteins in Solution," *Small,* vol. 10, pp. 1101-1105, Mar 2014.
[61] J. Homola, "Surface plasmon resonance sensors for detection of chemical and biological species," *Chemical Reviews,* vol. 108, pp. 462-493, Feb 2008.
[62] O. R. Bolduc, L. S. Live, and J. F. Masson, "High-resolution surface plasmon resonance sensors based on a dove prism," *Talanta,* vol. 77, pp. 1680-1687, Mar 2009.
[63] P. Y. Chen, M. T. Chung, W. McHugh, R. Nidetz, Y. W. Li, J. P. Fu*, et al.*, "Multiplex Serum Cytokine Immunoassay Using Nanoplasmonic Biosensor Microarrays," *Acs Nano,* vol. 9, pp. 4173-4181, Apr 2015.
[64] T. H. Chou, C. Y. Chuang, and C. M. Wu, "Quantification of Interleukin-6 in cell culture medium using surface plasmon resonance biosensors," *Cytokine,* vol. 51, pp. 107-111, Jul 2010.
[65] J. Martinez-Perdiguero, A. Retolaza, L. Bujanda, and S. Merino, "Surface plasmon resonance immunoassay for the detection of the TNF alpha biomarker in human serum," *Talanta,* vol. 119, pp. 492-497, Feb 2014.
[66] W. C. Law, K. T. Yong, A. Baev, and P. N. Prasad, "Sensitivity Improved Surface Plasmon Resonance Biosensor for Cancer Biomarker Detection Based on Plasmonic Enhancement," *Acs Nano,* vol. 5, pp. 4858-4864, Jun 2011.
[67] T. M. Battaglia, J. F. Masson, M. R. Sierks, S. P. Beaudoin, J. Rogers, K. N. Foster*, et al.*, "Quantification of cytokines involved in wound healing using surface plasmon resonance," *Analytical Chemistry,* vol. 77, pp. 7016-7023, Nov 2005.
[68] D. Regatos, B. Sepulveda, D. Farina, L. G. Carrascosa, and L. M. Lechuga, "Suitable combination of noble/ferromagnetic metal multilayers for enhanced magneto-plasmonic biosensing," *Optics Express,* vol. 19, pp. 8336-8346, Apr 2011.

[69] T. Huang, P. D. Nallathamby, and X. H. N. Xu, "Photostable Single-Molecule Nanoparticle Optical Biosensors for Real-Time Sensing of Single Cytokine Molecules and Their Binding Reactions," *Journal of the American Chemical Society,* vol. 130, pp. 17095-17105, Dec 17 2008.
[70] C. Y. Chiang, M. L. Hsieh, K. W. Huang, L. K. Chau, C. M. Chang, and S. R. Lyu, "Fiber-optic particle plasmon resonance sensor for detection of interleukin-1 beta in synovial fluids," *Biosensors & Bioelectronics,* vol. 26, pp. 1036-1042, Nov 2010.
[71] Y. C. Huang, C. Y. Chiang, C. H. Li, T. C. Chang, C. S. Chiang, L. K. Chau*, et al.*, "Quantification of tumor necrosis factor-alpha and matrix metalloproteinases-3 in synovial fluid by a fiber-optic particle plasmon resonance sensor," *Analyst,* vol. 138, pp. 4599-4606, 2013.
[72] E. Stern, A. Vacic, N. K. Rajan, J. M. Criscione, J. Park, B. R. Ilic*, et al.*, "Label-free biomarker detection from whole blood," *Nature Nanotechnology,* vol. 5, pp. 138-142, Feb 2010.
[73] G. Stybayeva, M. Kairova, E. Ramanculov, A. L. Simonian, and A. Revzin, "Detecting interferon-gamma release from human CD4 T-cells using surface plasmon resonance," *Colloids and Surfaces B-Biointerfaces,* vol. 80, pp. 251-255, Oct 2010.
[74] Y. Liu, J. Yan, M. C. Howland, T. Kwa, and A. Revzin, "Micropatterned Aptasensors for Continuous Monitoring of Cytokine Release from Human Leukocytes," *Analytical Chemistry,* vol. 83, pp. 8286-8292, Nov 2011.
[75] Y. Liu, Q. Zhou, and A. Revzin, "An aptasensor for electrochemical detection of tumor necrosis factor in human blood," *Analyst,* vol. 138, pp. 4321-4326, 2013.
[76] Y. Liu, T. Kwa, and A. Revzin, "Simultaneous detection of cell-secreted TNF-alpha, and IFN-gamma using micropatterned aptamer-modified electrodes," *Biomaterials,* vol. 33, pp. 7347-7355, Oct 2012.
[77] X. P. A. Gao, G. F. Zheng, and C. M. Lieber, "Subthreshold Regime has the Optimal Sensitivity for Nanowire FET Biosensors," *Nano Letters,* vol. 10, pp. 547-552, Feb 2010.
[78] T. Kwa, Q. Zhou, Y. D. Gao, A. Rahimian, L. Kwon, Y. Liu*, et al.*, "Reconfigurable microfluidics with integrated aptasensors for monitoring intercellular communication," *Lab on a Chip,* vol. 14, pp. 1695-1704, 2014.
[79] K. Shoorideh and C. O. Chui, "On the origin of enhanced sensitivity in nanoscale FET-based biosensors," *Proceedings of the National Academy of Sciences of the United States of America,* vol. 111, pp. 5111-5116, Apr 2014.
[80] J. Alicea, Y. Oreg, G. Refael, F. von Oppen, and M. P. A. Fisher, "Non-Abelian statistics and topological quantum information processing in 1D wire networks," *Nature Physics,* vol. 7, pp. 412-417, May 2011.
[81] W. Al-Sawai, H. Lin, R. S. Markiewicz, L. A. Wray, Y. Xia, S. Y. Xu*, et al.*, "Topological electronic structure in half-Heusler topological insulators," *Physical Review B,* vol. 82, p. 5, Sep 2010.
[82] J. J. Cha and Y. Cui, "TOPOLOGICAL INSULATORS The surface surfaces," *Nature Nanotechnology,* vol. 7, pp. 85-86, Feb 2012.
[83] C. L. Kane and E. J. Mele, "Z(2) topological order and the quantum spin Hall effect," *Physical Review Letters,* vol. 95, p. 4, Sep 2005.

[84] F. Schedin, A. K. Geim, S. V. Morozov, E. W. Hill, P. Blake, M. I. Katsnelson*, et al.*, "Detection of individual gas molecules adsorbed on graphene," *Nature Materials,* vol. 6, pp. 652-655, Sep 2007.
[85] K. Novoselov and A. Geim, "Graphene detects single molecule of toxic gas," *Materials Technology,* vol. 22, pp. 178-179, Sep 2007.
[86] S. Bae, H. Kim, Y. Lee, X. F. Xu, J. S. Park, Y. Zheng*, et al.*, "Roll-to-roll production of 30-inch graphene films for transparent electrodes," *Nature Nanotechnology,* vol. 5, pp. 574-578, Aug 2010.
[87] W. Park, J. Baik, T. Y. Kim, K. Cho, W. K. Hong, H. J. Shin*, et al.*, "Photoelectron Spectroscopic Imaging and Device Applications of Large-Area Patternable Single-Layer MoS2 Synthesized by Chemical Vapor Deposition," *Acs Nano,* vol. 8, pp. 4961-4968, May 2014.
[88] X. Liang, A. S. P. Chang, Y. Zhang, B. D. Harteneck, H. Choo, D. L. Olynick*, et al.*, "Electrostatic Force Assisted Exfoliation of Prepatterned Few-Layer Graphenes into Device Sites," *Nano Letters,* vol. 9, pp. 467-472, Jan 2009.
[89] X. G. Liang, V. Giacometti, A. Ismach, B. D. Harteneck, D. L. Olynick, and S. Cabrini, "Roller-style electrostatic printing of prepatterned few-layer-graphenes," *Applied Physics Letters,* vol. 96, p. 3, Jan 2010.
[90] H. Nam, S. Wi, H. Rokni, M. K. Chen, G. Priessnitz, W. Lu*, et al.*, "MoS2 Transistors Fabricated via Plasma-Assisted Nanoprinting of Few-Layer MoS2 Flakes into Large-Area Arrays," *Acs Nano,* vol. 7, pp. 5870-5881, Jul 2013.
[91] B. B. Aggarwal and K. Natarajan, "Tumor necrosis factors: Developments during the last decade," *European Cytokine Network,* vol. 7, pp. 93-124, Apr-Jun 1996.
[92] D. Aderka, "The potential biological and clinical significance of the soluble tumor necrosis factor receptors," *Cytokine and Growth Factor Reviews,* vol. 7, pp. 231-240, 1996.
[93] W. Shurety, A. Merino-Trigo, D. Brown, D. A. Hume, and J. L. Stow, "Localization and post-Golgi trafficking of tumor necrosis factor-alpha in macrophages," *Journal of Interferon and Cytokine Research,* vol. 20, pp. 427-438, Apr 2000.
[94] R. Gorlin, "THE BIOLOGICAL ACTIONS AND POTENTIAL CLINICAL-SIGNIFICANCE OF DIETARY PSI-3 FATTY-ACIDS," *Archives of Internal Medicine,* vol. 148, pp. 2043-2048, Sep 1988.
[95] W. J. Frazier and M. W. Hall, "Immunoparalysis and adverse outcomes from critical illness," *Pediatric Clinics of North America,* vol. 55, pp. 647-+, Jun 2008.
[96] M. W. Hall, N. L. Knatz, C. Vetterly, S. Tomarello, M. D. Wewers, H. D. Volk*, et al.*, "Immunoparalysis and nosocomial infection in children with multiple organ dysfunction syndrome," *Intensive Care Medicine,* vol. 37, pp. 525-532, Mar 2011.
[97] W. Z. Bao, X. H. Cai, D. Kim, K. Sridhara, and M. S. Fuhrer, "High mobility ambipolar MoS2 field-effect transistors: Substrate and dielectric effects," *Applied Physics Letters,* vol. 102, p. 4, Jan 2013.
[98] M. K. Chen, H. Nam, S. J. Wi, L. Ji, X. Ren, L. F. Bian*, et al.*, "Stable few-layer MoS2 rectifying diodes formed by plasma-assisted doping," *Applied Physics Letters,* vol. 103, p. 4, Sep 2013.

[99] Y. J. Zhang, J. T. Ye, Y. Yornogida, T. Takenobu, and Y. Iwasa, "Formation of a Stable p-n Junction in a Liquid-Gated MoS2 Ambipolar Transistor," *Nano Letters,* vol. 13, pp. 3023-3028, Jul 2013.
[100] F. N. Ishikawa, M. Curreli, H. K. Chang, P. C. Chen, R. Zhang, R. J. Cote*, et al.*, "A Calibration Method for Nanowire Biosensors to Suppress Device-to-Device Variation," *Acs Nano,* vol. 3, pp. 3969-3976, Dec 2009.
[101] V. H. Perez-Luna, M. J. O'Brien, K. A. Opperman, P. D. Hampton, G. P. Lopez, L. A. Klumb*, et al.*, "Molecular recognition between genetically engineered streptavidin and surface-bound biotin," *Journal of the American Chemical Society,* vol. 121, pp. 6469-6478, Jul 1999.
[102] L. S. Jung, K. E. Nelson, P. S. Stayton, and C. T. Campbell, "Binding and dissociation kinetics of wild-type and mutant streptavidins on mixed biotin-containing alkylthiolate monolayers," *Langmuir,* vol. 16, pp. 9421-9432, Nov 2000.
[103] R. N. Germain, "The art of the probable: System control in the adaptive immune system," *Science,* vol. 293, pp. 240-245, Jul 2001.
[104] R. A. Seder, P. A. Darrah, and M. Roederer, "T-cell quality in memory and protection: implications for vaccine design," *Nature Reviews Immunology,* vol. 8, pp. 247-258, Apr 2008.
[105] N. P. Restifo, M. E. Dudley, and S. A. Rosenberg, "Adoptive immunotherapy for cancer: harnessing the T cell response," *Nature Reviews Immunology,* vol. 12, pp. 269-281, Apr 2012.
[106] J. A. Woodfolk, "T-cell responses to allergens," *Journal of Allergy and Clinical Immunology,* vol. 119, pp. 280-294, Feb 2007.
[107] M. Noack and P. Miossec, "Th17 and regulatory T cell balance in autoimmune and inflammatory diseases," *Autoimmunity Reviews,* vol. 13, pp. 668-677, Jun 2014.
[108] F. Issa, A. Schiopu, and K. J. Wood, "Role of T cells in graft rejection and transplantation tolerance," *Expert Review of Clinical Immunology,* vol. 6, pp. 155-169, Jan 2010.
[109] M. Edinger, P. Hoffmann, J. Ermann, K. Drago, C. G. Fathman, S. Strober*, et al.*, "CD4(+)CD25(+) regulatory T cells preserve graft-versus-tumor activity while inhibiting graft-versus-host disease after bone marrow transplantation," *Nature Medicine,* vol. 9, pp. 1144-1150, Sep 2003.
[110] C. Hartono, T. Muthukumar, and M. Suthanthiran, "Immunosuppressive Drug Therapy," *Cold Spring Harbor Perspectives in Medicine,* vol. 3, Sep 2013.
[111] C. Ozdemir, U. C. Kucuksezer, M. Akdis, and C. A. Akdis, "Specific immunotherapy and turning off the T cell: how does it work?," *Annals of Allergy Asthma & Immunology,* vol. 107, pp. 381-392, Nov 2011.
[112] Y. Liu, Z. Matharu, A. Rahimian, and A. Revzin, "Detecting multiple cell-secreted cytokines from the same aptamer-functionalized electrode," *Biosensors & Bioelectronics,* vol. 64, pp. 43-50, Feb 2015.
[113] B. R. Oh, N. T. Huang, W. Q. Chen, J. H. Seo, P. Y. Chen, T. T. Cornell*, et al.*, "Integrated Nanoplasmonic Sensing for Cellular Functional Immunoanalysis Using Human Blood," *Acs Nano,* vol. 8, pp. 2667-2676, Mar 2014.

[114] Y. B. Zheng, B. Kiraly, P. Weiss, and T. Huang, "Molecular plasmonics for biology and nanomedicine," *Nanomedicine,* vol. 7, pp. 751-770, May 2012.
[115] M. S. Wang, C. L. Zhao, X. Y. Miao, Y. H. Zhao, J. Rufo, Y. J. Liu*, et al.*, "Plasmofluidics: Merging Light and Fluids at the Micro-/Nanoscale," *Small,* vol. 11, pp. 4423-4444, Sep 2015.
[116] T. Chatila, L. Silverman, R. Miller, and R. Geha, "MECHANISMS OF T-CELL ACTIVATION BY THE CALCIUM IONOPHORE IONOMYCIN," *Journal of Immunology,* vol. 143, pp. 1283-1289, Aug 1989.
[117] B. J. Nankivell and S. I. Alexander, "Mechanisms of Disease: Rejection of the Kidney Allograft," *New England Journal of Medicine,* vol. 363, pp. 1451-1462, Oct 2010.
[118] R. Vafadari, R. Kraaijeveld, W. Weimar, and C. C. Baan, "Tacrolimus Inhibits NF-kappa B Activation in Peripheral Human T Cells," *Plos One,* vol. 8, p. 9, Apr 2013.
[119] A. Rao, C. Luo, and P. G. Hogan, "Transcription factors of the NFAT family: Regulation and function," *Annual Review of Immunology,* vol. 15, pp. 707-747, 1997.
[120] H. Khalaf, J. Jass, and P. E. Olsson, "Differential cytokine regulation by NF-kappa B and AP-1 in Jurkat T-cells," *Bmc Immunology,* vol. 11, p. 12, May 2010.
[121] M. J. Barten, A. Tarnok, J. Garbade, H. B. Bittner, S. Dhein, F. W. Mohr*, et al.*, "Pharmacodynamics of T-cell function for monitoring immunosuppression," *Cell Proliferation,* vol. 40, pp. 50-63, Feb 2007.
[122] J. D. Pirsch, J. Miller, M. H. Deierhoi, F. Vincenti, and R. S. Filo, "A comparison of tacrolimus (FK506) and cyclosporine for immunosuppression after cadaveric renal transplantation," *Transplantation,* vol. 63, pp. 977-983, Apr 1997.
[123] S. X. Leng, J. E. McElhaney, J. D. Walston, D. X. Xie, N. S. Fedarko, and G. A. Kuchel, "ELISA and multiplex technologies for cytokine measurement in inflammation and aging research," *Journals of Gerontology Series a-Biological Sciences and Medical Sciences,* vol. 63, pp. 879-884, Aug 2008.
[124] Q. Han, N. Bagheri, E. M. Bradshaw, D. A. Hafler, D. A. Lauffenburger, and J. C. Love, "Polyfunctional responses by human T cells result from sequential release of cytokines," *Proceedings of the National Academy of Sciences of the United States of America,* vol. 109, pp. 1607-1612, Jan 2012.
[125] Y. Lu, Q. Xue, M. R. Eisele, E. S. Sulistijo, K. Brower, L. Han*, et al.*, "Highly multiplexed profiling of single-cell effector functions reveals deep functional heterogeneity in response to pathogenic ligands," *Proceedings of the National Academy of Sciences of the United States of America,* vol. 112, pp. E607-E615, Feb 2015.
[126] P. Kobbe, Y. Vodovotz, D. J. Kaczorowski, K. P. Mollen, T. R. Billiar, and H. C. Pape, "Patterns of cytokine release and evolution of remote organ dysfunction after bilateral femur fracture," *Shock,* vol. 30, pp. 43-47, Jul 2008.
[127] A. Sica, L. Dorman, V. Viggiano, M. Cippitelli, P. Ghosh, N. Rice*, et al.*, "Interaction of NF-kappa B and NFAT with the interferon-gamma promoter," *Journal of Biological Chemistry,* vol. 272, pp. 30412-30420, Nov 1997.

[128] A. Kiani, A. Rao, and J. Aramburu, "Manipulating immune responses with immunosuppressive agents that target NFAT," *Immunity,* vol. 12, pp. 359-372, Apr 2000.
[129] V. Baud and M. Karin, "Signal transduction by tumor necrosis factor and its relatives," *Trends in Cell Biology,* vol. 11, pp. 372-377, Sep 2001.
[130] Z. Y. Wang, H. Sato, S. Kusam, S. Sehra, L. M. Toney, and A. L. Dent, "Regulation of IL-10 gene expression in Th2 cells by Jun proteins," *Journal of Immunology,* vol. 174, pp. 2098-2105, Feb 2005.
[131] K. Taga and G. Tosato, "IL-10 INHIBITS HUMAN T-CELL PROLIFERATION AND IL-2 PRODUCTION," *Journal of Immunology,* vol. 148, pp. 1143-1148, Feb 1992.
[132] D. F. Fiorentino, A. Zlotnik, P. Vieira, T. R. Mosmann, M. Howard, K. W. Moore*, et al.*, "IL-10 ACTS ON THE ANTIGEN-PRESENTING CELL TO INHIBIT CYTOKINE PRODUCTION BY TH1 CELLS," *Journal of Immunology,* vol. 146, pp. 3444-3451, May 1991.
[133] G. Delprete, M. Decarli, F. Almerigogna, M. G. Giudizi, R. Biagiotti, and S. Romagnani, "HUMAN IL-10 IS PRODUCED BY BOTH TYPE-1 HELPER (TH1) AND TYPE-2 HELPER (TH2) T-CELL CLONES AND INHIBITS THEIR ANTIGEN-SPECIFIC PROLIFERATION AND CYTOKINE PRODUCTION," *Journal of Immunology,* vol. 150, pp. 353-360, Jan 1993.
[134] H. Groux, M. Bigler, J. E. deVries, and M. G. Roncarolo, "Interleukin-10 induces a long-term antigen-specific anergic state in human CD4(+) T cells," *Journal of Experimental Medicine,* vol. 184, pp. 19-29, Jul 1996.
[135] S. B. A. Cohen, S. L. Parry, M. Feldmann, and B. Foxwell, "Autocrine and paracrine regulation of human T cell IL-10 production," *Journal of Immunology,* vol. 158, pp. 5596-5602, Jun 1997.
[136] K. M. Mayer, S. Lee, H. Liao, B. C. Rostro, A. Fuentes, P. T. Scully*, et al.*, "A label-free immunoassay based upon localized surface plasmon resonance of gold nanorods," *Acs Nano,* vol. 2, pp. 687-692, Apr 2008.
[137] G. Bellapadrona, A. B. Tesler, D. Grunstein, L. H. Hossain, R. Kikkeri, P. H. Seeberger*, et al.*, "Optimization of localized surface plasmon resonance transducers for studying carbohydrate-protein interactions," *Anal Chem,* vol. 84, pp. 232-40, Jan 3 2012.
[138] D. A. Stuart, A. J. Haes, C. R. Yonzon, E. M. Hicks, and R. P. Van Duyne, "Biological applications of localised surface plasmonic phenomenae," *IEE Proc Nanobiotechnol,* vol. 152, pp. 13-32, Feb 2005.
[139] J. Martins e Silva, "Biochemical characterization and metabolic effects of tumor necrosis factor," *Acta medica portuguesa,* vol. 4 Suppl 1, pp. 20S-27S, 1991 1991.
[140] H. P. Benton, "Benton_cytokines and their receptors(1991)," *Current Opinion in Cell Biology,* vol. 3, pp. 171-175, 1991.
[141] J. S. Boomer, K. To, K. C. Chang, O. Takasu, D. F. Osborne, A. H. Walton*, et al.*, "Immunosuppression in Patients Who Die of Sepsis and Multiple Organ Failure," *Jama-Journal of the American Medical Association,* vol. 306, pp. 2594-2605, Dec 21 2011.

[142] W. Chen, N. T. Huang, X. Li, Z. T. Yu, K. Kurabayashi, and J. Fu, "Emerging microfluidic tools for functional cellular immunophenotyping: a new potential paradigm for immune status characterization," *Front Oncol,* vol. 3, p. 98, 2013.
[143] T. K. Q. Zhou, Y. Liu, A. Revzin, "Cytokine biosensors: the future of infectious disease diagnosis?," *Expert Rev. Anti Infec. Ther.,* vol. 10, pp. 1079-1081, 2012.
[144] Y. Shen, J. Zhou, T. Liu, Y. Tao, R. Jiang, M. Liu*, et al.*, "Plasmonic gold mushroom arrays with refractive index sensing figures of merit approaching the theoretical limit," *Nat Commun,* vol. 4, p. 2381, Aug 27 2013.
[145] T. Endo, S. Yamamura, N. Nagatani, Y. Morita, Y. Takamura, and E. Tamiya, "Localized surface plasmon resonance based optical biosensor using surface modified nanoparticle layer for label-free monitoring of antigen–antibody reaction," *Science and Technology of Advanced Materials,* vol. 6, pp. 491-500, 2005.
[146] T. Endo, S. Yamamura, K. Kerman, and E. Tamiya, "Label-free cell-based assay using localized surface plasmon resonance biosensor," *Anal Chim Acta,* vol. 614, pp. 182-9, May 5 2008.
[147] W. P. Hall, S. N. Ngatia, and R. P. Van Duyne, "LSPR Biosensor Signal Enhancement Using Nanoparticle-Antibody Conjugates," *J Phys Chem C Nanomater Interfaces,* vol. 115, pp. 1410-1414, Feb 10 2011.
[148] H. M. Hiep, T. Nakayama, M. Saito, S. Yamamura, Y. Takamura, and E. Tamiya, "A Microfluidic Chip Based on Localized Surface Plasmon Resonance for Real-Time Monitoring of Antigen–Antibody Reactions," *Japanese Journal of Applied Physics,* vol. 47, pp. 1337-1341, 2008.
[149] K. M. Mayer and J. H. Hafner, "Localized surface plasmon resonance sensors," *Chem Rev,* vol. 111, pp. 3828-57, Jun 8 2011.
[150] J. Mitchell, "Small molecule immunosensing using surface plasmon resonance," *Sensors (Basel),* vol. 10, pp. 7323-46, 2010.
[151] L. H. Guo and D. H. Kim, "LSPR biomolecular assay with high sensitivity induced by aptamer-antigen-antibody sandwich complex," *Biosensors & Bioelectronics,* vol. 31, pp. 567-570, Jan 2012.
[152] A. Salehi-Reyhani, S. Sharma, E. Burgin, M. Barclay, A. Cass, M. A. Neil*, et al.*, "Scaling advantages and constraints in miniaturized capture assays for single cell protein analysis," *Lab Chip,* vol. 13, pp. 2066-74, Jun 7 2013.
[153] W. Chen, N. T. Huang, B. Oh, R. H. Lam, R. Fan, T. T. Cornell*, et al.*, "Surface-micromachined microfiltration membranes for efficient isolation and functional immunophenotyping of subpopulations of immune cells," *Adv Healthc Mater,* vol. 2, pp. 965-75, Jul 2013.
[154] G. T. Hermanson, "Bioconjugate Techniques," *Academic Press (Book Chapter),* vol. 1st edition, 1996 1996.
[155] R. P. Van Duyne and K. A. Willets, "ANYL 41-Localized surface plasmon R\resonance spectroscopy and sensing," *Abstracts of Papers of the American Chemical Society,* vol. 234, p. 1, Aug 2007.
[156] T. Lawrence, "The Nuclear Factor NF-kappa B Pathway in Inflammation," *Cold Spring Harbor Perspectives in Biology,* vol. 1, p. 10, Dec 2009.

[157] J. Lazar, O. Cip, M. Cizek, J. Hrabina, and Z. Buchta, "Suppression of air refractive index variations in high-resolution interferometry," *Sensors (Basel),* vol. 11, pp. 7644-55, 2011.
[158] N. T. Huang, W. Chen, B. R. Oh, T. T. Cornell, T. P. Shanley, J. Fu*, et al.*, "An integrated microfluidic platform for in situ cellular cytokine secretion immunophenotyping," *Lab Chip,* vol. 12, pp. 4093-101, Oct 21 2012.
[159] T. T. Cornell, L. Sun, M. W. Hall, J. G. Gurney, M. J. Ashbrook, R. G. Ohye*, et al.*, "Clinical implications and molecular mechanisms of immunoparalysis after cardiopulmonary bypass," *J Thorac Cardiovasc Surg,* vol. 143, pp. 1160-1166 e1, May 2012.
[160] M. Nimah, B. Zhao, A. G. Denenberg, O. Bueno, J. Molkentin, H. R. Wong*, et al.*, "CONTRIBUTION OF MKP-1 REGULATION OF p38 TO ENDOTOXIN TOLERANCE," *Shock,* vol. 23, pp. 80-87, 2005.
[161] C. Ma, R. Fan, H. Ahmad, Q. H. Shi, B. Comin-Anduix, T. Chodon*, et al.*, "A clinical microchip for evaluation of single immune cells reveals high functional heterogeneity in phenotypically similar T cells," *Nature Medicine,* vol. 17, pp. 738-U133, Jun 2011.
[162] W. de Jager, H. te Velthuis, B. J. Prakken, W. Kuis, and G. T. Rijkers, "Simultaneous detection of 15 human cytokines in a single sample of stimulated peripheral blood mononuclear cells," *Clinical and Diagnostic Laboratory Immunology,* vol. 10, pp. 133-139, Jan 2003.
[163] C. C. Caldwell and R. S. Hotchkiss, "The first step in utilizing immune-modulating therapies: immune status determination," *Critical Care,* vol. 15, p. 2, 2011.
[164] L. F. Gentile, A. G. Cuenca, P. A. Efron, D. Ang, A. Bihorac, B. A. McKinley*, et al.*, "Persistent inflammation and immunosuppression: A common syndrome and new horizon for surgical intensive care," *Journal of Trauma and Acute Care Surgery,* vol. 72, pp. 1491-1501, Jun 2012.
[165] J. R. Korzenik and D. K. Podolsky, "Evolving knowledge and therapy of inflammatory bowel disease," *Nature Reviews Drug Discovery,* vol. 5, pp. 197-209, Mar 2006.